The Physics of Wind Instruments

by

Jared Thacker

A dissertation submitted to the Graduate Faculty of
Auburn University
in partial fulfillment of the
requirements for the Degree of
Doctor of Philosophy

Auburn, Alabama
May 7, 2022

Keywords: Physics, Acoustics, Wind Instruments

Approved by

Nicholas Giordano, Chair, Professor of Physics
Guillaume Marc Laurent, Associate Professor of Physics
Yu Lin, Alumni Professor of Physics
Stuart Loch, Professor of Physics

Abstract

Musical instruments have been studied by physicists for centuries due to their complex mechanisms and the presence of many pieces of fundamental physics within. This dissertation aims its focus on wind instruments which are particularly difficult to model because the equations that govern air flow are nonlinear. The last couple of decades have seen the rise of fast and cheap computing power which make it possible for researchers to use first principles approaches employing the Naiver-Stokes equations. The goals of this project were to improve the design of the recorder using simulations that are based on first principles physics, to understand the effect of a musician's blowing profile on the tone of the recorder, and to present and discuss a model for a clarinet reed that will be part of fully distributed model of the clarinet. This thesis explores how simulations based on the Navier-Stokes equations can be used to get new insights into wind instruments. Specifically, these simulations which are all based on the Navier-Stokes equations are used to (1) understand how small alterations to the geometry of the recorder will affect the dynamical playing range for fundamental modes of a recorder. The new design was identified using simulation results then validated via experiments on 3D printed recorders. (2) A full sized soprano recorder that mimics the geometry of the Yamaha YRS-23 was used to study the effect of blowing profile on the tone of the instrument. The presence of inharmonic frequencies in the attack transient of the tone were detected which affect the tone color of the instrument. (3) A model of the reed of the clarinet is presented; this particular model of the reed allows more efficient computations in Navier-Stokes simulations of the clarinet. Instrument makers typically improve instrument design by using guided intuition. The work in this dissertation provides insights on how wind instrument design can be improved by using a more quantitative, scientific, and collaborative approach between instrument makers and scientists.

Acknowledgments

I would like to thank Jeff Estep for his patient help with 3D printing. I would also like to thank Dr. Chris Easley for all of his help with the microscopy.

I would also like to thank my wife, Jenny, whose love and patience during my graduate education helped propel me to graduation. And last, but certainly not least, I would like to thank to my parents Ken and Kim; you guys have always had my back.

Table of Contents

Abstract ii

Acknowledgments iii

List of Figures vii

List of Tables xv

1 Introduction 1

2 Numerical Methods for Partial Differential Equations 6

2.1 The Navier-Stokes Equations 10

2.2 Numerical Methods 11

2.3 Implementation 12

3 The Physics of the Recorder 13

3.1 Introduction to the Fundamentals of the Recorder 13

3.2 Regime Change in Recorders 18

3.3 Sopranino, Bass Recorder Analogues, and threshold Speed Shifts . . . 19

3.4 Threshold Speed Shift and the Link to Vorticity 21

3.5 Mitigating the Threshold Shift in the Bass Style Recorder 25

4 From Simulations to Reality: Constructing Physical Recorders 31

4.1 Recorder Design 31

4.1.1 Sopranino Style Recorder Dimensions 31
4.1.2 Bass Style and Modified Bass Style Recorders 34
4.2 Designing Recorders with AutoCAD 34
4.2.1 AutoCAD Commands 37
4.2.2 Designing Recorders: Step 1 38
4.2.3 Designing the Recorders: Step 2 41
4.2.4 Fabricating the Recorders: Step 3 42
4.2.5 Designing Recorders: Step 4 44
4.3 Overview of 3D Printing 44
4.3.1 3D Printers 46
4.4 3D Printing Side Effects, Microscopy and Uncertainty 47

5 Experimental Setup, Results and Comparison 51
5.1 Introduction 51
5.2 Experimental Setup 52
5.3 Results and Theoretical Comparison 55

6 Effects of Blowing Profile on the Tone of a Soprano Recorder 65
6.1 Autocorrelation and Correlograms 66
6.1.1 Spectral Analysis Using FFT 67
6.1.2 Autocorrelation and the Correlogram 72
6.1.3 Alternative Correlograms 75
6.1.4 Artifact Frequencies 75
6.2 Recorder Geometry Under Analysis 79
6.3 Results 81
6.3.1 Spectral Analysis: C5 81

6.3.2 Spectral Analysis: E5 96
6.3.3 Spectral Analysis: G5 105
6.3.4 Spectral Analysis: C6 114
6.4 Summary of Results 123

7 Modeling a Clarinet Reed 126
7.1 Implicit Theta Method 129
7.2 Simulations 131
7.3 Conclusion 133

8 Summary and Conclusion 136

References 139

List of Figures

2.1 A diagram of a numerical stencil showing the relationship between adjacent lattice points and successive time-steps. 9

3.1 Examples of renaissance recorders [1]. 14

3.2 Examples of baroque recorders [1]. 14

3.3 A schematic of a cross-section of a recorder looking from the side of the instrument. 15

3.4 A schematic cross-section of a recorder looking from the open end of the instrument (the right) in figure (3.3). 16

3.5 Left: Results from one of my simulations illustrating the vortex and the air jet near the labium. Right: A diagram showing the location and geometry of the left side of this figure. 16

3.6 The vortex mechanism near the labium that is necessary for a recorder to facilitate self-sustained oscillations for sound production ($u_0 = 28$ m/s). 17

3.7 Pressure Vs Time graph for a point outside of the recorder that illustrates what a listener might hear from these simulated instruments ($u_0 = 28$ m/s). 17

3.8 ρ vs t graph from a simulation illustrating the pressure/density oscillations in the resonator of the recorder at a blowing speed of $u_0 = 28$ m/s and a fundamental frequency of $f = 1183$ Hz. 18

3.9 A schematic of the general form of the cross-section of a simplified recorder design. 20

3.10 A schematic of the cross-section of the unmodified bass-style recorder. 20

3.11 Threshold curves for the *sopranino*- and *bass*-style recorders 21

3.12 Fourier spectrum for the sopranino style recorder (10 mm $\times$10 mm) $u_0 = 28$ m/s. The label P1 indicates the power of the first harmonic. . . 22

3.13 Fourier spectrum for the bass style recorder (10 mm $\times$ 5 mm) $u_0 = 28$ m/s. The labels P1 and P2 indicate the power of the first and second harmonic respectively. 22

3.14 The vortex mechanism for a sopranino style recorder (10 mm $\times$10 mm) at ($u_0 = 28$ m/s) for one period of motion. 22

3.15 The vortex mechanism for a bass style recorder (10 mm $\times$ 5 mm) at ($u_0 = 28$ m/s) for one period of motion. 22

3.16 Simulation for a sopranino style recorder at $u_0 = 28$ m/s. Note the position of the air-jet above the labium. 23

3.17 Simulation for a bass style recorder at $u_0 = 28$ m/s. Note the position of the air-jet at the height of the labium. 24

3.18 A schematic of the cross-section of the modified bass-style recorder. Please note the trench in the bottom left-hand corner of the resonator. . . 25

3.19 Vortex pattern for a modified bass style recorder for one period of motion at a blowing speed of $u_0 = 28$ m/s. 27

3.20 Vortex pattern sequence for a bass style recorder for one period of motion at a blowing speed of $u_0 = 28$ m/s. 28

3.21 Fourier spectrum for the unmodified bass-style recorder at $u = 28$ m/s. 29

3.22 Fourier spectrum for the modified bass style recorder at $u = 28$ m/s. . . 29

3.23 Fourier spectrum for the unmodified bass-style recorder at $u_0 = 35$ m/s. 30

3.24 Fourier spectrum for the modified bass style recorder at $u_0 = 35$ m/s. . 30

3.25 Threshold speed curve for the unmodified bass-style recorder. 30

3.26 Threshold speed curve for the modified bass-style recorder. 30

4.1 A schematic of the general form of the cross-section of a simplified recorder design. 32

4.2 Schematic of the cross-section of the sopranino style recorder. Note the dimensions are given. 32

4.3 Schematic of the cross-section of the sopranino style recorder looking down the resonator of the recorder as viewed from the open end (the end at right in fig. (4.3). Note the dimensions given. 33

4.4 Schematic of the cross-section of the (unmodified) bass style recorder. Note the dimensions are given. 34

4.5 A schematic of the cross-section of the (unmodified) bass style recorder looking down the resonator of the recorder as viewed from the open end (the end at right in fig. (4.4)). Note the dimensions are given. 35

4.6 A schematic of the cross-section of the modified bass style recorder. Note the dimensions are given. 35

4.7 A schematic of the cross-section of the modified bass style recorder looking down the resonator of the recorder as viewed from the open end (the end at right in fig. 4.6) Please note the dimensions are given. . . 36

4.8 A visual of what AutoCAD (2015) looks like before anything is drawn. . 38

4.9 A visual of what the finished cross-section looks like in AutoCAD after step 1 is performed. Note that the recorder is flipped to the right. 39

4.10 A visual of what the finished cross-section looks like in AutoCAD after step 1 is performed. In this figure, the area around the labium and channel has been magnified in order to display the most important components of the recorder. 40

4.11 A visual of what the extruded cross-sections look like in AutoCAD after step 2 is performed. 41

4.12 A visual of what the extruded cross-sections look like in AutoCAD after step 2 is performed. 42

4.13 A visual of what the addition of the supports looks like in AutoCAD after step 3 is performed. 43

4.14 A zoomed in visual of what the addition of the supports looks like in AutoCAD after step 3 is performed. 43

4.15 A visual of what the finished modeled recorder looks like in AutoCAD after step 4 is performed. 44

4.16 A zoomed in visual of what the finished modeled recorder looks like in AutoCAD after step 4 is performed. Take special note that, in this figure, the recorder has been flipped on its side so the labium, channel, supports and tuning fork can be viewed. 45

4.17 A picture of the Tiger printer XHD made by *Romanoff* with its door open revealing the build plate and resin reservoir. 47

4.18 A picture of the MakerBot Replicator+ that was used in this research project. 48

4.19 Example of an image taken with a microscope that was used to measure the channel height along y and for the uncertainty analysis in chapter (4.3.1). Note the rounding at the corners on the left side of the channel. . 50

5.1 A schematic of the experimental setup. The sensor is a piezoresistive pressure transducer and Endevco model: 8510b -1, the computer is a 2017 Apple macbook pro with built in microphone, the bridge amplifier is an Endevco model 126 and the voltmeter used was a Keithley 2100 Multimeter. 53

5.2 Laminar Flow for a rectangular cross-section. 54

5.3 The simulated threshold curve for the sopranino style recorder. The arrow represents the location of the threshold blowing speed. 56

5.4 The theoretical threshold curve for the unmodified bass style recorder. The arrow represents the location of the threshold blowing speed. 57

5.5 The theoretical threshold curve for the modified bass style recorder. The arrow represents the location of the threshold blowing speed. 57

5.6 Both of the experimental threshold curves from the sopranino style recorders that are to be compared against the simulated l threshold plots. The error bar is centered at $u_0 = 43$m/s and has a margin of error of $\pm$ 10%. . . . 59

5.7 Both of the experimental threshold curves from the unmodified bass style recorders that are to be compared against the simulated threshold plots. The error bar is centered at $u_0 = 27$m/s and has a margin of error of $\pm 10\%$. 60

5.8 Both of the experimental threshold curves from the modified bass style recorders that are to be compared against the simulated threshold plots. The error bar is centered at $u_0 = 41$m/s and has a margin of error $\pm 10\%$. 61

5.9 The simulated threshold curves for the sopranino-, bass-, and modified bass-style recorders. 63

5.10 The experimental and theoretical threshold curves for the sopranino style recorder. The simulated threshold curve is given by the black line and symbols. 63

5.11 The experimental and theoretical curves for the bass style recorder. The simulated threshold curve is given by the black line and symbols. 64

5.12 The experimental and theoretical curves for the modified bass style recorder. The simulated threshold curve is given by the black line and symbols. . 64

6.1 Fourier spectrum using 1,024 points for the unmodified bass-style recorder at the regime-change threshold, v_{RC} = 28 m/s. This spectrum was calculated using data from the steady-state (red) region in figure 6.2. 68

6.2 Sound pressure vs. time for an unmodified bass-style recorder at the regime-change threshold, v_{RC} = 28 m/s. The blue line indicates the attack portion of the tone and the red line indicates the steady-state portion of the tone. 69

6.3 Fourier spectrum using 256 points for the unmodified bass-style recorder at the regime-change threshold, v_{RC} = 28 m/s. This spectrum was calculated using data from the steady-state (red) region in figure 6.2. 70

6.4 Fourier spectrum using 1,024 points for the unmodified bass-style recorder at the regime-change threshold, v_{RC} = 28 m/s. This spectrum was calculated using data from the attack (black) region in figure 6.2. 71

6.5 Two correlation windows with n and m, x_m, and w labeled. [2]. 73

6.6 **Top**: A *time delay-real time* correlogram. The value of time, or index m, is located along the x-axis and the time lag, or n is on the y-axis. The value of the Pearson correlation is the darkness of the grayscale color. **Bottom**: A *frequency-real time* correlogram with m plotted along the x-axis and $f = \frac{1}{\Delta t}$ along the y-axis. [2]. 76

6.7 Tones 78

6.8 The Yamaha YRS-23 that we are modeling using NSE. This instrument is 33 cm long and has a tapering cylindrical bore. The instrument in this figure has toneholes that are in the same position along the resonator as the simulated instrument in figure 6.9. 79

6.9 The geometry that we are using in the NSE simulations to model the Yamaha YRS-23. This instrument is 33 cm long and has a cylindrical bore that is 13 mm in diameter. This instrument has toneholes that are in the same position along the resonator as the Yamaha recorder in figure 6.8. In this case the open tone holes correspond to a fingering that produces C6. 80

6.10 Simulated geometry of a soprano recorder illustrating the fingering for C5. 82

6.11 Tones 84

6.12 Correlogram for C5 with a blowing speed of 15 m/s, ramp up time of 5 ms. The window size is 20 ms and the starting time is at 5 ms. 85

6.13 Sound spectra for C5 with a blowing speed of 15 m/s, ramp up time of 5 ms. Each spectrum was calculated with an FFT using 23 ms from figure 6.11a and 6.11b. Each FFT was calculated using 23.5 ms of data with the following midpoints for different the different colored spectra black: 12 ms, red: 20ms, blue: 77 ms, green: 110 ms. 86

6.14 Tones 88

6.15 Correlogram for C5 with a blowing speed of 15 m/s, ramp up time of 30 ms. The window size is 20 ms and the starting time is at 5 ms. 89

6.16 Sound spectrum for C5 with a blowing speed of 15 m/s, ramp up time of 30 ms. Each spectrum was calculated with an FFT using 23 ms from figure 6.14a and 6.14b. Each FFT was calculated using 23.5 ms of data with the following midpoints for different the different colored spectra black: 12 ms, red: 20ms, blue: 77 ms, green: 110 ms. 90

6.17 Tones 91

6.18 Correlogram for C5 with a blowing speed of 12.5 m/s, ramp up time of 5 ms. The window size is 4 ms and the starting time is at 2 ms. 92

6.19 Sound spectrum for C5 with a blowing speed of 12.5 m/s, ramp up time of 5 ms. Each spectrum was calculated with an FFT using 23 ms from figure 6.17a and 6.17b. Each FFT was calculated using 23.5 ms of data with the following midpoints for different the different colored spectra black: 12 ms, red: 20ms, blue: 77 ms, green: 110 ms. 93

6.20 Tones 94

6.21 Correlogram for C5 with a blowing speed of 12.5 m/s, ramp up time of 30 ms. The window size is 4 ms and the starting time is at 2 ms. 95

6.22 Sound spectrum for C5 with a blowing speed of 12.5 m/s, ramp up time of 30 ms. Each spectrum was calculated with an FFT using 23 ms from figure 6.20a and 6.20b. Each FFT was calculated using 23.5 ms of data with the following midpoints for different the different colored spectra black: 12 ms, red: 20ms, blue: 77 ms, green: 110 ms. 96

6.23 Simulated geometry of a soprano recorder illustrating the fingering for E5. 97

6.24 Tones 99

6.25 Correlogram for E5 with a blowing speed of 15 m/s, ramp up time of 5 ms. The window size is 4 ms and the starting time is at 2 ms. 100

6.26 Sound spectrum for E5 with a blowing speed of 15 m/s, ramp up time of 5 ms. Each spectrum was calculated with an FFT using 23 ms from figure 6.24a and 6.24b. Each FFT was calculated using 23.5 ms of data with the following midpoints for different the different colored spectra black: 12 ms, red: 20ms, blue: 77 ms, green: 110 ms. 101

6.27 Tones 103

6.28 Correlogram for E5 with a blowing speed of 15 m/s, ramp up time of 30 ms. The window size is 4 ms and the starting time is at 2 ms. 104

6.29 Sound spectrum for E5 with a blowing speed of 15 m/s, ramp up time of 30 ms. Each spectrum was calculated with an FFT using 23 ms from figure 6.27a and 6.27b. Each FFT was calculated using 23.5 ms of data with the following midpoints for different the different colored spectra black: 12 ms, red: 20ms, blue: 77 ms, green: 110 ms. 105

6.30 Simulated geometry of a soprano recorder illustrating the fingering for G5. 106

6.31 Tones 108

6.32 Correlogram for G5 with a blowing speed of 17 m/s, ramp up time of 5 ms. The window size is 4 ms and the starting time is at 2 ms. 109

6.33 Sound spectrum for G5 with a blowing speed of 17 m/s, ramp up time of 5 ms. Each spectrum was calculated with an FFT using 23 ms from figure 6.31a and 6.31b. Each FFT was calculated using 23.5 ms of data with the following midpoints for different the different colored spectra black: 12 ms, red: 20ms, blue: 77 ms, green: 110 ms. 110

6.34 Tones 112

6.35 Correlogram for G5 with a blowing speed of 17 m/s, ramp up time of 30 ms. The window size is 4 ms and the starting time is at 2 ms. 113

6.36 Sound spectrum for G5 with a blowing speed of 17 m/s, ramp up time of 30 ms. Each spectrum was calculated with an FFT using 23 ms from figure 6.34a and 6.34b. Each FFT was calculated using 23.5 ms of data with the following midpoints for different the different colored spectra black: 12 ms, red: 20ms, blue: 77 ms, green: 110 ms. 114

6.37 Simulated geometry of a soprano recorder illustrating the fingering for C6. 115

6.38 Tones 117

6.39 Correlogram for C6 with a blowing speed of 21 m/s, ramp up time of 5 ms. The window size is 4 ms and the starting time is at 2 ms. 118

6.40 Sound spectrum for C6 with a blowing speed of 21 m/s, ramp up time of 5 ms. Each spectrum was calculated with an FFT using 23 ms from figure 6.38a and 6.38b. Each FFT was calculated using 23.5 ms of data with the following midpoints for different the different colored spectra black: 12 ms, red: 20ms, blue: 77 ms, green: 110 ms. 119

6.41 Tones 121

6.42 Correlogram for C6 with a blowing speed of 21 m/s, ramp up time of 30 ms. The window size is 4 ms and the starting time is at 2 ms. 122

6.43 Sound spectrum for C6 with a blowing speed of 21 m/s, ramp up time of 30 ms. Each spectrum was calculated with an FFT using 23 ms from figure 6.41a and 6.41b. Each FFT was calculated using 23.5 ms of data with the following midpoints for different the different colored spectra black: 12 ms, red: 20ms, blue: 77 ms, green: 110 ms. 123

7.1 Diagram of a nonuniform beam/reed. Diagram is from AW [3]. 128

7.2 Displacement vs time plot for Avanzini parameter set 132

7.3 Fourier transform for Avanzini parameter set. The frequency corresponding the largest power is 1405 Hz. 133

7.4 Displacement vs time plot for the Avanzini parameter set with an additional external force added to the system 134

7.5 Fourier transform for Avanzini parameter set with an external force added to the reed-system. The frequency corresponding the peak is 223 Hz. 135

List of Tables

4.1 A list of the commands used in AutoCAD to make the recorders for 3D printing 37

6.1 A list of the fundamental frequencies of each note, the blowing speeds, and ramp up times that will be used in the analysis in this chapter. . . . 81

7.1 The Avanzini parameter set 131

Chapter 1

Introduction

A very wide variety of musical instruments have existed long before recorded history. As scientists, physicists have sought to understand or describe phenomena present in the universe; the purpose of this project is not to study musical instruments for music performance, but to understand their behavior by applying the principles of physics, and perhaps make improvements to their design. Scientific interest, including research, of musical instruments can be found all throughout history and there are many examples of prominent scientists who have studied them. Early examples of such work are Pythagorean tuning [4] and research on vibrating strings in violins by Galileo Galilei and Marin Mersenne [5].

An example of an instrument that has had extensive research performed on it is the violin. The physical mechanism behind the sound produced by the violin, stick-slip motion, was first observed by Jean-Marie Duhamel [5]. Herman von Helmholtz, who is known to have contributed to multiple scientific fields including electromagnetism, mechanics and physiology, confirmed stick-slip motion by using a vibration microscope to view a violin string and discovered the sawtooth waveform of the vibrating string which is now called Helmholtz motion [5]. Nobel laureate C.V Raman well-known for his work in spectroscopy, used a mechanical bowing machine in a set of experiments, that showed the minimum bowing force needed to maintain stable motion of the violin string is proportional to the speed of the bow and inversely proportional as to the square of the distance from the bridge [5, 6]. Frederick Saunders, another scientist known for his work in spectroscopy was a pioneer in violin research in the first half of the 20^{th} century who compared the acoustics between many classical and modern era violins [7]. Saunders, together with Carleen Hutchins, John Schelleng, and Robert Fryxell

founded the Catgut Acoustical Society (CAS) [5]. One of the accomplishments of the CAS is a truly scientific understanding of the development of the Violin Octet family in use today. So the study of musical instruments is a scientific endeavor that can be experimental, theoretical, or both and beneficial in the following ways: (1) from using the principles of physics we can gain insight into how they work and (2) it is possible to make design improvements to musical instruments.

In the present, acoustics research is still very much active. One of the more popular topics in acoustics research has been the modeling of musical instruments with progressively more fundamental physics. Many different instruments that appear in the scientific literature are the piano [8], the Japanese Koto [9], guitar [10], picolo [11], trumpet [12], and drums [13]. The work in this thesis will focus on wind instruments such as the recorder and clarinet.

In general, the level of difficulty of modeling depends on the family to which the instrument belongs to. String instruments are considered the easiest to model, while wind instruments are some of the most difficult instruments to model and percussion instruments are somewhere in the middle. Early work on the simulation of musical instruments was done on stringed instruments since, the principal mechanism of sound production is the vibration of a string(s) and, the physical laws governing string vibrations are intrinsically less complex than fluid dynamics. The early work that was performed on *wind* instruments such as the recorder [14], flute [15–17], and organ-pipes [14] were for simplified geometries and very short time-scales (millisecond). As computing has seen dramatic advances in power and cost, researchers in the field have included more and more fundamental physics. Therefore, over time, the modeling performed on wind instruments has included more calculations derived from first principles. Many of the earlier models for musical instruments were based on *lumped* models where continuous or *distributed* physics geometries are simplified into discrete masses. For example, one of the earlier attempts to produce a functioning model of the clarinet was performed in 1978 by R. T. Schumacher [18]. In his approximation, he studied a *lumped* model where the input current (induced by the player) is coupled to the acoustic field in the bore of the instrument via a lumped approximation of the clarinet reed. In other words, only the tip of the reed is considered and its equation of motion is an *ordinary* differential equation in time. The integral equation

resulting from the lumped model proposed by Schumacher was solved using various numerical methods [18, 19]. Schumacher's model successfully displays self-sustained oscillations, yields the pressure waveform found in the mouthpiece, and other results that are in reasonable agreement with experiments performed on real clarinets. *Lumped* models can certainly provide good insight. However, if one wishes to study behavior that is related to detailed, quantitative refinements in instrument geometry then one must use a *distrubted* model. For example, if one wishes to study how linear density of a nonuniform clarinet reed alters the behavior of the clarinet, then lumped models are not adequate. For purposes of this thesis, lumped approximations are not sufficient because they cannot be used to study the detailed behavior of the fluid in the wind instrument. For example, in this thesis we study the behavior of a vortex of air that is present inside the recorder; this *is not possible* with a *lumped* approximation.

Fast forwarding nearly 20 years from Schumacher's work to 1995, computational power had increased significantly and numerical simulations on continuous systems were feasible. In 1995 Skordos [14] was the first to simulate the acoustics of flue pipes using the Navier-Stokes equations (NSE) and the lattice Boltzmann method (LBM). The work was cutting edge but had serious limitations of computing power at the time, and as a result, only a two-dimensional recorder was modeled and then only the spaces inside the recorder and just above the labium were considered.

Substantial advancements in computational power have been made since the 1990s and, especially within the last three decades, computational studies of musical instruments have become a significantly more popular approach with the rise of cheap and powerful computational resources [15–17, 20–23]. One example being Giordano [22, 23] who has done several studies on multiple wind instruments using the Navier-Stokes equations which require more powerful computational resources than needed with the lumped approximations of Schumacher or the two-dimensional calculations performed by Skordos. In a 2013 paper, Giordano [23] explored the results of a functional two-dimensional recorder model via direct numerical simulation based on the Navier-Stokes equations. He successfully showed that numerical simulations can be used to predict the qualitative of behavior of real instruments. In [23], Giordano's simulations successfully yield the density variations and fluid velocity which can be used to obtain

visuals/plots of the standing density wave, vortex, air-jet, vortex-shedding, sound spectra, and other qualitative/quantitative behavior. In addition, in a 2014 paper Giordano [22] further explored the results of the three-dimensional model of a recorder. In this paper, Giordano explored the qualitative behavior of jet dynamics, analyzed differences in sound spectra while varying blowing speed, and the effects of chamfers on the raw signal from the recorder [22]. Many of the questions and findings from [23, 22] can only be studied using distributed models based on fundamental physics. For example, the effects of small changes in the geometry of the recorder such as chamfers, cannot be studied under the assumptions of a lumped model. Analyzing the results from small changes in the recorder geometry will be of paramount importance to studies in this project and will be expanded upon in future chapters of this project. Distributed models also allow researchers to study the dynamics of the gas (air, nitrogen) in wind instruments and how small alterations to the geometry can affect those dynamics. For example, one might wish to study the magnitude of the flow velocity at some point in space near or in the instrument; or maybe one is interested in studying *vibrato* by imposing oscillating blowing speeds in the channel of the wind instrument. All of these and more are problems that can only be studied with distributed models, such as the NSE, and that is the approach that will be used in the thesis.

It is now appropriate to give a brief outline of the contents of this thesis. In chapter 2 the numerical methods, algorithms, and equations that are used will be presented and discussed. Section 2.1 will discuss the NSE, section 2.2 will discuss time-domain finite difference methods that we employ to solve the NSE and section 2.3 will discuss specifics on how we implement finite difference methods. In chapter 3, the methods to make a better recorder will be presented in detail and will also set up the background necessary to motivate chapter 4. Section 3.1 will introduce the fundamentals of the recorder, section 3.2 will discuss *regime change* behavior that is present in the recorder family while sections 3.3 - 3.5 are dedicated to calculating, explaining and altering the regime change behavior in the recorder. The changes that were made to the recorder geometry in order to alter the regime change behavior will be validated with experimentation; chapters 4 - 5 will detail the experiment and draw comparisons between both the experiment and simulations. Chapter 4 introduces how the instruments that were used for

experimental purposes were fabricated. Specifically 4.1 discusses how each of style of recorder (bass/sopranino) were designed and the dimensions that were used. Sections 4.2 - 4.3 discuss drawing the recorders with *AutoCAD* and 3D printing. Section 4.4 discusses the limitations of 3D printing and their side effects on the experiment. Chapter 5 will discuss the details of the experiment that was performed in order to validate the simulations of chapter 3; this includes the details of the experimental setup and comparison between the results of the simulations and exeriments. Chapter 6 describes a study of how a player can influence the tone of the recorder. Specifically, chapter 6 explores the effects that varying certain blowing parameters have on the early portion, known as the attack portion, of the tone. The parameters that are studied are ones that players would have control over while playing a real instrument thus providing scientific insight into how musicians produce musical tones. Chapter 7 details the reed modeling that is part of a larger clarinet simulation.

Chapter 2

Numerical Methods for Partial Differential Equations

This project makes extensive use of finite-difference time-domain methods (FDTDM) to numerically calculate various time-dependent quantities using the Navier-Stokes equations and the equation of motion of a clarinet reed. Two such applications of the FDTDM in this project are studies of regime change in recorders and of the vibrations of a reed modeled as a non-uniform bar. The method of finite differences works by approximating the solution to a PDE in space and time over which the independent variables are defined by a discrete grid [24]. The derivatives in the equation are then approximated using difference equations derived from Taylor's theorem. Suppose $y(x)$ is a continuous function and has n continuous derivatives over some interval (a, b). Then for $a < x_0 < b$ and $a < x_0 + \Delta x < b$,

$$y(x_0 + \Delta x) = y(x_0) + \Delta x y'(x_0) + \Delta x^2 \frac{y''(x_0)}{2} + .. + \Delta x^{n-1} \frac{y^{n-1}(x_0)}{n!} + O(\Delta x^n) \quad (2.1)$$

where $O(\Delta x^n)$ is an error term of order n. When solving a PDE numerically, suppose that we know the value of the function y at the point $x = x_0$. For the specific case of the first derivative, we can use equation (2.1) to obtain:

$$\frac{y(x_0 + \Delta x)}{\Delta x} = \frac{y(x_0)}{\Delta x} + y'(x_0) + O(\Delta x^2) \, . \quad (2.2)$$

If we neglect the error term and solve for the first derivative $y'(x_0)$ we get an approximation to the first derivative at $x = x_0$,

$$y'(x_0) \approx \frac{y(x_0 + \Delta x) - y(x_0)}{\Delta x} \,. \tag{2.3}$$

It is now assumed that the spatial region is a grid such that we have only discrete values of x. For simplicity let's assume a uniform grid spacing such that $x_i = x_0 + i\Delta x$. We now adjust our notation,

$$y'(x_i) = y_x \approx \frac{y(x_{i+1}) - y(x_i)}{\Delta x} = \frac{y_{i+1} - y_i}{\Delta x}. \tag{2.4}$$

Equation (2.1) can then be written as either,

$$y_{i+1} = y_i + \Delta x y_x + \frac{\Delta x^2 y_{xx}}{2!} + \frac{\Delta x^3 y_{xxx}}{3!} + O(\Delta x^4) \tag{2.5}$$

or

$$y_{i-1} = y_i - \Delta x y_x + \frac{\Delta x^2 y_{xx}}{2!} - \frac{\Delta x^3 y_{xxx}}{3!} + O(\Delta x^4). \tag{2.6}$$

We can then proceed with approximating the second derivatives by summing equations (2.5) - (2.6) together and then rearranging the terms to solve for the second derivative, y_{xx}, which gives a centered-difference approximation for the second derivative,

$$y_{xx} \approx \frac{y_{i+1} - 2y_i + y_{i-1}}{\Delta x^2}. \tag{2.7}$$

Note that equations (2.2) and (2.7) are just examples of how to approximate first and second derivatives, however, there are other methods which can lead to different orders of accuracy [24].

We are now in a position to express a PDE as a set of difference equations. Consider the wave equation

$$\frac{\partial^2 y}{\partial t^2} = c^2 \frac{\partial^2 y}{\partial x^2}, \tag{2.8}$$

which has been a workhorse in much of classical physics to describe mechanical and light waves as they arise in acoustics, electrodynamics, and fluid dynamics. The wave equation is a

partial differential equation which means that the underlying function of interest is a function of not one, but multiple independent variables. In the case of the *one* dimensional wave equation, the function we wish to calculate, y, is a function of both the coordinate, x, and time, t. As a result, the following notation will be used throughout the remainder of this thesis in order to be more concise, y_i^n, where the index i is used to refer to the i^{th} lattice point and (n) refers to the time-step at (n). Inserting the finite difference approximations for equations (2.2) and (2.7) the respective time and spatial partial derivatives into the wave equation we get

$$\frac{y_i^{n+1} - 2y_i^n + y_i^{n-1}}{\Delta t^2} = c^2 \left(\frac{y_{i+1}^n - 2y_i^n + y_{i-1}^n}{\Delta x^2} \right). \tag{2.9}$$

We can now rearrange for the value of displacement at position i and time-step $(n+1)$, y_i^{n+1}, which enables us to solve for the next wave-form as it has advanced in time,

$$y_i^{n+1} = 2y_i^n - y_i^{n-1} + \frac{c^2}{\Delta t^2} \left(\frac{y_{i+1}^n - 2y_i^n + y_{i-1}^n}{\Delta x^2} \right). \tag{2.10}$$

Note that we have solved for the wave at future times, y_i^{n+1}, *explicitly* in terms of the displacement at neighboring lattice points and previous time-steps, namely, y_{i-1}^n, y_i^n, and y_{i+1}^n. For this reason, algorithms where future time-steps are calculated as difference equations full of previous time-step terms are called *explicit* finite-difference methods.

A second type of finite difference method can be constructed by reformulating the second spatial derivative in terms of the time-step at $(n+1)$, yielding:

$$\begin{aligned} \frac{y_i^{n+1} - 2y_i^n + y_i^{n-1}}{\Delta t^2} &= c^2 \left(\frac{y_{i+1}^{n+1} - 2y_i^{n+1} + y_{i-1}^{n+1}}{\Delta x^2} \right), \\ y_i^{n+1} - c^2 \Delta t^2 \left(\frac{y_{i+1}^{n+1} - 2y_i^{n+1} + y_{i-1}^{n+1}}{\Delta x^2} \right) &= 2y_i^n - y_i^{n-1}. \end{aligned} \tag{2.11}$$

This equation can no longer be solved for the *i*th position in space at the time-step $(n+1)$ solely in terms of the displacement of the wave, y, at previous time-steps and such an algorithm is called an *implicit* finite-difference method. The displacement y_i^{n+1} must now be obtained by solving a solving a system of equations. The advantage of an explicit algorithm is that it is simpler to implement. However, the main disadvantage of explicit methods is that they can

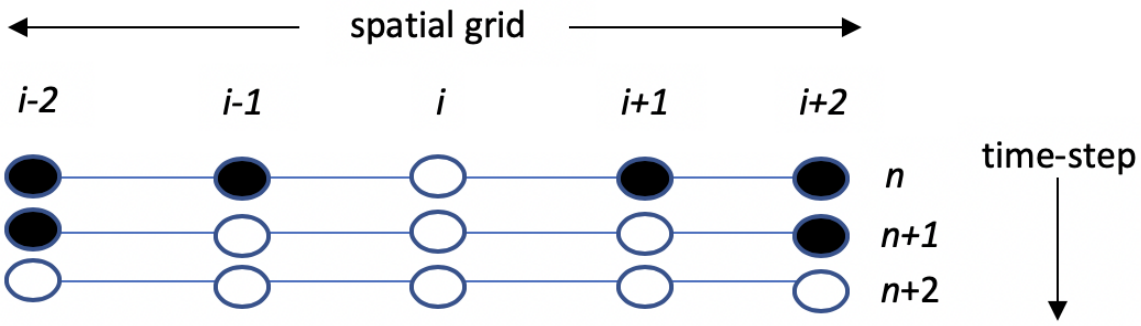

Figure 2.1: A diagram of a numerical stencil showing the relationship between adjacent lattice points and successive time-steps.

suffer from serious numerical instabilities. For explicit methods as written in equation (2.10), disturbances in the fluid must propagate no further than the distance between two adjacent mesh points in a successive time-step. For example, consider the ith lattice point at time-step (n) in Figure 2.1 indicated by a white or hollowed out grid point. A condition placed upon an *explicit* method is that disturbances induced in the wave can propagate no further than to neighboring lattice points at time-step $(n+1)$ indicated again by white or hollowed out lattice points. The additional lattice points that disturbances can travel to are again indicated by white lattice points if we repeat this process for the time-step at $(n+2)$. This constraint is necessary in order for an explicit algorithm to achieve numerical stability and accuracy and is called the Courant condition [24],

$$\frac{c\Delta t}{\Delta x} \leq C_{max}, \tag{2.12}$$

where a typical value of C_{max} is $C_{max} = 1$ or smaller. This can lead to values of Δt that are very small, especially when a system is dispersive. The advantage of an implicit method is that the method is not as sensitive to the Courant condition, i.e, C_{max} can take on values that are significantly larger than 1. The disadvantage to implicit methods is that they are often numerically more intensive and more difficult to implement since they require the solution of a system of equations at each time-step.

2.1 The Navier-Stokes Equations

The example of the wave equation and the algorithms from the previous section are intended to give the reader a taste for the numerical algorithms that can be used to solve the Navier-Stokes equations. The NSE involve the conservation of mass and momentum by relating fluid speed, density, time, and spatial coordinates. The NSE are considerably more complicated than the wave equation so a more sophisticated explicit finite-difference algorithm will be used to solve them. The assumptions placed upon the fluid in the NSE in this project are the following: (1) the fluid is an ideal gas, (2) with viscosity, (3) is compressible (the density is allowed to vary), and (4) the coupling between the temperature and the momentum of the flow is very small and can be ignored, i.e, we make the adiabatic approximation. It is a reasonable approximation for air at room temperature to be considered as an ideal gas, and the third assumption is needed in order for sound to propagate. The reason for the adiabatic assumption is concise enough: sound causes differences in pressure/density that happens quickly compared to the thermal diffusion time. The NSE under the assumptions just listed are given in equations (2.13)-(2.16):

$$\frac{\partial \rho}{\partial t} + \frac{\partial(\rho u)}{\partial x} + \frac{\partial(\rho v)}{\partial y} + \frac{\partial(\rho w)}{\partial z} = 0 \tag{2.13}$$

$$\frac{\partial u}{\partial t} + u\frac{\partial u}{\partial x} + v\frac{\partial u}{\partial y} + w\frac{\partial u}{\partial z} + \frac{c^2}{\rho}\frac{\partial \rho}{\partial x} - \alpha\nabla^2 u = 0 \tag{2.14}$$

$$\frac{\partial v}{\partial t} + u\frac{\partial v}{\partial x} + v\frac{\partial v}{\partial y} + w\frac{\partial v}{\partial z} + \frac{c^2}{\rho}\frac{\partial \rho}{\partial y} - \alpha\nabla^2 v = 0 \tag{2.15}$$

$$\frac{\partial w}{\partial t} + u\frac{\partial w}{\partial x} + v\frac{\partial w}{\partial y} + w\frac{\partial w}{\partial z} + \frac{c^2}{\rho}\frac{\partial \rho}{\partial z} - \alpha\nabla^2 w = 0, \tag{2.16}$$

where u, v, and w are the x, y, and z components of flow velocity; α and c are the kinematic viscosity and the speed of sound in air respectively. Also the pressure variations are related to density by $\Delta P = c^2 \Delta\rho$, where $\Delta P = P - P_0$ is the difference between the pressure of the fluid (P) and atmospheric pressure (P_0), and $\Delta\rho = \rho - \rho_0$ is the difference between the density of the fluid (ρ) and the density of air at atmospheric pressure (ρ_0).

Furthermore, important assumptions that are specific to our simulation of a recorder are (1) that the recorder is located in a small enclosure that is 200 mm $\times 60$ mm $\times 60$ mm and (2)

the walls are modeled with a real (for reflection) and an imaginary (for absorption) components of acoustic impedance.

2.2 Numerical Methods

The NSE are nonlinear and as a result do not have analytical solutions in the general case. In light of this, numerical methods are required to approximate the solutions for the cases of most interest. The numerical method that will be detailed in this section to solve the NSE is the MacCormack predictor-corrector method [25]. This method is a second-order accurate explicit finite difference algorithm that approximates a hyperbolic partial differential equation of any number of spatial dimensions of the form,

$$\frac{\partial y}{\partial t} + a\frac{\partial y}{\partial x} = 0 \tag{2.17}$$

The method operates by first computing an initial value of $\hat{y}_i^{n+1}$, called a *predictor* that is an approximate solution at the next time-step, by using the forward difference for the spatial derivatives [25] in equation (2.18):

$$\hat{y}_i^{n+1} = y_i^n - a\frac{\Delta t}{\Delta x}\left(y_{i+1}^n - y_i^n\right) \tag{2.18}$$

In the second step, known as the *corrector* step, the predictor, $\hat{y}_i^{n+1}$, is used to calculate y_i^{n+1}, called the *corrector*, by taking an average of the forward and backwards differences as shown in equation (2.19):

$$y_i^{n+1} = \frac{1}{2}\left[y_i^n + \hat{y}_i^{n+1} - \frac{a\Delta t}{\Delta x}\left(\hat{y}_i^{n+1} - \hat{y}_{i-1}^{n+1}\right)\right] \tag{2.19}$$

The method easily extends to 3-dimensions and to the NSE in equations (2.13)-(2.16).

Solutions to the NSE that are obtained numerically are known to often suffer from numerical instabilities. To mitigate these instabilities an artificial viscosity term is added [22] into the

NSE. These artificial viscosity terms are described in [23] and are similar in form to the viscosity (α) terms in equations (2.14) - (2.16). These terms are introduced to damp rapid oscillations that can result from numerical instabilities in a (potentially) turbulent system.

2.3 Implementation

Giordano's [22] simulation(s) apply the MacCormack method to the NSE as described in section 2.1 using a custom piece of software written in the programming language, C, and parallelized using the OpenMP application programming interface (API). Due to the magnitude of the computational load, these numerical simulations have been implemented on the supercomputer, Hopper, run by OIT at Auburn University.

Chapter 3

The Physics of the Recorder

3.1 Introduction to the Fundamentals of the Recorder

The recorder is one of the simplest members of the wind instrument family. A recorder player creates an air jet in the channel of the instrument by making physical contact with the instrument and blowing. Self-sustained oscillations then occur in the instrument once the player blows into the instrument at a minimum blowing speed. Recorders can be grouped into two main classes of instruments: renaissance recorders and baroque recorders [1]. Renaissance recorders are defined as the instruments that were built up until the 17^{th} century and baroque recorders are defined as the instruments that incorporate new features that were introduced around the end of the 17^{th} century [1] with relatively minor alterations being made to the instruments since then. Examples of renaissance and baroque style recorders are shown in the figures 3.1 and 3.2.

As can be seen from figure 3.1 recorders from the renaissance period have a nearly cylindrical bore and are typically one solid unit whereas the baroque style instruments tend to have a tapering bore and have jointed sections. Recorders are traditionally made in a few different lengths. The traditional recorder family consists of the soprano, alto, tenor, bass, and sopranino; the sopranino (which is the shortest) having a musical range that is composed of notes on the higher end of the musical spectrum and the bass having a range composed of notes that are on the lower end for that instrument family. The alto recorder has a musical range of two and a half octaves above F4 (342.88 Hz), while the sopranino has a musical range an octave above the alto, and the bass recorder has a musical range that has an octave below the alto recorder.

Figure 3.1: Examples of renaissance recorders [1].

Figure 3.2: Examples of baroque recorders [1].

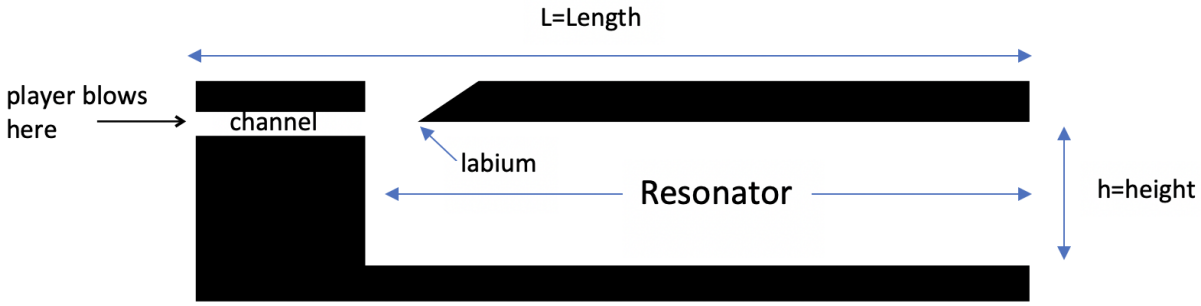

Figure 3.3: A schematic of a cross-section of a recorder looking from the side of the instrument.

For our studies we consider a simple recorder with a square (or rectangular, as in further discussion) cross-section and without tone holes as shown in figures 3.3 and 3.4. Figure 3.3 is a schematic looking at the side of a simplified geometry of a recorder while figure 3.4 is looking down the resonator of this same recorder. The mechanism of sound production for a recorder starts in the channel with a uniform flow imparted in the channel of the instrument as shown in figure 3.5. The channel of a recorder forces an air-jet to be expelled and travel toward the labium; the region between the end of the channel to the tip of the labium is called the window (see figure 3.9) and this terminology will come up in future chapters. At sufficient blowing speeds, an acoustical field is produced in the resonator. Consider figure 3.6. This figure is the result of a simulation of a sopranino style recorder at a blowing speed of $u_0 = 28$ m/s and shows the magnitude of the flow velocity for *one period* of motion. The images in this figure are focused on both the labium and channel, and their alphabetical order corresponds to their sequential order in time. Each image gives a detailed view of the behavior of the fluid motion including the behavior of the air-jet and vortex. Viewing the series of images in alphabetical order illustrates the oscillatory behavior of the air-jet as it oscillates above and below the labium. Likewise, in the same figure, a vortex beneath the labium is coupled to the motion of the air-jet; as the vortex circulates, it causes the interaction necessary for the air-jet to oscillate above and below the labium. The vortex, positioned just below the window and labium, oscillates due to the feedback from the acoustical field in the resonator. This interaction between the air-jet, vortex, and standing pressure waves in the resonator is *the* fundamental mechanism behind the sound production of a recorder and it is this mechanism that will be the focal point of this part of this thesis.

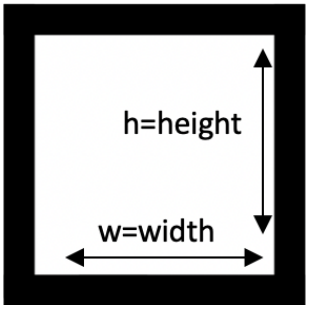

Figure 3.4: A schematic cross-section of a recorder looking from the open end of the instrument (the right) in figure (3.3).

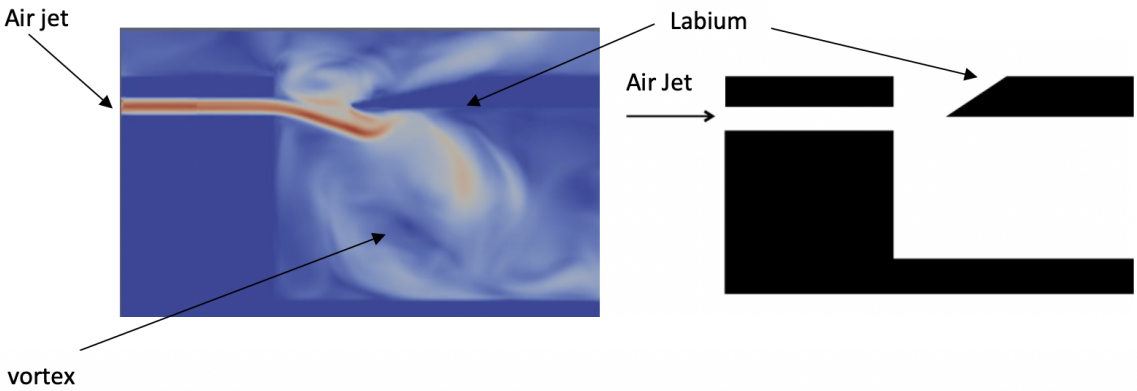

Figure 3.5: Left: Results from one of my simulations illustrating the vortex and the air jet near the labium. Right: A diagram showing the location and geometry of the left side of this figure.

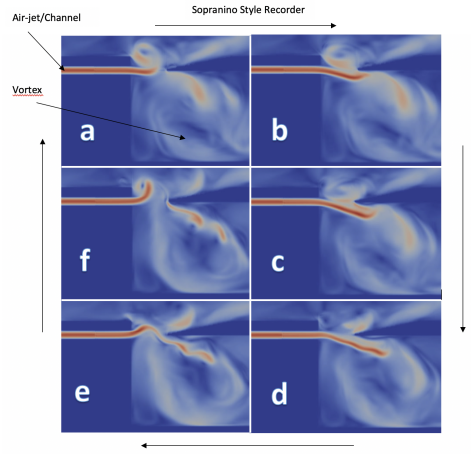

Figure 3.6: The vortex mechanism near the labium that is necessary for a recorder to facilitate self-sustained oscillations for sound production ($u_0 = 28$ m/s).

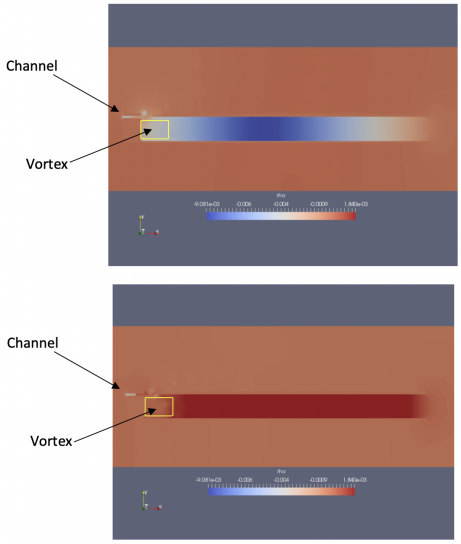

Figure 3.7: Pressure Vs Time graph for a point outside of the recorder that illustrates what a listener might hear from these simulated instruments ($u_0 = 28$ m/s).

As mentioned in chapter 2, solving the NSE yields the density of the fluid ρ and the variation in the ρ can be related to pressure through the relationship $\Delta p = c^2 \Delta \rho$. The pressure oscillations in the resonator are shown in figure 3.7; a red hue indicates a pressure value that is above atmospheric pressure and a blue hue indicates a pressure that is below atmospheric pressure. This periodic motion between high- and low-pressure is a standing pressure/density wave inside the resonator of the recorder.

In our simulations the density of the fluid is recorded at various points inside and outside the resonator of the recorder as a function of time. These density/pressure oscillations are examples of what one might hear if one were standing in the same room as this recorder is being played. An example of these pressure oscillations is shown in figure 3.8.

Thus far we have discussed the basic mechanics behind the sound production of a recorder at particular blowing speed. However, the player can increase the blowing speed in the channel of the recorder by increasing the pressure in her/his mouth all the while maintaining a particular note. At low blowing speeds this note is maintained but at sufficiently large blowing speeds the recorder can jump to the next highest harmonic - a behavior known as *regime change*.

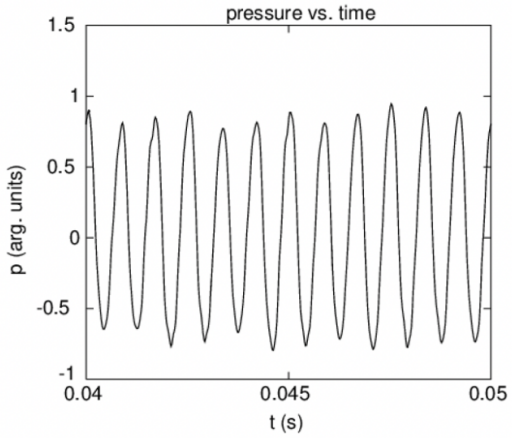

Figure 3.8: ρ vs t graph from a simulation illustrating the pressure/density oscillations in the resonator of the recorder at a blowing speed of $u_0 = 28$ m/s and a fundamental frequency of $f = 1183$ Hz.

3.2 Regime Change in Recorders

As mentioned in the previous section, the recorder exhibits behavior known as regime change where the note being played transitions an octave higher as a result of increasing the blowing speed. For consistency, when discussing a note and its octave, I will refer to the note that is lower in scale as the *base* or *ground note* and its octave as the *octave note*, or more concisely, its *octave*. The blowing speed for which the transition occurs is called the *threshold velocity*. An interesting phenomena that happens in the *bass* recorder is that regime change occurs at relatively low blowing speeds [26] when compared to instruments in the same family that have higher musical compasses, e.g, the sopranino recorder. Regime change at a low blowing speed can be undesirable from a practical standpoint. The transition from the base note to its octave may occur when, perhaps, it might be advantageous to remain on the base. For example, a particular composition might specify for the base note to be played and held or for the base note to be played with more volume.

There are two primary goals in this project: (1) we want to understand why the bass recorder exhibits regime change at a low blowing speed and (2) if possible, we would like to increase the blowing speed at which regime change occurs in the bass recorder by making small changes to the design of the instrument.

We next consider why the bass recorder is different than other instruments in its family. A clue to the answer to this question is found in a paper published in 2010 by Blanc et al [27]; this study performed an in-depth analysis of the dimensions of these recorders and how the different dimensions are related to one another. It was shown that the dimensions of the bass (lowest musical compass) recorder do not scale linearly to the sopranino recorder. Blanc et. al showed that the dimensions scale linearly to the alto recorder, but not to the sopranino recorder. To illustrate this concept, consider the bass recorder which has a musical compass that is two octaves lower than that of the sopranino recorder. This corresponds to an increase of the length of the sopranino recorder by a factor of four. However, if we refer to figure (3.3) and figure (3.4), scaling all dimensions by a factor of four results in an instrument that has a volume that is sixty-four times greater than that of the sopranino recorder. This would not be practical instrument for a human to play - a player would not be able to produce enough volume velocity to fill the resonator of this new recorder, let alone produce sound with the instrument! In other words, if the dimensions from the small sopranino recorder scale linearly to the larger bass recorder, you would be left with an unplayable instrument. It was found [27] that the actual bass recorder has a scaled diameter that is considerably less than that of the sopranino recorder. Our hunch was that the decrease in scaled diameter for the bass recorder alters the air-jet/vortex behavior (see section 3.1) which affects the dynamic range of the base note. We then performed simulations to check this idea.

3.3 Sopranino, Bass Recorder Analogues, and threshold Speed Shifts

Blanc *et al* [27] found that the scaled diameter (diameter/fundamental wavelength) of the bass recorder is 30% smaller than the scaled diameter of the sopranino recorder. This suggested how the simplified recorder design in figure 3.3 could be altered in order to exhibit regime change that is consistent with real bass recorders. The *bass style* recorder design in this project is obtained by decreasing the height of the resonator, h (see figures 3.4 and 3.3), by a factor of 2. A schematic of a cross-section of the *bass style* recorder can be seen in figure 3.10. From this point onward *sopranino style* recorder is used to refer to the recorder design in figure 3.3 and *bass style* recorder is used for recorders with the design shown in figure 3.10.

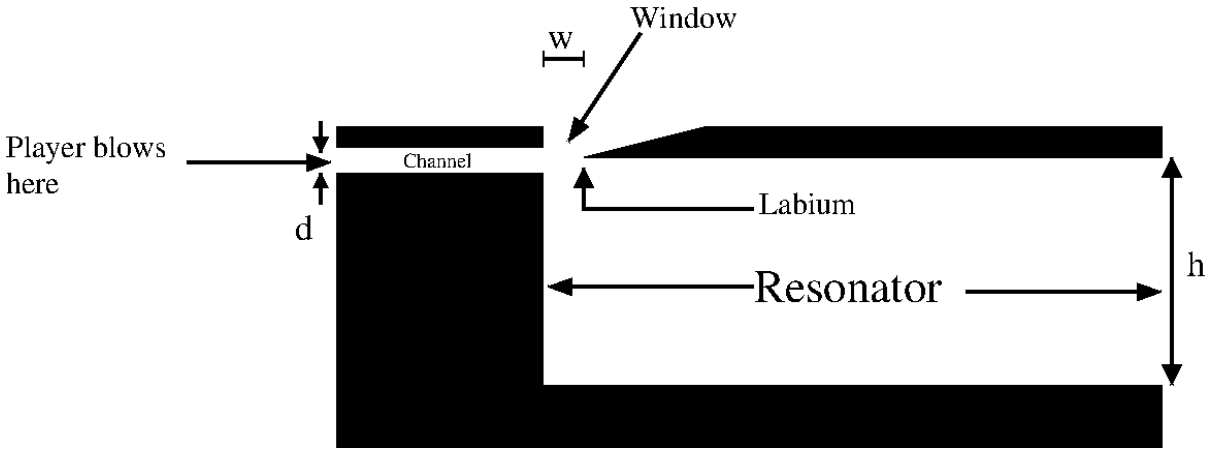

Figure 3.9: A schematic of the general form of the cross-section of a simplified recorder design.

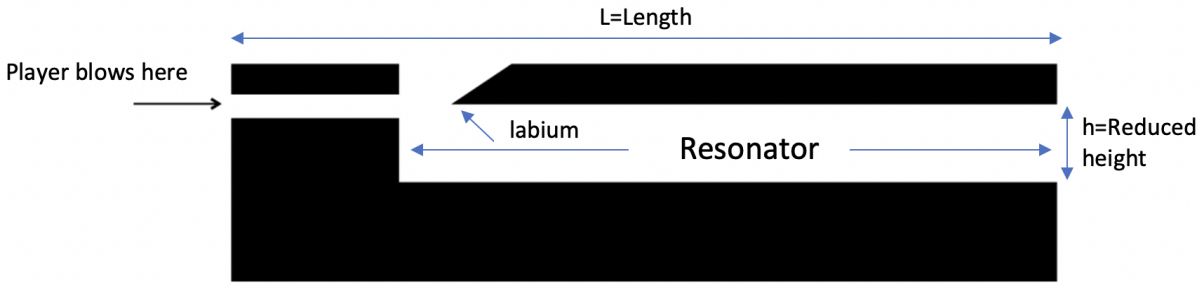

Figure 3.10: A schematic of the cross-section of the unmodified bass-style recorder.

Threshold speed curves are made by plotting the frequency of the harmonic with the largest magnitude of sound power versus the corresponding blowing speed. Our simulations show the effect of decreasing the scaled diameter in figure 3.11. In this figure the dominant frequency is plotted versus the blowing speed inside the channel of the recorder. As can be seen from figure 3.11, the threshold speed for the *sopranino*-style recorder is approximately $u_{RC} = 37$ m/s and the threshold speed for the *bass*-style is approximately $u_{RC} = 28$ m/s. Therefore, we have successfully designed simplified recorder geometries that exhibit the regime change behavior associated with the bass and sopranino instruments.

In figure 3.12 the blowing speed is $u_0 = 28$ m/s for the sopranino style recorder; the first harmonic is the *dominant* harmonic in this spectrum and the second harmonic is nearly nonexistent. Therefore, if a person were to listen to this recorder, they overwhelmingly would hear the first harmonic being played. In contrast, figure 3.13 shows the Fourier spectrum for a bass style recorder with the same parameters; the powers of the first and second harmonic are

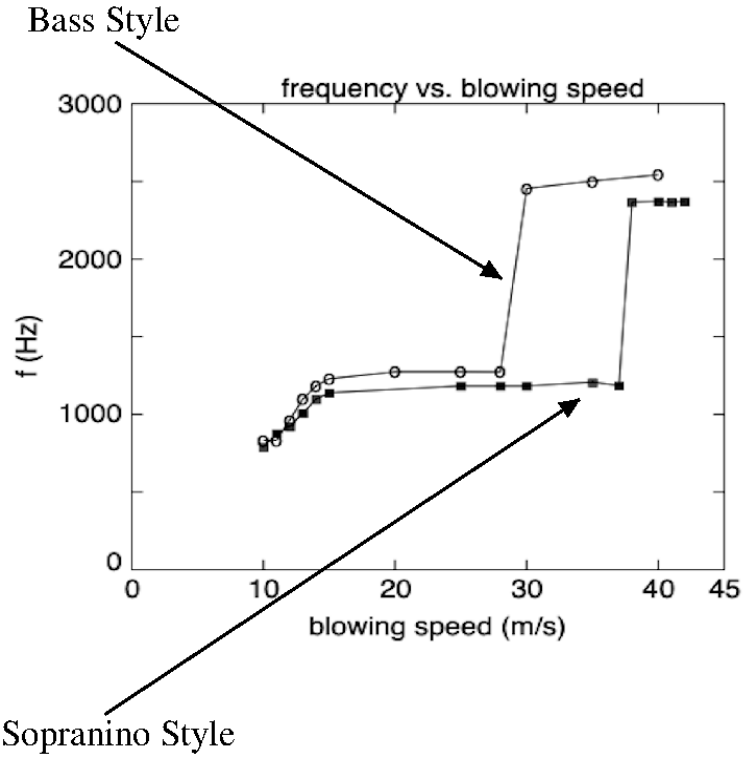

Figure 3.11: Threshold curves for the *sopranino*- and *bass*-style recorders

approximately equal. Since the powers of the first and second harmonic are approximately the same, then $u_{RC} = 28$ m/s represents the *threshold speed* for the *bass* style recorder; threshold speeds are denoted with the special subscripts of 'RC', e.g, u_{RC}. Figure 3.11 illustrates the threshold speed shift between the sopranino- and bass-style recorders and figures 3.12 and 3.13 reinforce that illustration by showing the sound spectra at the approximate threshold speed for the bass-style recorder. To summarize: the 10mm height x 10mm width *sopranino* style recorder, maintains the first harmonic at blowing speed of up to approximately $u_{RC} = 37$ m/s, whereas the 10 mm height x 5mm width *bass* style recorder maintains the first harmonic up to only a reduced blowing speed of up to approximately $u_{RC} = 28$ m/s. This is precisely the behavior seen when comparing the real sopranino and bass recorders.

3.4 Threshold Speed Shift and the Link to Vorticity

In the preceding section, we saw how the bass style recorder has a significantly reduced threshold speed when compared to the sopranino style recorder. In the proceeding discussion, the air-jet/vortex interaction is analyzed in an attempt to find clues as to how to mitigate the regime

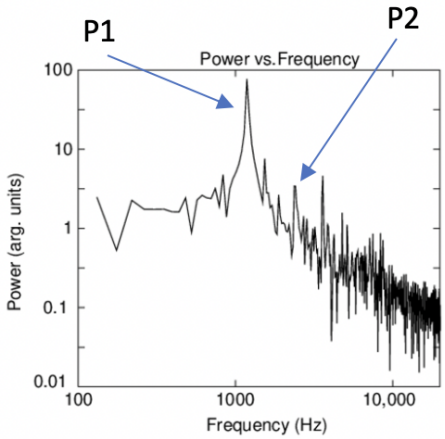

Figure 3.12: Fourier spectrum for the sopranino style recorder (10 mm $\times$10 mm) $u_0 = 28$ m/s. The label P1 indicates the power of the first harmonic.

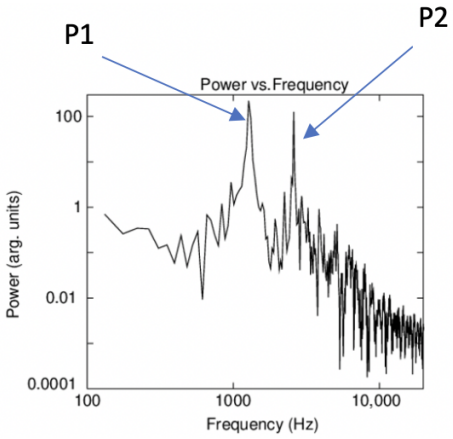

Figure 3.13: Fourier spectrum for the bass style recorder (10 mm $\times$ 5 mm) $u_0 = 28$ m/s. The labels P1 and P2 indicate the power of the first and second harmonic respectively.

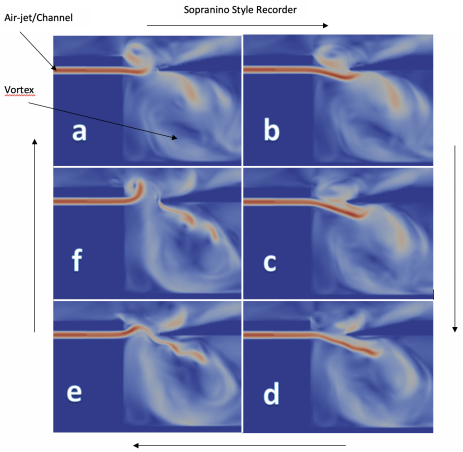

Figure 3.14: The vortex mechanism for a sopranino style recorder (10 mm $\times$10 mm) at ($u_0 = 28$ m/s) for one period of motion.

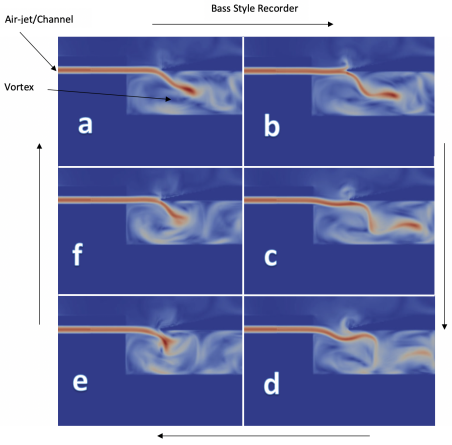

Figure 3.15: The vortex mechanism for a bass style recorder (10 mm $\times$ 5 mm) at ($u_0 = 28$ m/s) for one period of motion.

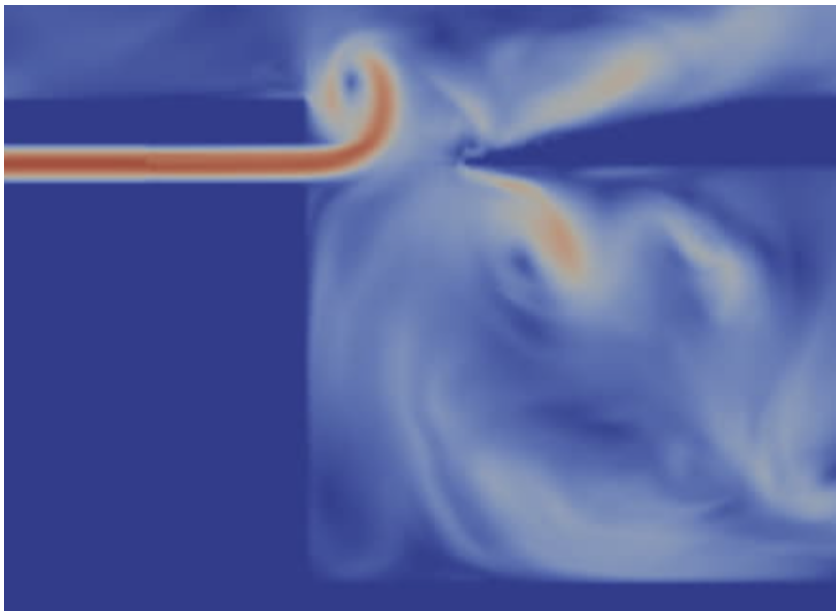

Figure 3.16: Simulation for a sopranino style recorder at $u_0 = 28$ m/s. Note the position of the air-jet above the labium.

change issue with the bass style recorder. The oscillations of the air jet are produced by interaction with the pressure oscillations in the resonator. This is nicely illustrated in figures 3.14 - 3.15. There are also a few clues within figures 3.14 - 3.15 that suggest how we can alter the geometry of the bass style recorder in order to increase its threshold speed; in the proceeding discussion each of the clues will be discussed on-by-one.

The first qualitative behavior that we shall focus on is the vortex beneath the labium. If we compare figures 3.14 and 3.15, then it can be seen that the vortex of the sopranino style recorder in figure 3.14 is significantly larger than the vortex for the bass style recorder in figure 3.15. In addition, the vortex for the sopranino style recorder is more defined as can be seen from figures 3.14 and 3.15. If we refer to figure 3.14, the vortex for the sopranino style recorder simulation appears to have a consistently circular shape whereas the the shape of the vortex in the bass style simulation in figure 3.15 seems to be approximately elliptical with slight changes to the shape about midway through the period of motion. This indicates the strong effect that the floor of the resonator has.

The next behavior that we shall focus on deals with the behavior of the air-jet. In figures 3.16 - 3.17, a sopranino and bass style recorder are simulated at a blowing speed of $u_0 = 28$ m/s

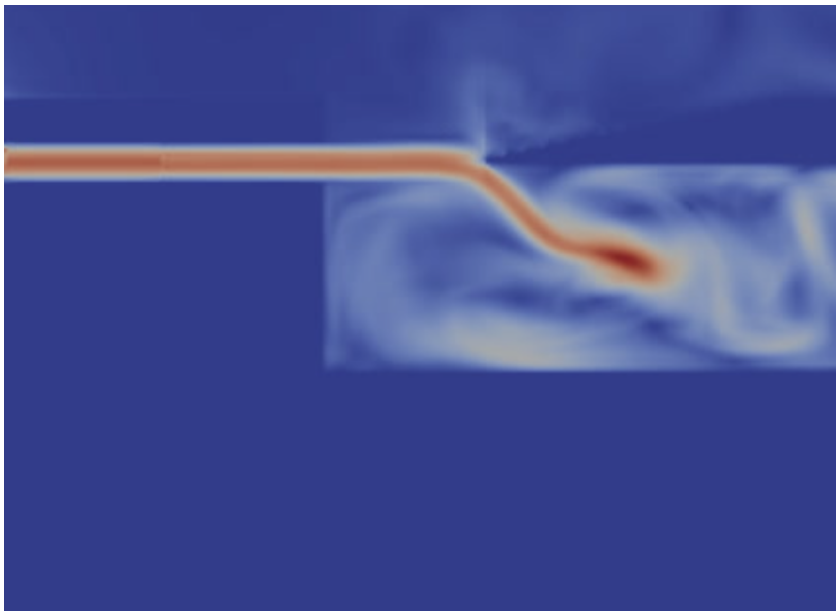

Figure 3.17: Simulation for a bass style recorder at $u_0 = 28$ m/s. Note the position of the air-jet at the height of the labium.

and the region where the air-jet, labium, and vortex is magnified. If we compare both of these figures, then it can be seen that the air-jet for the sopranino style recorder (figure 3.16) reaches a much higher distance above the labium than the air-jet of the bass style recorder (figure 3.17). Both of these figures are of the air-jet at the highest point above the labium for each respective instrument.

In summary, modifications to the length of the resonator will result in a higher or lower fundamental harmonic frequency, which in turn, determines the higher order harmonic frequencies of the recorder. It appears that any modifications to the *shape* of the resonator will shift the threshold speed of a particular instrument by affecting the interaction between the air-jet, vortex, and the acoustic field in the resonator. In the next section, we use the differences in fluid motion (air-jet and vortex) between the sopranino style and bass style recorders to select the alterations to the geometry of the bass style recorder that will increase its threshold blowing speed.

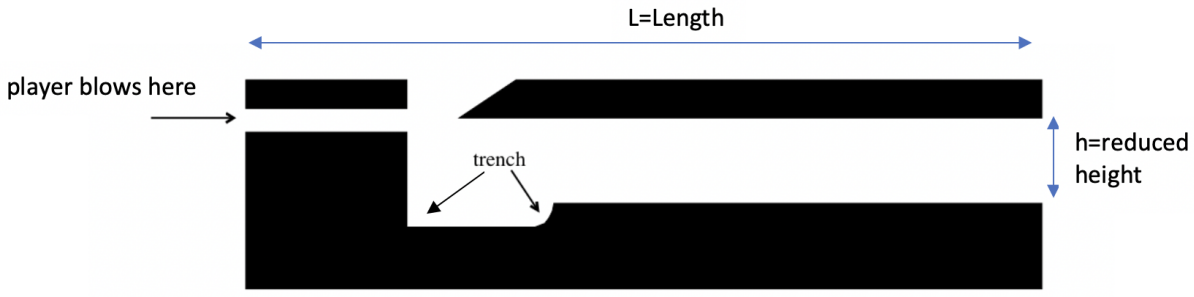

Figure 3.18: A schematic of the cross-section of the modified bass-style recorder. Please note the trench in the bottom left-hand corner of the resonator.

3.5 Mitigating the Threshold Shift in the Bass Style Recorder

At this point, it has been established that the air-jet oscillates by interacting with a vortex beneath the labium, and this vortex forces the air-jet and the acoustic field in the resonator to oscillate synchronously. The vortex for the bass style recorder is significantly smaller than the vortex for the sopranino style recorder. In addition, the vortex in the bass style recorder appears to be elliptical, interacts strongly with the bottom wall of the resonator, and can be slightly "amorphous". This suggests that the vortex for the bass style recorder needs to have enough space to increase in size and maintain a more well-defined shape. We therefore explored the behavior of the bass-style recorder in which a section of the "floor" of the resonator beneath the labium is removed or "*scooped*" out to produce a modified bass style recorder. An example of this modified cross-section can be seen in figure 3.18.

Figure 3.19 is a simulation for one period of motion of the modified bass style recorder at a blowing speed of $u_0 = 28$ m/s; when compared to figure 3.20, the vortex in the modified bass style recorder is significantly larger and has a more well-defined shape than the vortex in the unmodified bass style recorder. In addition, the air-jet in the modified bass style recorder reaches a greater distance above the labium than that of the unmodified bass style recorder. Now that the vortex in the modified bass style recorder has properties more like those of the sopranino style recorder, it is time to see some quantitative results for the threshold speed. In figures 3.21 and 3.22, the Fourier spectra of the sound for both the bass-style and modified bass-style recorders at the same blowing speed of $u_0 = 28$ m/s are given. It should be noted that

the first harmonic in the modified bass style spectrum (figure 3.22) is the dominant harmonic and therefore has not yet achieved threshold. On the contrary the powers of the first and second harmonic are approximately equal in the spectrum for the unmodified bass style recorder (figure 3.21) and is therefore at the approximate threshold blowing speed. Together, these four figures 3.19 - 3.22 illustrate that changing the shape of the resonator seems to alter the interaction between the air-jet and the vortex and therefore increases the threshold speed for the bass style recorder. This suggests that enlarging the local resonator height, for the bass-style recorder, where the vortex is formed might restore the vortex-air jet interaction that was once seen for the alto-style recorders.

Thus far it has been shown that the modified bass-style recorder has an increased threshold blowing speed due to altering the shape of the resonator just below the labium. It is useful to also show the spectra at a higher blowing speed to see the behavior of both the modified and unmodified bass-style recorders. In figure 3.23 and 3.24 we plot the same two spectra but we now increase the blowing speed from $u_0 = 28$ m/s to $u_0 = 35$ m/s. From these two figures, 3.23 and 3.24, it can be seen that the modified bass-style recorder is *still* able to maintain the base note as the clearly dominant frequency. Meanwhile, the octave is the dominant note of the unmodified bass-style recorder. This is certainly promising behavior. We can also plot the power at these two frequencies versus the blowing speed to get a sense of the threshold speed for both the modified and unmodified bass-style recorders. These plots show in more detail how the addition of the trench in the resonator of the recorder mitigates the sensitive threshold speed behavior. Figure 3.25 shows a threshold speed of approximately $u_{RC} = 28$ m/s for the bass-style recorder without the addition of the trench in the resonator of the recorder. Figure 3.26 shows a threshold speed of approximately $u_{RC} = 37$ m/s for the modified bass-style recorder. From figures 3.25 and 3.26 and the threshold speeds that were just mentioned, the simulations show that the addition of the trench accomplishes its task of widening the dynamic range at which the first harmonic can be held by the bass style recorder, i.e, the player is able to play the first harmonic over a wider range of values of blowing speeds thus making it easier to maintain that harmonic. Lastly, it is time to address the breakdown in monotonicity that occurs between the speeds of 25 m/s - 28 m/s in figure 3.25. In figure 3.26, the power of the first and

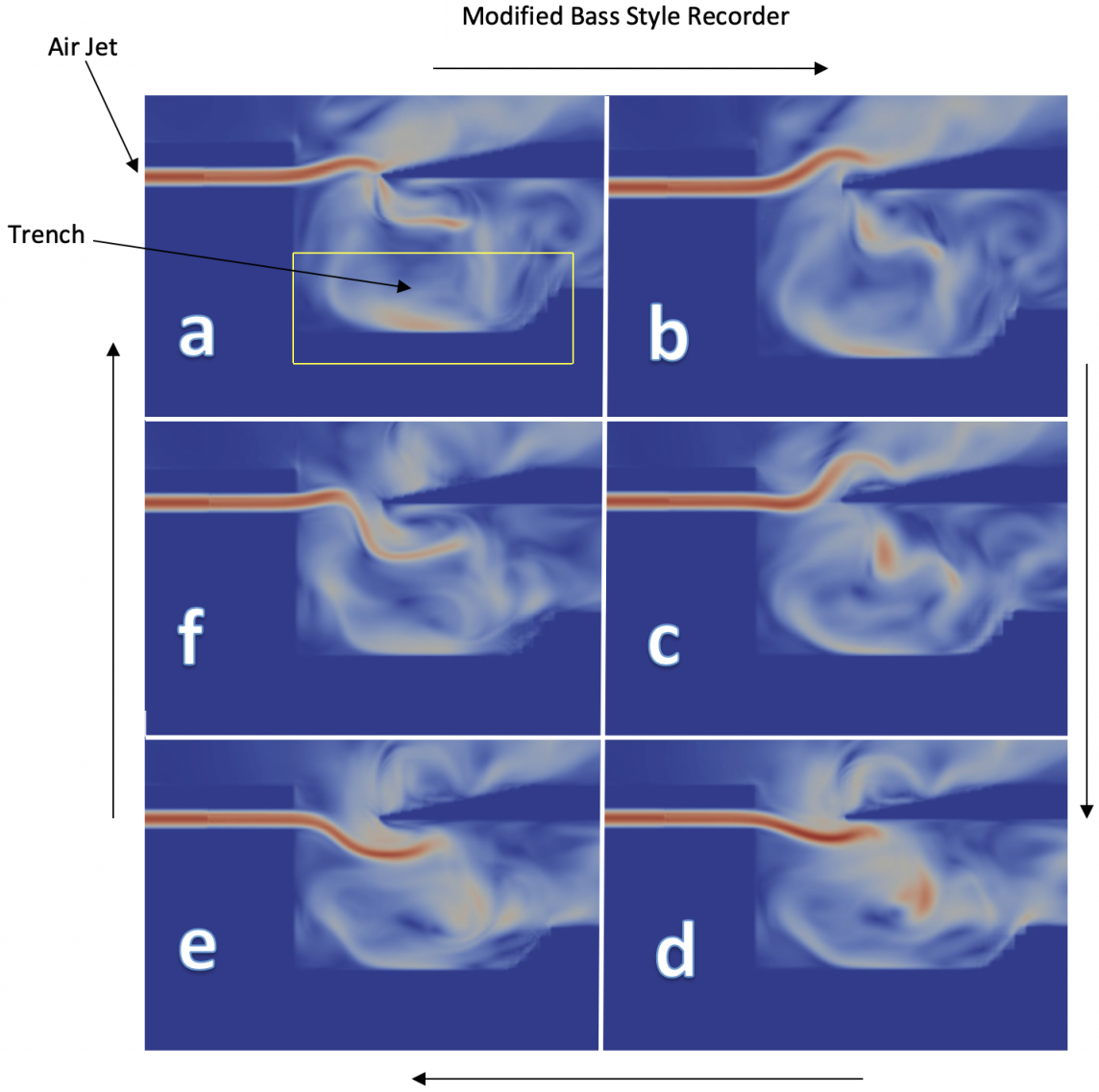

Figure 3.19: Vortex pattern for a modified bass style recorder for one period of motion at a blowing speed of $u_0 = 28$ m/s.

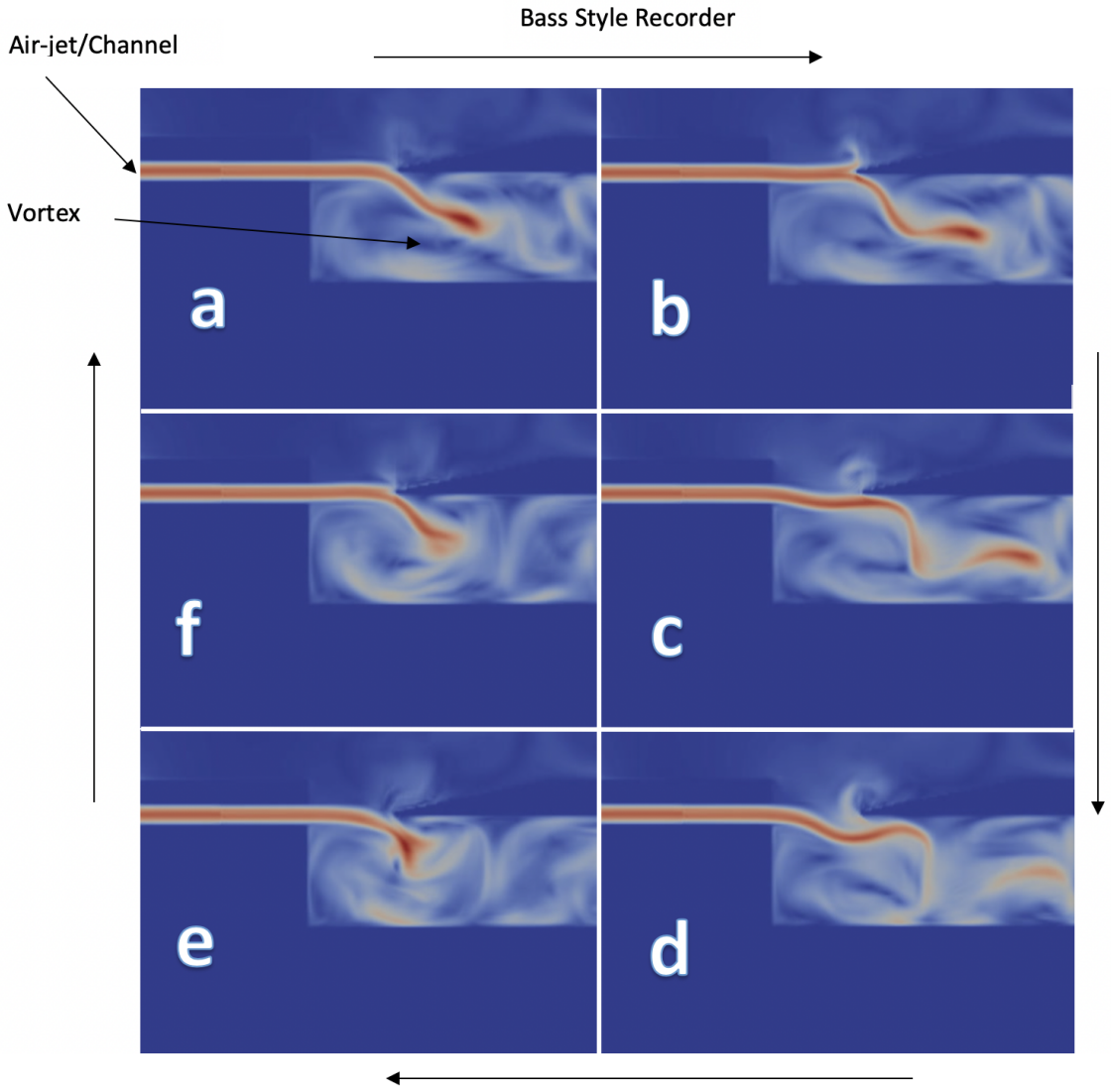

Figure 3.20: Vortex pattern sequence for a bass style recorder for one period of motion at a blowing speed of $u_0 = 28$ m/s.

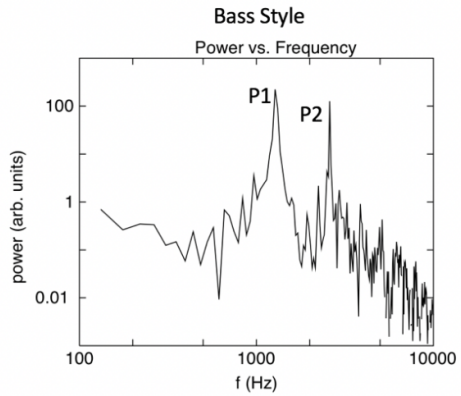

Figure 3.21: Fourier spectrum for the unmodified bass-style recorder at $u = 28$ m/s.

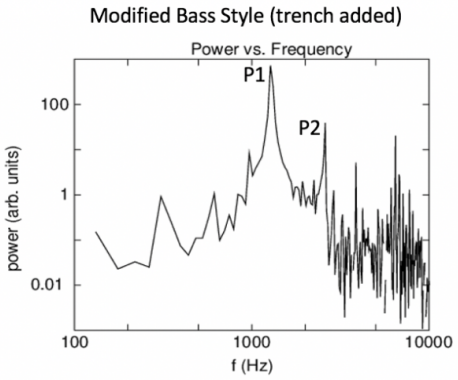

Figure 3.22: Fourier spectrum for the modified bass style recorder at $u = 28$ m/s.

second harmonic steadily *increases* for increasing blowing speeds in the region 20 m/s - 35 m/s; the first harmonic is approximately an order magnitude greater in power than the second harmonic in this region. There is then a short region (35 m/s - 37 m/s) where the power of the first harmonic *decreases* as the power of the second harmonic begins to *increase* as it begins to dominate the sound spectrum. In figure 3.25 the power of the first and second harmonic steadily begin to *increase* for increasing blowing speeds. Then, at around 25 m/s, the power of *both* the first and second harmonic begin to *decrease* for about 3 m/s. Afterwards, the second harmonic then increases in power as it begins to dominate the spectrum. This behavior was first observed in the simulations via the threshold speed curves as seen in figure 3.25 and it was again observed while performing experiments on 3D printed recorders of similar design. When experimenting with the bass style recorders, it was observed that once the channel speed reached a value as that approximately seen in figure 3.25 the recorder begins to whisper while maintaining faint harmonics. This behavior is not yet fully understood and needs future study.

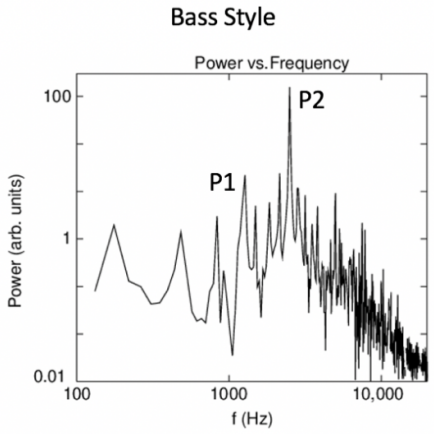

Figure 3.23: Fourier spectrum for the unmodified bass-style recorder at $u_0 = 35$ m/s.

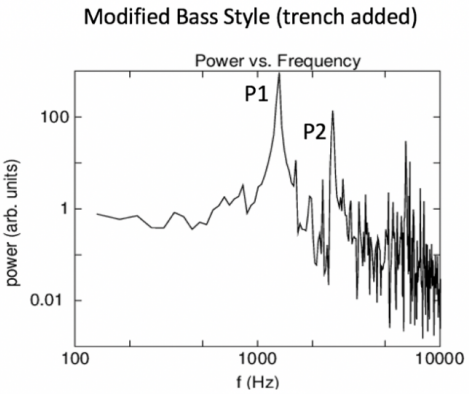

Figure 3.24: Fourier spectrum for the modified bass style recorder at $u_0 = 35$ m/s.

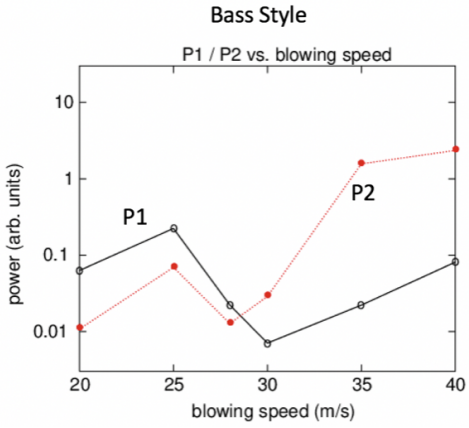

Figure 3.25: Threshold speed curve for the unmodified bass-style recorder.

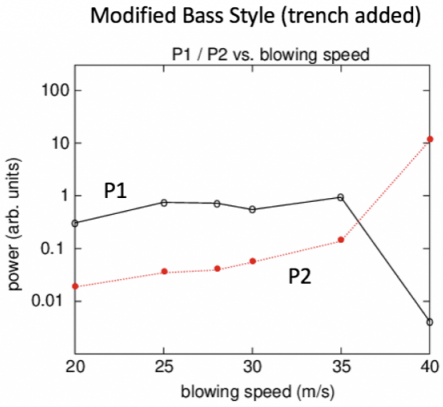

Figure 3.26: Threshold speed curve for the modified bass-style recorder.

Chapter 4

From Simulations to Reality: Constructing Physical Recorders

Thus far, we have discussed the fundamentals of the recorder, the possible implications that occur from altering the geometry of the recorder, and the numerical methods necessary to solve the NSE in these simulations. Experimentation is needed in order to validate the simulation results from chapter 3. In the proceeding four sections we review the design of the simulated square/rectangular recorders from chapter 3, briefly survey the modeling software and 3D printers that were used to make the physical recorders, and describe the finished recorders. Therefore, this chapter is an overview on how to make the recorders. Results for experiments with these recorders and their comparison to the simulations are presented in chapter 5.

4.1 Recorder Design

In this section the designs of three different recorders are given in enough detail that they can be reproduced for future study. First the sopranino style recorder will be described, followed by the bass style recorder, and then a description of the modified bass style recorder.

4.1.1 Sopranino Style Recorder Dimensions

The basic structure of all the recorders is a simple cartesian design, i.e, the geometry is based on a rectangular/square geometry. The sopranino is the ”parent” recorder because the other two recorders can be obtained by simple alterations to the design of the sopranino recorder. This cartesian design was chosen because: 1) such a design simplifies the implementation of the simulations *and* the physical recorders, 2) the simple designs of the recorders presented in this

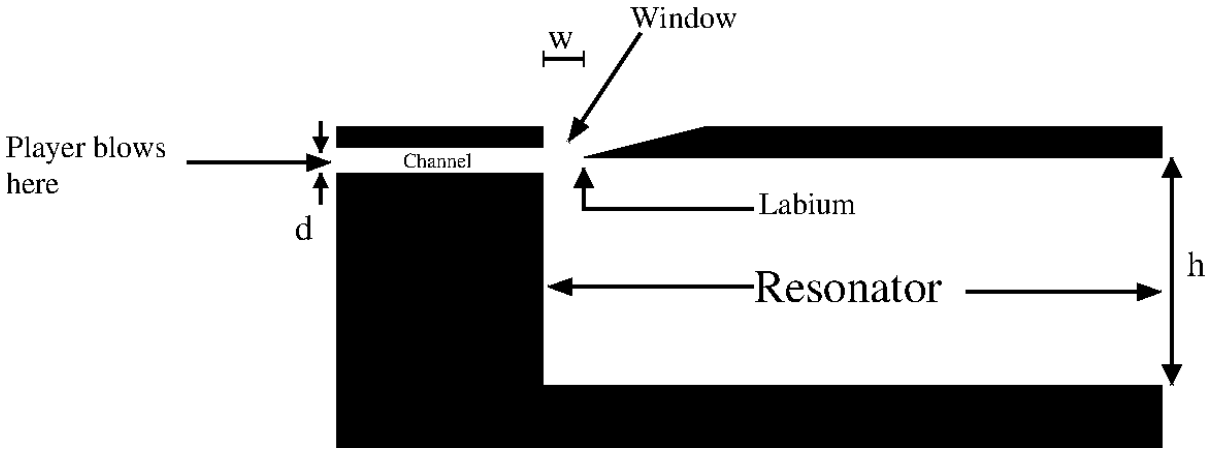

Figure 4.1: A schematic of the general form of the cross-section of a simplified recorder design.

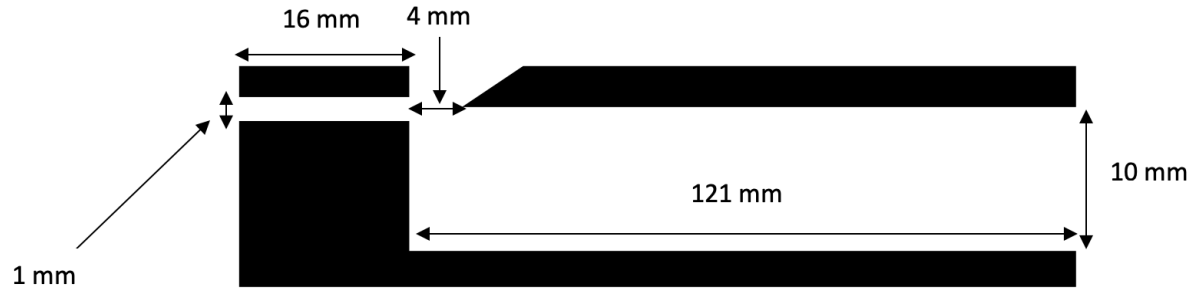

Figure 4.2: Schematic of the cross-section of the sopranino style recorder. Note the dimensions are given.

project are sufficient in order to capture the behavior associated with real recorders that have a cylindrical geometry, and lastly 3) the shape of the cross-section should not matter since the wavelength of the sounds they produce is much greater than the diameter. The geometry of the sopranino recorder can again be seen in figures (4.2) and (4.3), but this time, the most important dimensions are given in addition. Please make a special note of the dimensions of the window w (see figure 4.1) and the channel height d (again, see figure 4.1). From chapter 3, the window is the distance from the end of the channel to the tip of the labium. For convenience figure 4.1 illustrates both the window w and channel height d. The ratio of the window to the channel height has a value of 4 which is standard for the instrument [22, 28].

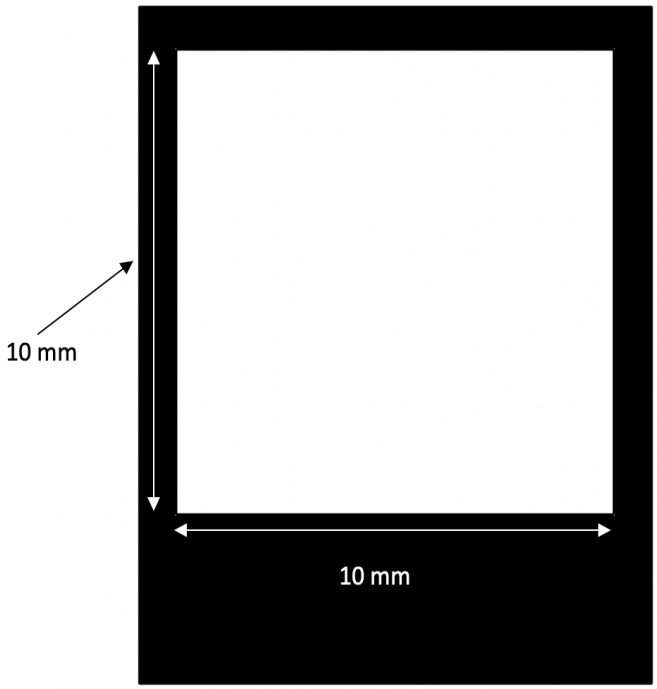

Figure 4.3: Schematic of the cross-section of the sopranino style recorder looking down the resonator of the recorder as viewed from the open end (the end at right in fig. (4.3). Note the dimensions given.

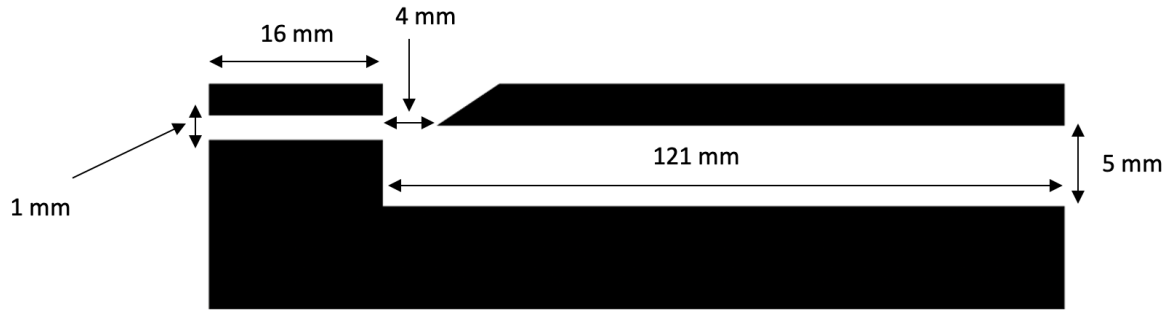

Figure 4.4: Schematic of the cross-section of the (unmodified) bass style recorder. Note the dimensions are given.

4.1.2 Bass Style and Modified Bass Style Recorders

In the previous subsection the geometry of the parent recorder, i.e, the sopranino style recorder has been established. Next we describe the designs of the unmodified and modified bass style recorders. The dimensions of the bass style recorder can be seen in figure (4.4 - 4.5). Note that the only difference between the sopranino and bass style recorder is the height of the resonator.

The last cross-sections to be presented are for the modified bass style recorder. Note that the dimensions are the same as that of the (unmodified) bass style recorder except for the addition of the trench in the bottom floor of the resonator just below the labium. In addition, it is noteworthy that it is only necessary for the trench to be 2 mm deep resulting in a local resonator height of 7 mm and not 10 mm which is the resonator height for the sopranino style recorder. The trench's depth of 2 mm was chosen after running many simulations of varying trench geometry. Parameters such as the height (along the y-axis), length (along the x-axis), shape (e.g a rectangular trench versus a smooth parabolic trench) were varied in these simulations in order to find which geometry had the greatest effect in altering the regime change behavior of the bass-style recorder. By comparing the regime change threshold speeds for the fundamental harmonic, the trench geometry in figure (4.6) was found to have the greatest effect.

4.2 Designing Recorders with AutoCAD

We decided to make the recorders that matched those instruments from the simulations of chapter 3 in order validate the results of the simulations. In addition, we decided to utilize 3D

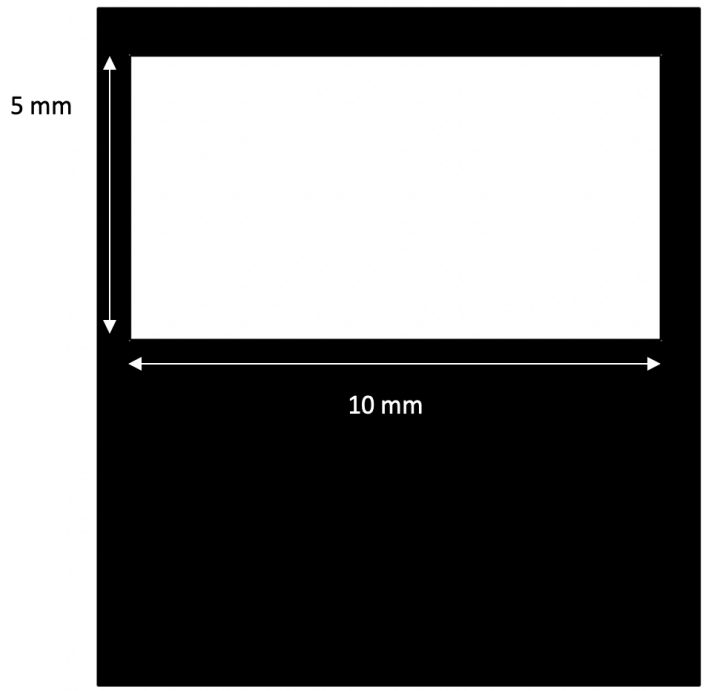

Figure 4.5: A schematic of the cross-section of the (unmodified) bass style recorder looking down the resonator of the recorder as viewed from the open end (the end at right in fig. (4.4)). Note the dimensions are given.

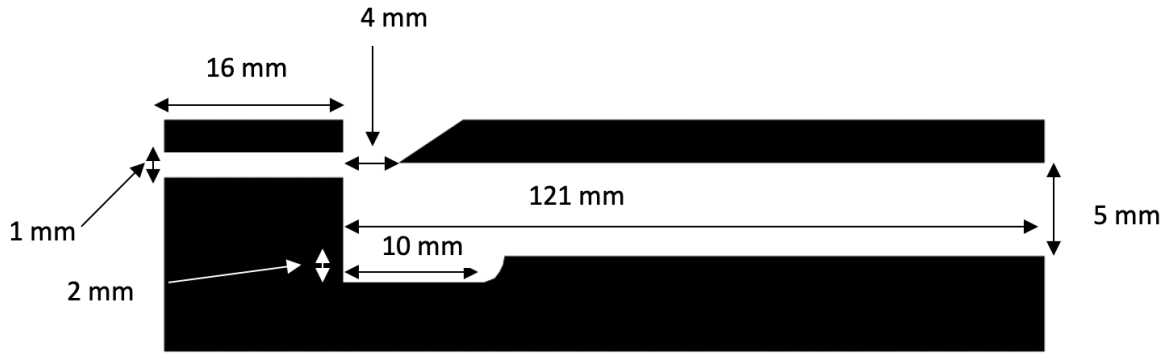

Figure 4.6: A schematic of the cross-section of the modified bass style recorder. Note the dimensions are given.

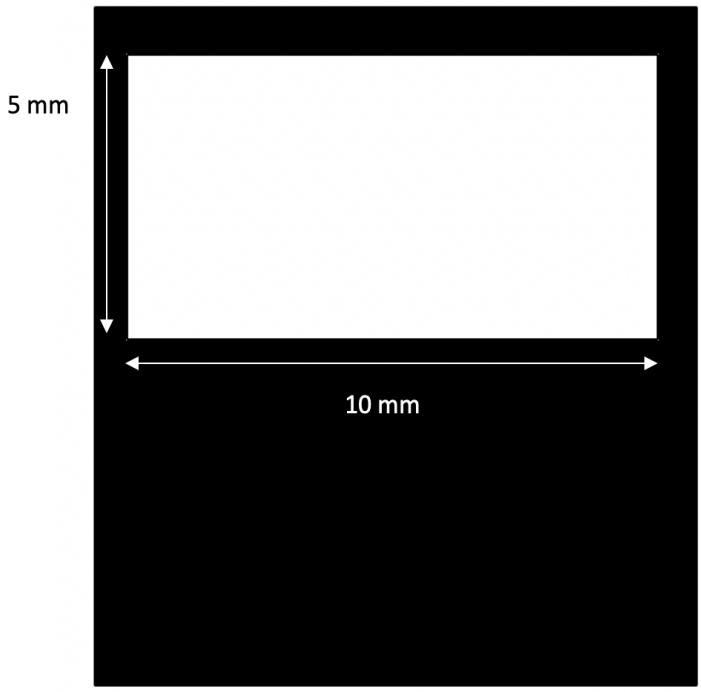

Figure 4.7: A schematic of the cross-section of the modified bass style recorder looking down the resonator of the recorder as viewed from the open end (the end at right in fig. 4.6) Please note the dimensions are given.

AutoCAD Command List	
Command List	Description
LINE	Creates straight line segments
PLINE	Creates a 2D polyline
EXTRUDE	Creates a 3D solid or surface by extruding a 2D object
JOIN	Joins similar object to form a single, unbroken object
UNION	Combines selected 3D solids or 2D regions by addition
PLANESURF	Creates a planar surface
MEASUREGEOM	Measures the distance between two points or along a polyline
ERASE	Removes objects from a drawing
SPLINE	Creates a smooth curve that passes through or near specified points

Table 4.1: A list of the commands used in AutoCAD to make the recorders for 3D printing

printing in order to rapidly fabricate prototypes made out of plastic; plastic is a material that recorders are typically made out of. We first designed drawings of the recorders in AutoCAD. Afterwards, we used a 3D printer to print the recorders from the AutoCAD drawings.

This section gives a brief overview as to how these recorders were modeled using the AutoCAD software. AutoCAD is a software that allows users to draw objects within the AutoCAD environment; generally the intention behind a CAD drawing is to have some machine, or device, fabricate the object in the drawing. In our case of course, the intention was to have a 3D printer fabricate the recorders.There are a variety of both open-source and proprietary drafting software that are available on the market today and there are entire books that go into extensive detail on how to use each one. Such a detailed treatment is beyond the scope of this dissertation. In addition, the recorders from the simulations of chapter 3 can be made with a small handful of AutoCAD commands in a free version of AutoCAD 2015.

4.2.1 AutoCAD Commands

This subsection lists and describes each of the AutoCAD commands that were used in the modeling of each of the recorders that were made with a 3D printer (to be discussed in section 4.3). A full list of the commands used for modeling the recorders in AutoCAD can be found in table (4.1).

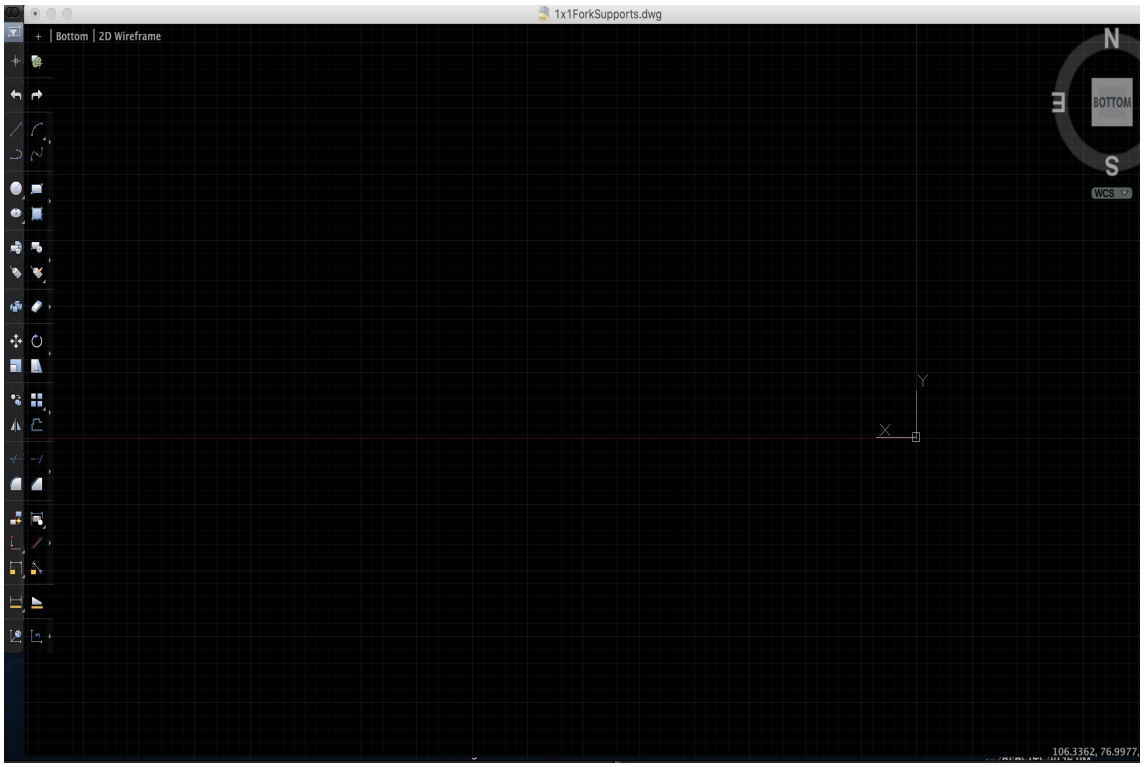

Figure 4.8: A visual of what AutoCAD (2015) looks like before anything is drawn.

4.2.2 Designing Recorders: Step 1

Opening up AutoCAD results in a screen/workstation that looks similar to the one in figure (4.8). The toolbar on the left-hand-side of the screen contains most of the commands that are needed to make the recorders; the others can simply be typed in. There are 4 basic steps that are needed in order to design a recorder in AutoCAD and this subsection will describe the first step.

The first step is to draw the outline of the recorder using one of the following commands: LINE or PLINE. The LINE command draws a single line object and will need to be called after each use. The advantage to LINE is that if there is a mistake in one of the segments of the recorder outline, you can easily use the ERASE command to erase that single undesired line segment and then continue drawing at the point just before the mistake was made. After the particular cross-section of the recorder is drawn, the JOIN command is needed in order to combine each of the individual line segments into a single 2D object. The other option is the command PLINE which is short for polyline. The PLINE command performs the same

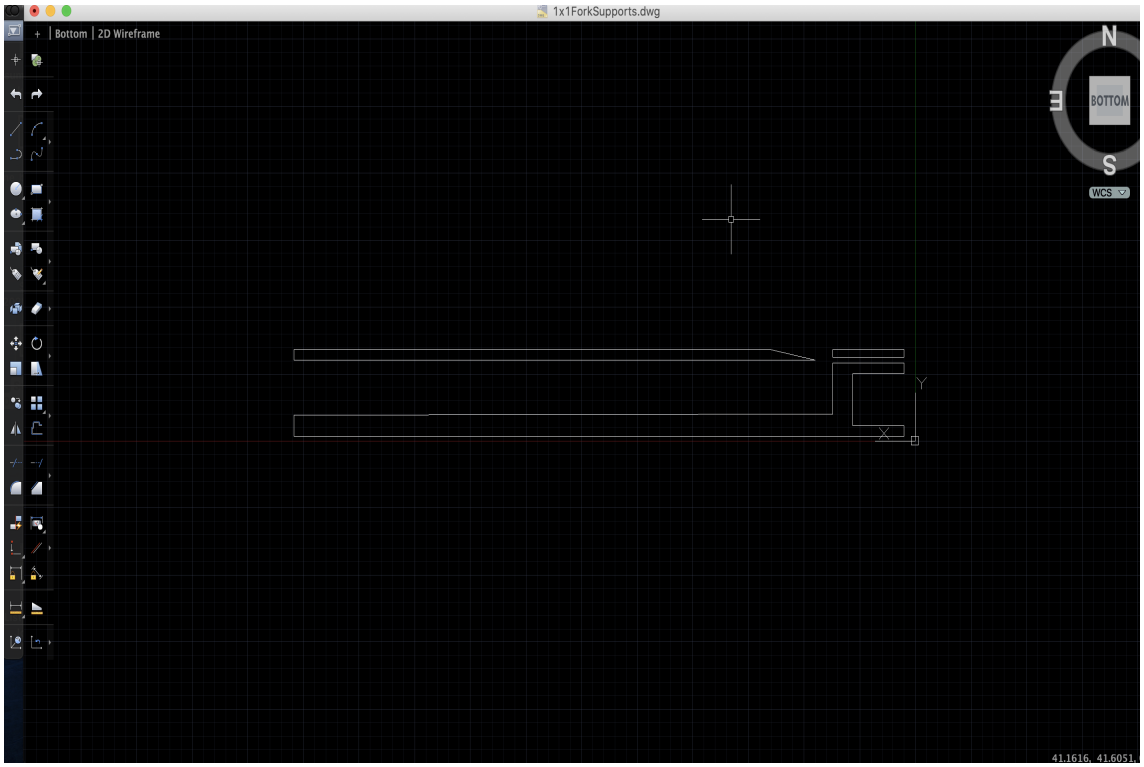

Figure 4.9: A visual of what the finished cross-section looks like in AutoCAD after step 1 is performed. Note that the recorder is flipped to the right.

action as that of the LINE command except that PLINE automatically JOINS each segment into a 2D object, so explicit use of the JOIN command is not needed. The disadvantage of the PLINE command is that if a mistake is made in a particular cross-section, then you will need to erase that cross-section and start over. The advantage of PLINE is that you only have to call PLINE once per cross-section. Figure (4.9) shows what a finished lateral cross-section looks like before you need to move onto the extruding process (next step). There are a total of 3 cross-sections that make up the recorder

There is a difference in the design of the recorder presented here and the original design from figure (4.2) that should be noted. In figure (4.9), the bottom right corner has been extended which adds a lip below the channel of the recorder giving the right-hand side of the recorder a ”tuning fork” look. In figure (4.10) the area around the labium has been magnified and the different parts of the recorder has been labeled; in addition the ”tuning fork” lip has been labeled as well. This addition to the geometry was added due to the way the 3D printers fabricate the recorders. The 3D printer used in this project applies a layer of hot plastic one at a

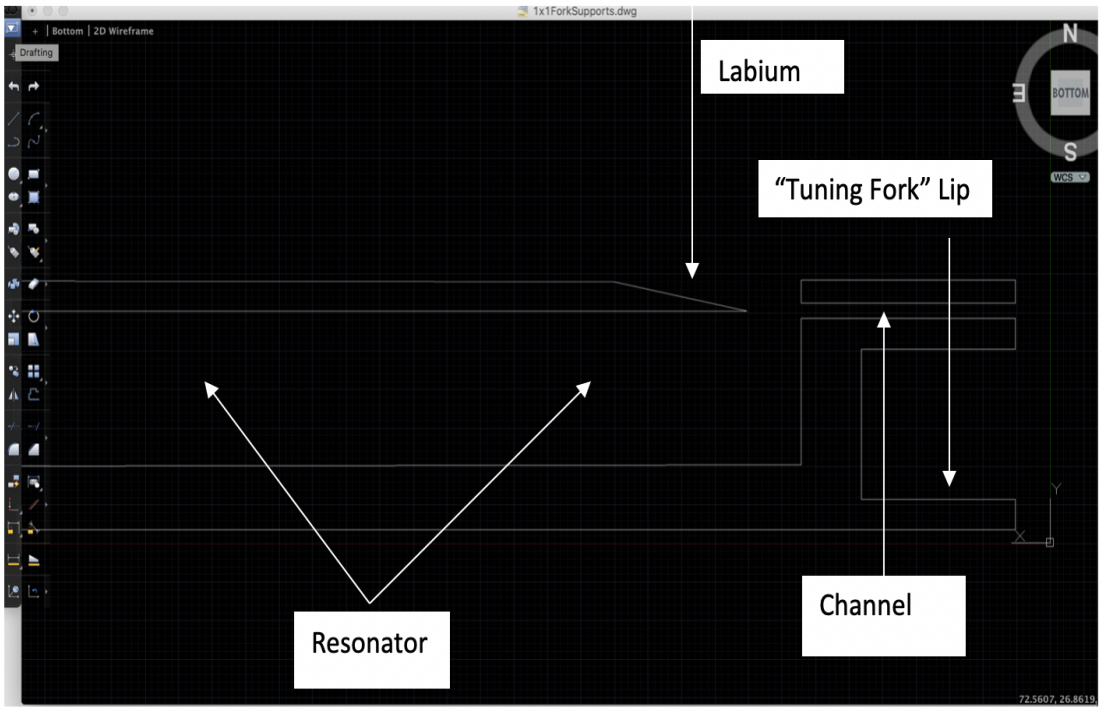

Figure 4.10: A visual of what the finished cross-section looks like in AutoCAD after step 1 is performed. In this figure, the area around the labium and channel has been magnified in order to display the most important components of the recorder.

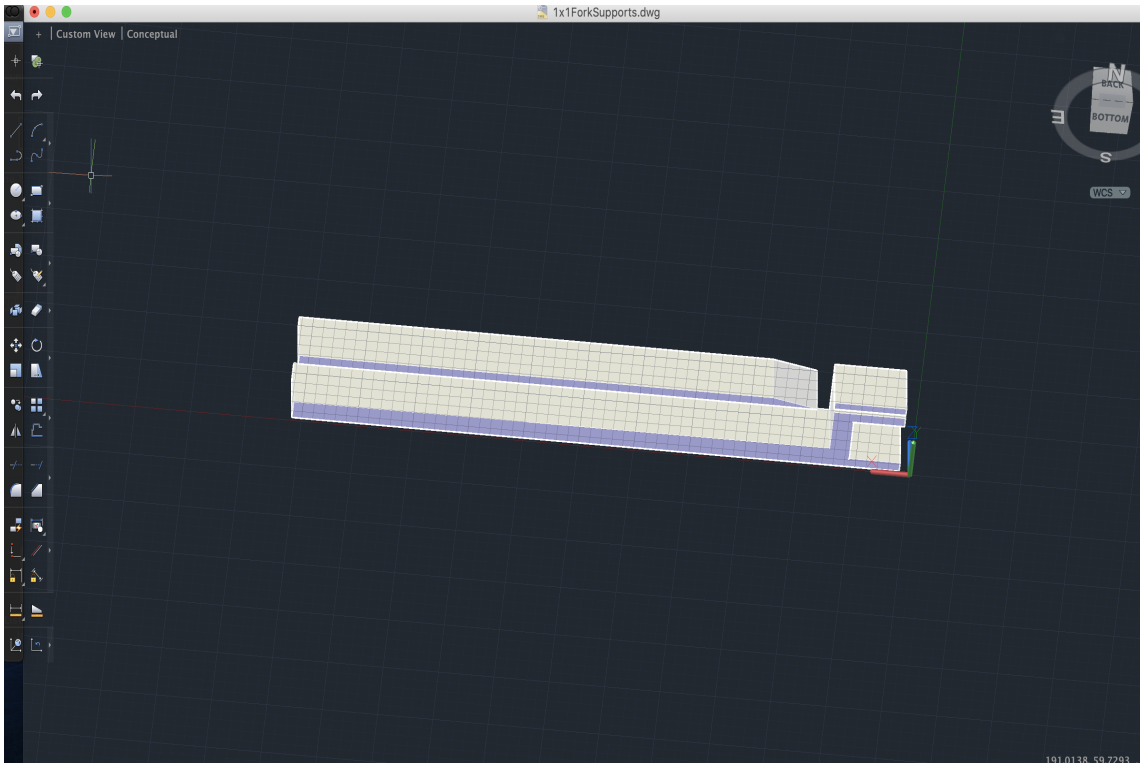

Figure 4.11: A visual of what the extruded cross-sections look like in AutoCAD after step 2 is performed.

time effectively building the instrument up one layer at a time. The additional lip on the bottom was added for stability so the recorder could be printed channel down and *resonator* up. This will be discussed in more detail in section (4.3).

4.2.3 Designing the Recorders: Step 2

This subsection will describe the extrusion process step in drawing the recorders in AutoCAD 2015. Extrusion is the process in which a 2D object is extended in a third dimension in order to create a 3D object. Once the cross-sections using LINE or PLINE have been drawn (from the first step), the second step is to extrude them into a 3-dimensional object. Calling the EXTRUDE command, selecting all three cross-sections, and giving the extrusion parameter of 10 mm will produce the object in figure (4.11 - 4.12).

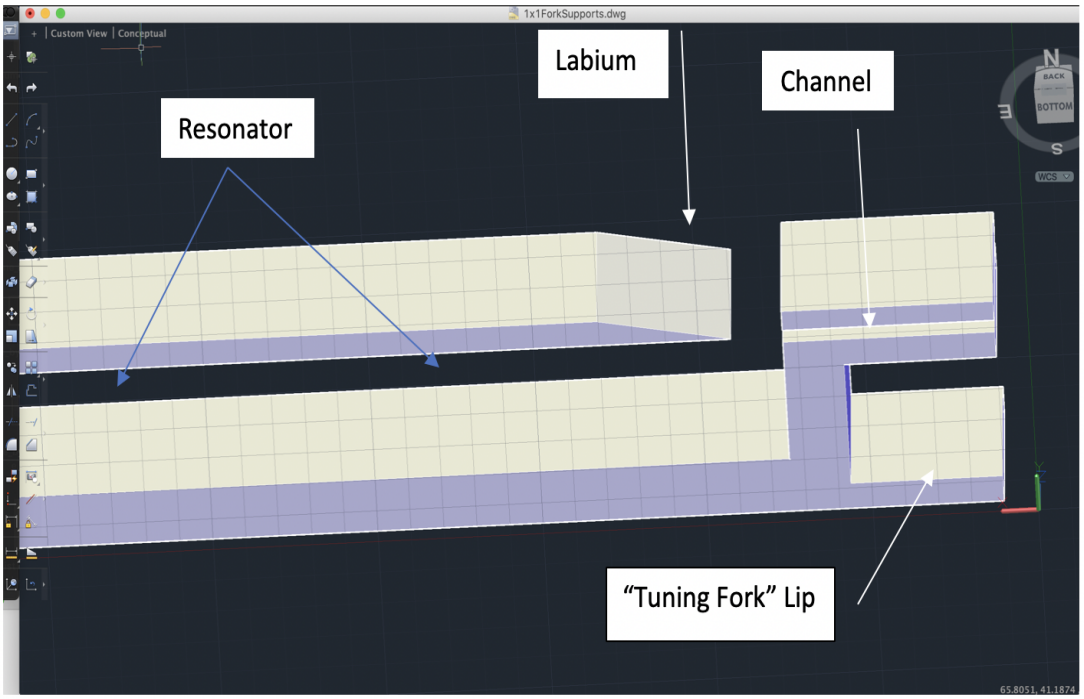

Figure 4.12: A visual of what the extruded cross-sections look like in AutoCAD after step 2 is performed.

4.2.4 Fabricating the Recorders: Step 3

Once step 2 has been completed, it is time to add supports that hold the labium in place during the printing process. This step is crucial in order for warping effects to be minimized and can easily be justified. The 3D printer lays the plastic down in layers in order to make an object, in our case a recorder. When it is first deposited, the plastic is typically at 215 °C and in a gel-like phase. The first several layers of the labium can warp in the middle under their own weight if there is nothing to support the weight. By painful experience we found that warping produces unusable recorders. One will typically use PLANESURF and EXTRUDE to draw the supports that extend from the channel to the cusp of the labium as can be seen in figure (4.13 - 4.14). Note that the supports in figures (4.13 - 4.14) will be removed from the recorder once it has been fabricated. The supports were removed from the recorder by (1) cutting the supports at the channel end using a small-sized pair of wire cutters, (2) make a small incision in the supports at the labium end and finally (3) using a set of pliers to gently pull the supports off the labium.

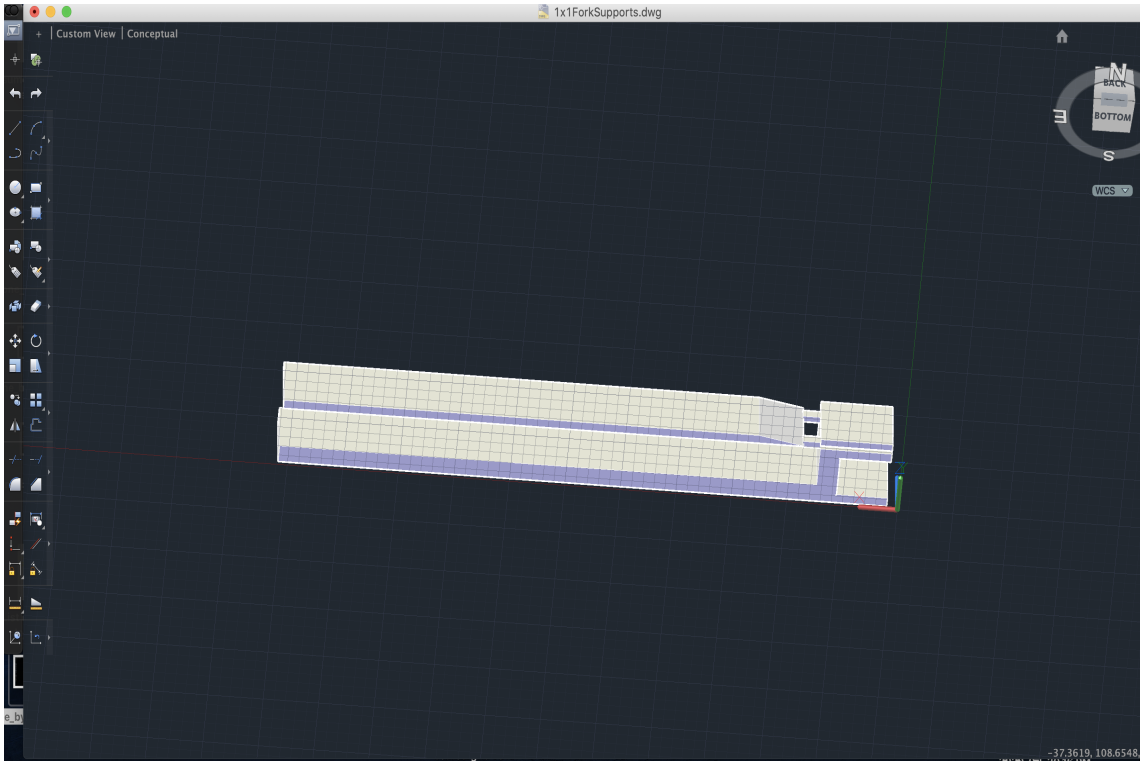

Figure 4.13: A visual of what the addition of the supports looks like in AutoCAD after step 3 is performed.

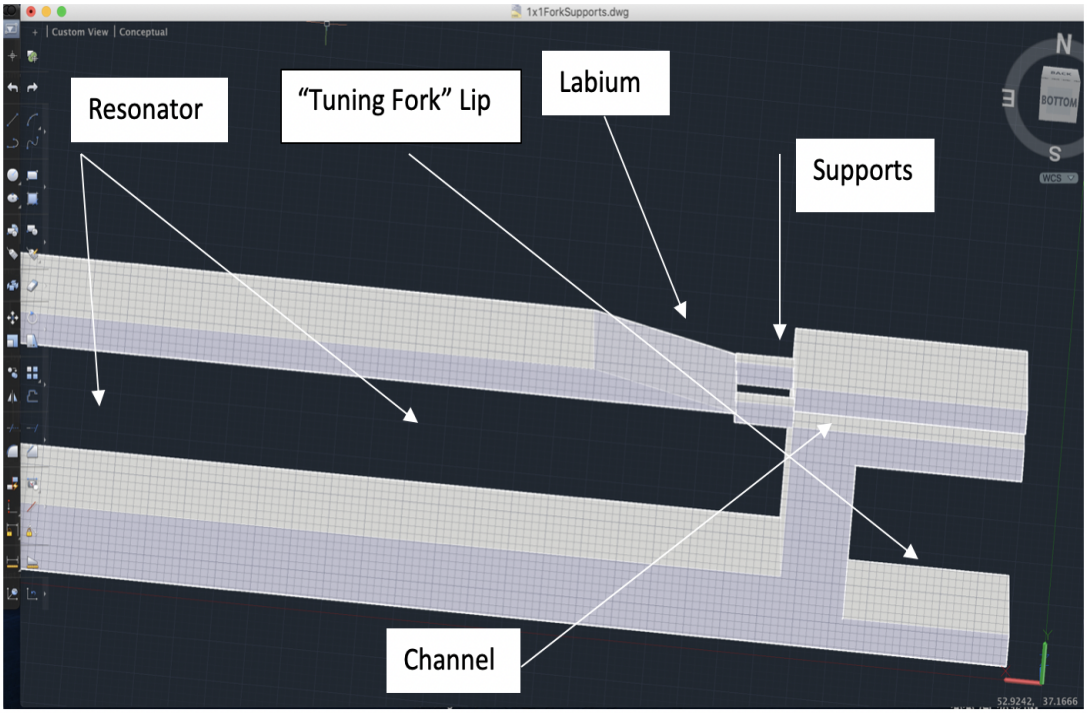

Figure 4.14: A zoomed in visual of what the addition of the supports looks like in AutoCAD after step 3 is performed.

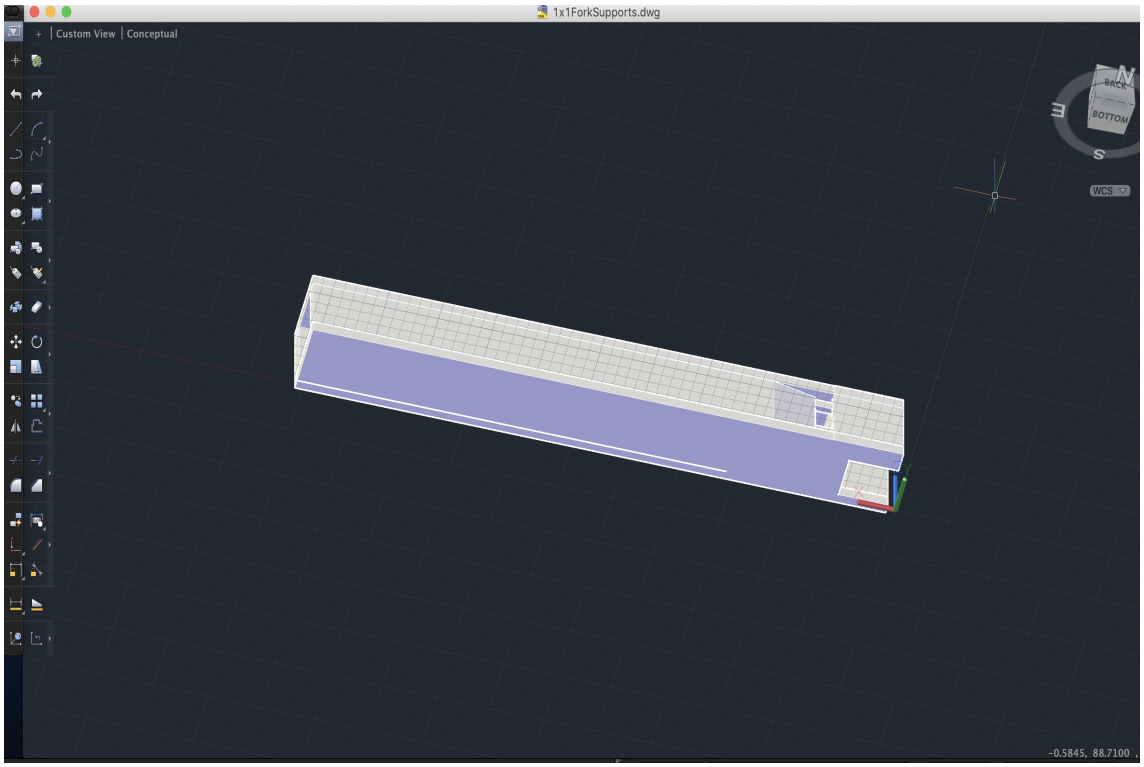

Figure 4.15: A visual of what the finished modeled recorder looks like in AutoCAD after step 4 is performed.

4.2.5 Designing Recorders: Step 4

This subsection will describe the fourth and final step in designing the recorders in AutoCAD 2015. The last and final step is to draw the walls that will enclose the resonator and channel of the recorder. This can again be done using the PLANESURF and EXTRUDE command. First two planes (using PLANESURF) should be drawn on the sides of the recorder to enclose the resonator and channel. Next, these two surfaces are extruded in order to give some thickness to make these surfaces into walls as seen in figure (4.15 - 4.16).

4.3 Overview of 3D Printing

This section will focus on the 3D printing aspect of the fabrication process as opposed to the previous section which focused on designing the recorders in a computer-aided design (CAD) software. This section will be divided into multiple subsections the first of which will focus on the two different types of 3D printers that were considered when conducting this

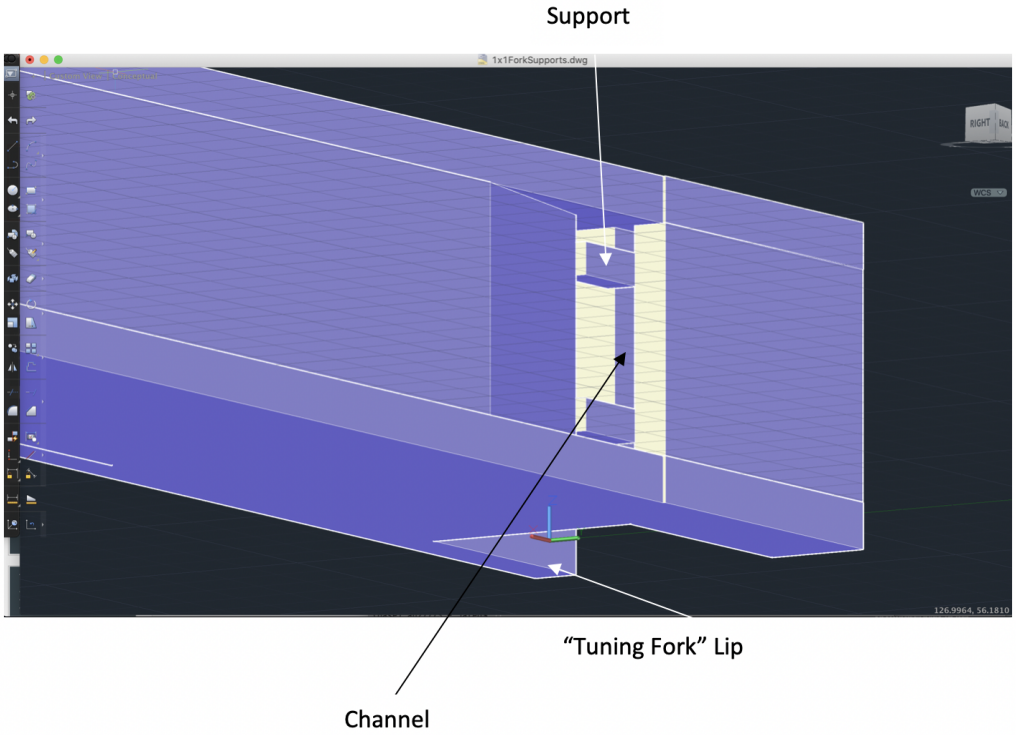

Figure 4.16: A zoomed in visual of what the finished modeled recorder looks like in AutoCAD after step 4 is performed. Take special note that, in this figure, the recorder has been flipped on its side so the labium, channel, supports and tuning fork can be viewed.

research project and their corresponding pros and cons. The second subsection will focus on the parameters that were selected on the 3D printer that was chosen to fabricate the recorders (a MakerBot replicator+). The third subsection will focus on the (subtle) importance of printing orientation and the *exact* physical orientation to use in order to produce recorders that are consistently usable. The fourth and final subsection will be brief and show pictures of the final recorders that were used in the experiments (to be discussed in chapter 5 section 1).

4.3.1 3D Printers

There are two types of 3D printers that were considered to fabricate the recorders in this research project: digital light processing (DLP) printers and fused deposition modeling (FDM) printers. DLP printers work by drawing the image of each layer of the object, in our case a recorder, onto a liquid thermoset resin. Thermosetting is the process of hardening a polymer, resin, or plastic by curing; DLP printers use light to cure the liquid layers of resin. DLP printers produce highly detailed and smooth objects. The second type of printer that was considered in this project, FDM printers, function by extruding a molten plastic filament layer-by-layer onto the building surface of the printer. FDM printers are best used to produce quick instruments/objects, but the finished products can have relatively rough surfaces and can lack strength.

The DLP printer (a Tiger XHD printer made by *Romanoff, Amityville, NY* pictured in figure 4.17) from the 3D printing lab at the College of Math and Science (COSAM) at Auburn University was strongly considered for fabrication purposes. Because the Tiger printer is a DLP printer, it would be able to produce a very detailed instrument with low uncertainty in important dimensions (channel height, window). However, the recorders from section (4.1.1) and (4.1.2) are too large for what the Tiger printer was able to to fabricate as one piece and there were significant issues during the curing process. The most frequent issue was that the resonator would warp so severely that the instrument would appear to be bent. We attempted to fabricate the recorders as two distinct pieces, i.e, a mouthpiece and a resonator piece but there were still warping effects in the channel that were hard to mitigate. In addition, the resonator of the (two piece) instrument would frequently fall off the build plate due to its weight. The

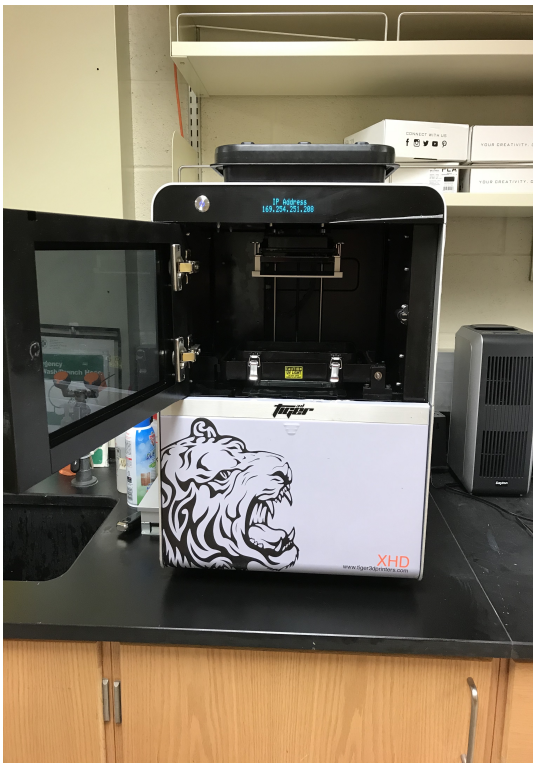

Figure 4.17: A picture of the Tiger printer XHD made by *Romanoff* with its door open revealing the build plate and resin reservoir.

Tiger Printer was therefore *not* selected for producing the recorders used for the experiments in this thesis.

The FDM printer (a MakerBot Replicator+) in the printing lab at COSAM was the machine that was ultimately selected to print the recorders that were used for our experiments. The downside to the FDM printer is the decrease in layer resolution and that there was some surface roughness surface of the recorders. The upside to the MakerBot is that print times are *significantly* reduced compared to the Tiger printer. The Makerbot printer could also easily print the recorders as *one* piece guaranteeing continuity in the resonator. There were issues that were (painfully) solved yielding the recorders that are given at the end of this chapter. Information that go into the setting and print orientation can be found in the next subsection (section 4.3).

4.4 3D Printing Side Effects, Microscopy and Uncertainty

In section (4.3.1) two kinds of 3D printers were considered to make the recorders that were used for experimental purposes in chapter (5). Section (4.3.1) also described the benefits and

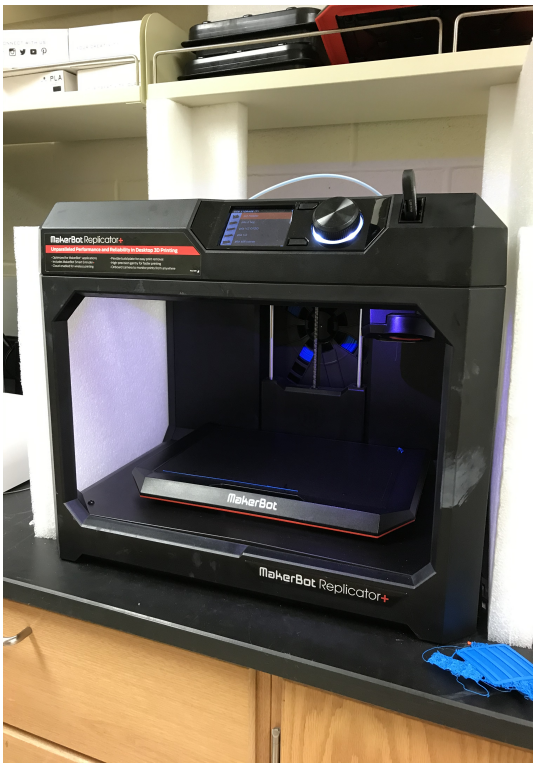

Figure 4.18: A picture of the MakerBot Replicator+ that was used in this research project.

cons of these different types/models of each 3D printer. One of the parameters that drew sharp attention is the printing resolution of the 3D printer that is being considered. The printing resolution of a 3D printer is determined largely by the thickness of each layer that is deposited on the build plate of the 3D printer. A high print resolution means that the deposited layers are thin and will yield very detailed and smooth fabrications. A region of the recorder that is particularly important is the channel of the recorder (see fig. 3.3); this is where a blowing speed u is imposed (the initial condition is set here) that will propagate and determine the dynamics of the gas at all other points in and around the recorder. In addition, the dimensions of the channel are small (the channel height is only 1 mm) and therefore a relatively small uncertainty in the dimensions of the channel will have a larger effect inside the channel of the recorder.

In chapter 5, the results of the simulations and experiments with the 3D printed recorders will be compared in order to validate the simulations. In addition, one other reason is to quantify the uncertainty in the measurement of the blowing speed in the channel of the recorder that results from the (relatively low) printing resolution. The quantity u in equation 5.2 is the blowing speed in the channel of the recorder; u is dependent on the *square* of d, namely, the

channel height. This means that only a 5% difference in the channel heights of two recorders, with the same dimensions in the AutoCAD drawing, can cause a 10% difference in the blowing speeds in the channel. Therefore, it is important to have an estimate of the value and uniformity of the channel height using direct examination after fabrication was complete. There were two primary methods that were used to accomplish this that yielded similar results: optical microscopy and the use of feeler gauge of the kind used to measure narrow gap spacing, e.g., a spark plug found in an old model automobile. This section will briefly describe the optical microscopy method, image analysis and results from the image anlaysis.

Thanks to the help of Dr. Chris Easley, optical microscopy was used to directly observe the channel cross section which had much better resolution than what could be obtained with the feeler gauge. A microscope was used to take images of the channel of the recorder from the perspective of the $y - z$ plane (see fig. 4.19). An example of such an image is given in figure (4.19). The open-source image analysis software, *Image J*, was used to analyze the images. The general procedure for the analysis will be described here. First an image with known dimensions was used to calibrate our measuring scale in the *ImageJ* environment. Afterwards we can then measure the channel heights in *ImageJ*. The analysis had the following basic steps:

1. Load channel images into *Image J*.
2. Calibrate the scale within *ImageJ*.
3. Measure multiple heights along the channel in the lateral direction including the corners of the channel to account for rounding.
4. Average the heights and compute their standard deviations.

Following this procedure we calculated the channel heights to within ± 0.05 mm. In the analysis that follows in chapter (5), we use the uncertainties from the optical microscopy method which were calculated to be ± 0.05 mm. Lastly, there is rounding present in the corners of the channel of the recorder (see fig. 4.19). This rounding was accounted for in estimating an average value of the channel height, having only a 2% effect on the final estimate of the channel height. The final estimate can be written $1.00 \pm 0.05 \pm 0.02$.

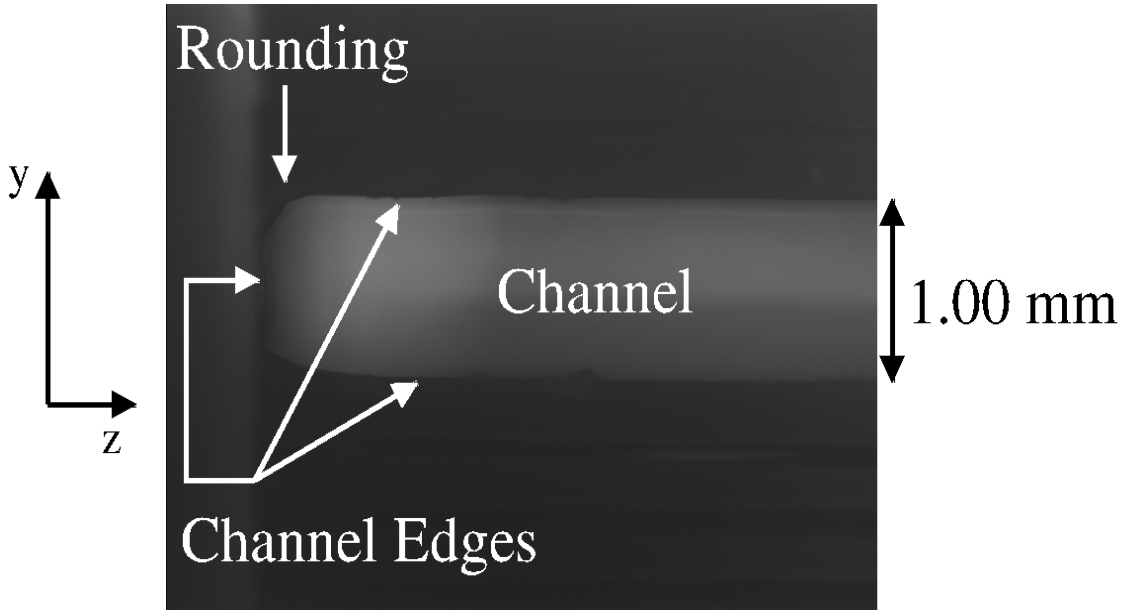

Figure 4.19: Example of an image taken with a microscope that was used to measure the channel height along y and for the uncertainty analysis in chapter (4.3.1). Note the rounding at the corners on the left side of the channel.

Chapter 5

Experimental Setup, Results and Comparison

5.1 Introduction

It is known among recorder players that playing loud or even maintaining lower notes on lower compassed recorders, such as the bass recorder, is difficult because the instrument tends to easily transition to higher notes at modest blowing speeds. Chapter 3 includes a discussion on the variance of the normalized diameter among the recorder family. For example, the bass recorder, a lower compassed recorder, has a smaller normalized diameter when compared with the sopranino recorder, a higher compassed instrument [27].

In chapter 3, the Navier-Stokes equations were numerically solved to simulate the behavior of a recorder that is being played by a human player. These results were used to study regime change in the bass and sopranino recorders. Additionally, in chapter 3, regime change at lower blowing speeds were linked to smaller normalized diameters (tube diameter/wavelength) when compared to recorders that have larger normalized diameters. This relationship was shown by simulating the air-flow in two different toy-model recorders (sopranino - style/bass - style): one recorder with a larger normalized diameter than the other. The spectral content of the tones produced of each recorder was then analyzed. The recorder with the smaller normalized diameter had its acoustic spectrums dominated by higher-frequency harmonics at significantly lower blowing speeds than the recorder with a larger normalized diameter.

In addition to verifying the regime change behavior observed in the simulations, in chapter 3, the simulations were also used to study how making small alterations to the geometry of the bass style recorder would increase the dynamical range of the fundamental harmonic. In chapter

4 we described how 3D printing was used to make *real* recorders using the designs studied in the simulations (chapter 3).

In this chapter, experimental results for the 3D printed recorders will be presented and compared with the results from the simulations in chapter 3. There are two primary quantities that will be considered when comparing the simulated and experimental results: 1) the values of the frequencies below and above the regime change threshold (this is a weak but important test) and 2) the blowing speeds for regime change and how they vary according to recorder geometry. The agreement between the experiment and simulations in this chapter will serve not only as validation for future studies that require simulations on the recorder, but also previous and future studies on simulations of wind instruments that employ the NSE.

5.2 Experimental Setup

The basic experimental setup is straightforward and described in figure 5.1. Nitrogen gas from a high-pressure canister flows via a pressure regulator that is connected to a valve. Gas then exits the valve and flows through a pressure sensor that measures the pressure at the inlet to the recorder. The resulting sound is then recorded by a microphone and a personal computer. By adjusting the valve and pressure regulator, the pressure at the inlet of the recorder and hence the blowing speed could be varied and the spectrum was measured at different blowing speeds.

Next, we discuss how the blowing speed inside the channel of the recorder is determined from a measurement from the pressure sensor. We know that the pressure sensor and plastic tubing that connects the recorder to the pressure sensor have approximately the same diameter (20 mm) and both are much larger than the height, d, of the channel (1.0 mm). The pressure measured by the pressure sensor is therefore equal to the pressure drop across the channel. The volumetric flow rate is proportional to d^2 and the channel height is much smaller than the diameters of both the pressure sensor and the plastic tubing. From figures (4.3) - (4.7) the channel has a rectangular cross-section. In addition we know that the volumetric flow rate inside the channel of the recorder is sufficiently small (the Reynolds number is relatively small $\backsim 8000$ [29]), such that the flow inside the channel of the recorder is laminar. Since the channel

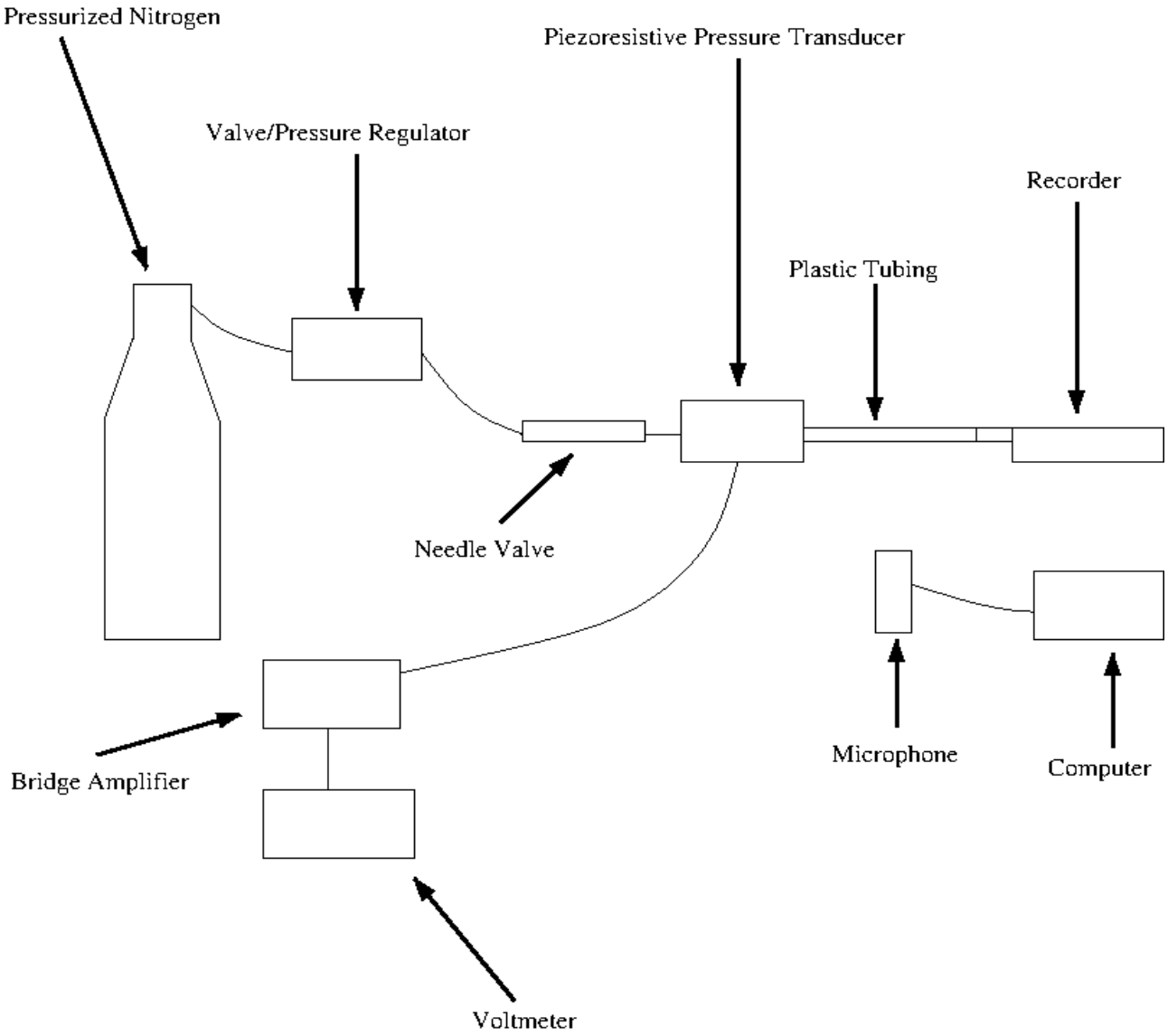

Figure 5.1: A schematic of the experimental setup. The sensor is a piezoresistive pressure transducer and Endevco model: 8510b -1, the computer is a 2017 Apple macbook pro with built in microphone, the bridge amplifier is an Endevco model 126 and the voltmeter used was a Keithley 2100 Multimeter.

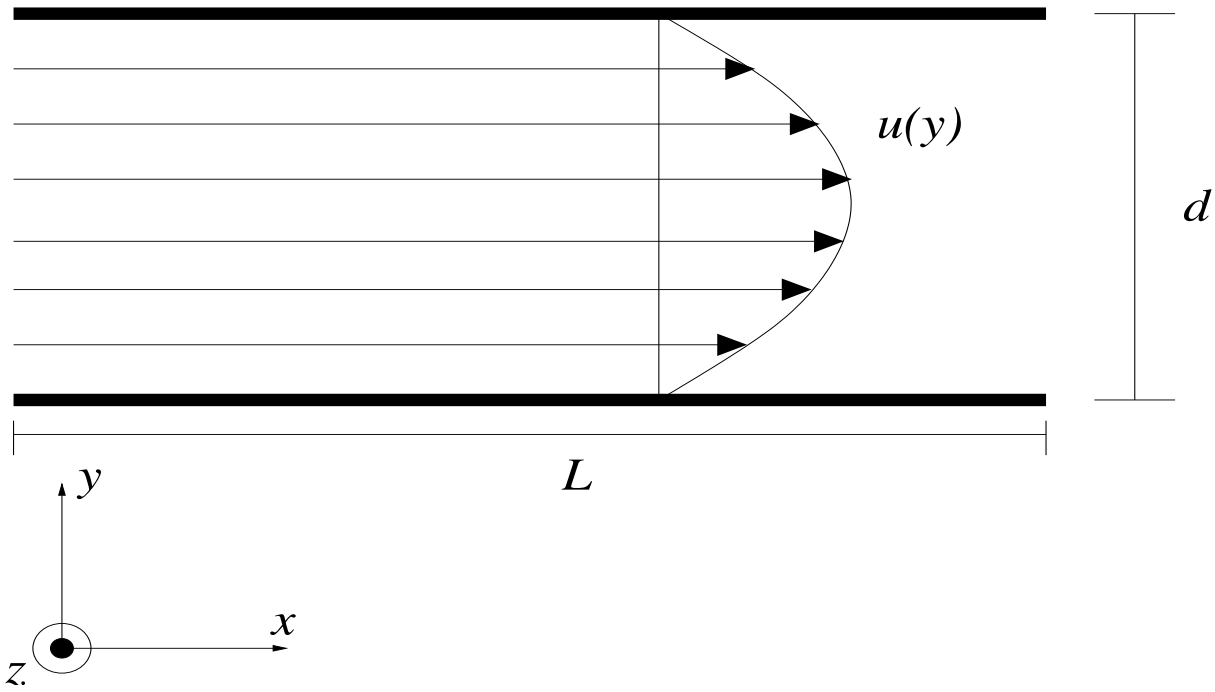

Figure 5.2: Laminar Flow for a rectangular cross-section.

is rectangular we can then say that the flow inside the channel of the recorder is governed by Poiseuille's law for a rectangular cross-section.

Consider a steady, laminar and viscous flow in between two parallel plates. A drawing of this scenario is given in figure (5.2). The flow velocity profile is given by [29],

$$u(y) = \frac{\Delta p y(d-y)}{2\rho L \alpha} \tag{5.1}$$

where Δp is the pressure drop between the ends of the channel, y is the position along the y-axis of the channel, L is the length of the channel, d is the height of the channel, α is the kinematic viscosity, and ρ is the density. The average value of flow velocity in equation (5.1) in the channel is given by equation (5.2),

$$u = \frac{\Delta p d^2}{12\rho L \alpha}. \tag{5.2}$$

Equation (5.2) allows us to calculate the flow speed inside the channel. We can measure Δp using the pressure sensor and the dimensions of the channel – d and L –, the kinematic viscosity

α, and ρ are known. The largest source of uncertainty in the measurement of u is due to d. This is because of the 3D printer's resolution which can be thought of as the amount of detail in which this printer can fabricate recorders. The resolution of our 3D printer is discussed in more detail in chapter 4. We need to determine the height of the channel d independently since we cannot rely solely on the channel height that is in the AutoCAD drawing due to the limited resolution of the 3D printer. Since the value of the channel height is so important we used *two* methods to determine the uncertainty in the measurement of the height of the channel: (1) using a feeler gauge similar to ones used to measure the spacing in spark-plugs in old automobiles and (2) directly observing the channel using optical microscopy. It is convenient and not invasive to use a feeler gauge to estimate channel heights; measurements can be taken anywhere and it is not necessary to alter or damage the instruments in order to obtain such measurements.The convenience of using a feeler gauge comes at the cost of the precision of the measurement and that this method also yields no information regarding the uniformity of the channel height in the z - direction. Optical microscopy to measure d, was discussed in section 4.4. It is worth noting that neither method enabled us to study variation in channel height within the channel.

In chapter 4 the uncertainty in the measurement of the height of the channel as determined by optical microscopy was found to be $1.00 \pm 0.05 \pm 0.02$ mm where the ± 0.02 is the 2% effect that the rounding at the channel corners had on the final estimate of the channel height. The value of d as determined using the feeler gauge (about 1.00 ± 0.07 mm) gave consistent results when compared with the results from the optical microscopy. In the analysis that follows we use the uncertainties as determined by the optical microscopy method of 1 ± 0.05 mm. Given this error of 0.05 mm in the height of the channel (d in equation 5.2), this is about a 5% error in the measurement. Since the flow speed is proportional to the *square* of the channel height, then this equates to an error of approximately 10% in the calculation of the flow speed.

5.3 Results and Theoretical Comparison

In the previous section (section 5.2) the experiment that will be used to obtain the results of the current section (section 5.3) was discussed and a basic schematic of the overall setup was

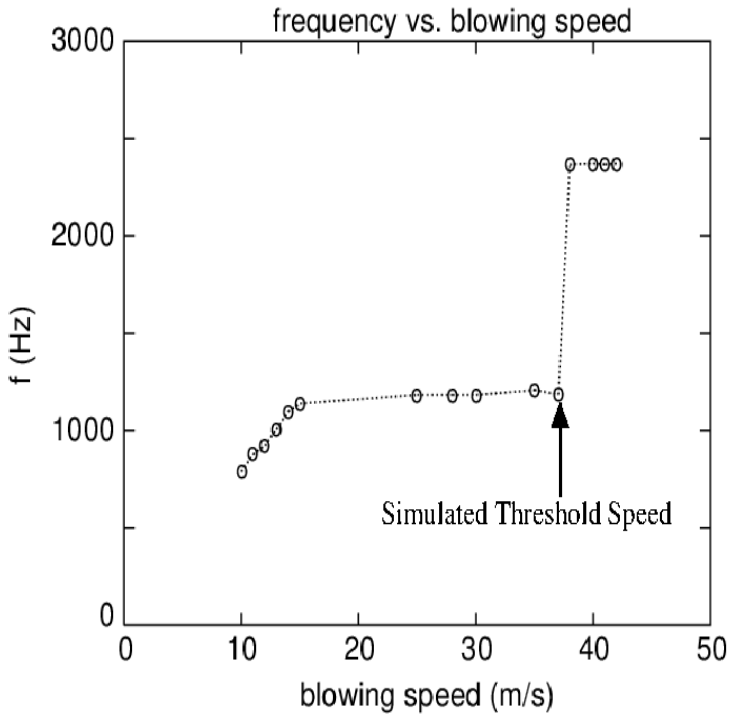

Figure 5.3: The simulated threshold curve for the sopranino style recorder. The arrow represents the location of the threshold blowing speed.

given. In this section, the results of the experiment will be given and compared to the simulation results. In addition there will be a brief discussion of uncertainties.

Firstly, the threshold curves from the simulations are given in figures (5.3 - 5.5). As can be seen the threshold speed for the sopranino recorders is approximately $u_{RC} = 38$ m/s, whilst the threshold speeds for the unmodified and modified bass style recorders are approximately $u_{RC} = 28$ m/s and $u_{RC} = 36.5$ m/s respectively. This shows 1) The sopranino style recorder has a higher threshold speed when compared to the bass style recorder for the lowest harmonic therefore giving a more dynamic range for the lowest harmonic to be played. 2) According to the simulations, the addition of a ”trench” beneath the labium of the bass style recorder raises the threshold speed from $u_{RC} = 28$ m/s $u_{RC} = 36.5$ m/s. This behavior can be revisited in chapter 3.

In this project, six total 3D printed recorders were analyzed: there were two sopranino style recorders, two bass style recorders and two modified bass style recorders. In figures (5.6 - 5.8) the experimental threshold curves are plotted for each 3D printed recorder: sopranino

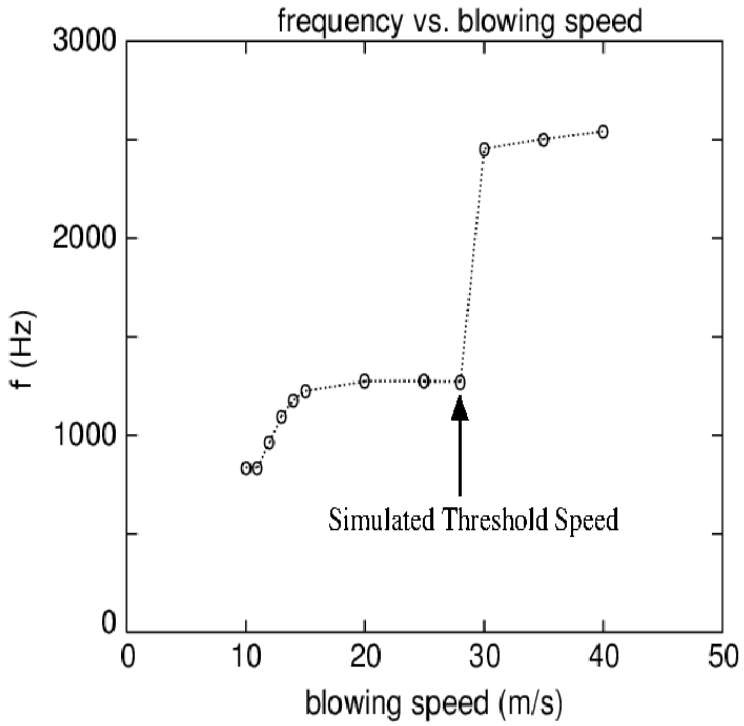

Figure 5.4: The theoretical threshold curve for the unmodified bass style recorder. The arrow represents the location of the threshold blowing speed.

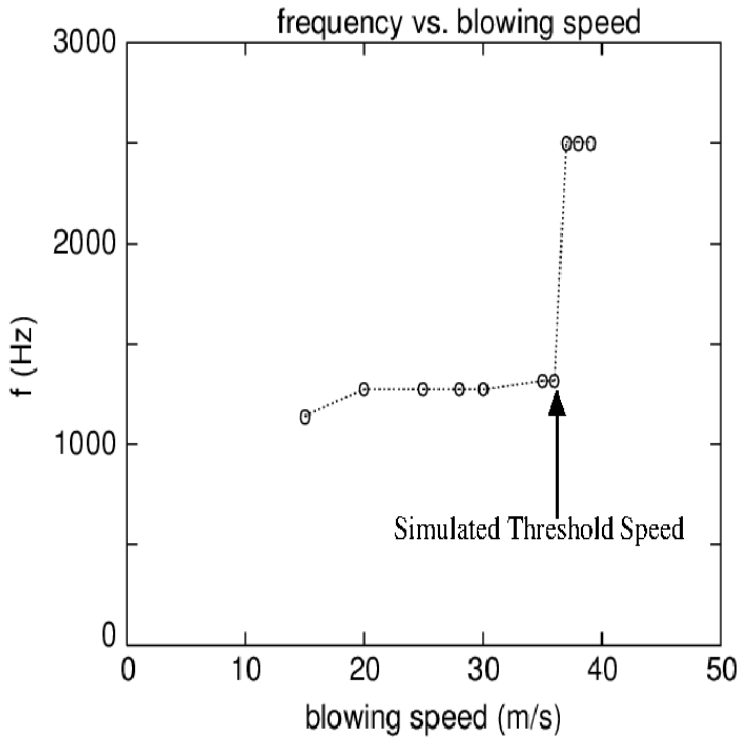

Figure 5.5: The theoretical threshold curve for the modified bass style recorder. The arrow represents the location of the threshold blowing speed.

style, bass style and modified bass style recorder. As can be seen from figures 5.6 - 5.8 the threshold speed for the 3D printed sopranino style recorder is approximately $u_{RC} = 41$ m/s, while for the modified and unmodified bass style and modified bass style recorder the threshold speeds are approximately $u_{RC} = 27$ m/s and $u_{RC} = 41$ m/s respectively.

One representative error bar is given in each of the figures (5.6 - 5.8). The uncertainty in the channel height of the recorder is estimated (section 5.2) to be 0.05 mm. The equation for the average flow speed in the channel of the recorder, which was given in section equation (5.2), is,

$$u = \frac{\Delta p d^2}{12 \rho L \alpha}, \tag{5.3}$$

where Δp is the pressure difference between the two ends of the recorder channel, d is the (separation) height of the channel, α is the kinematic viscosity of air, ρ is the density, and L is the length of the channel. It was briefly mentioned in section (5.2), but to reiterate, Δp is the measured quantity and u is calculated from Δp. The channel height in the AutoCAD drawing (and in the simulation) is 1.0 mm and if we add the 0.05 mm uncertainty in the channel height, then that equates to approximately 10% uncertainty in the channel speed. Therefore, each error bar is centered at each respective speed measurement and has a margin of error $\pm 10\%$. As the blowing speed is increased the error bars get wider implying more absolute uncertainty (but same percentage) in the blowing speed measurements.

Thus far we have primarily discussed blowing speeds and regime change threshold speeds with no discussion of the resonant frequencies below and above threshold. Here we will discuss the values only for f_1, but the discussion and results are similar for f_2. In figure 5.9 we see that the frequenicy of the first (f_1) harmonic for the bass-style and modified bass-style recorders is about the same (both $\approx$ 1180 Hz for f_1). *However*, the harmonics for the sorpanino-style recorder are slightly lower in frequency ($\approx$ 1140 Hz for f_1). This is because the resonator cross-section for the sopranino-style recorder is larger resulting in smaller end corrections [5]. The differences found in f_1 and f_2 between the bass style recorders and the sopranino style recorder in the simulations are also found in the experiments to the same order of magnitude.

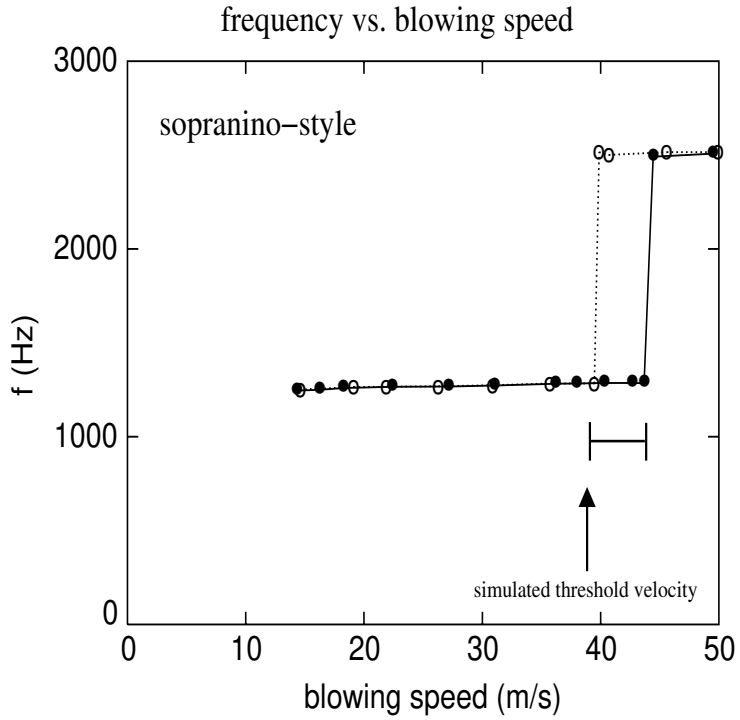

Figure 5.6: Both of the experimental threshold curves from the sopranino style recorders that are to be compared against the simulated l threshold plots. The error bar is centered at $u_0 = 43$m/s and has a margin of error of $\pm$ 10%.

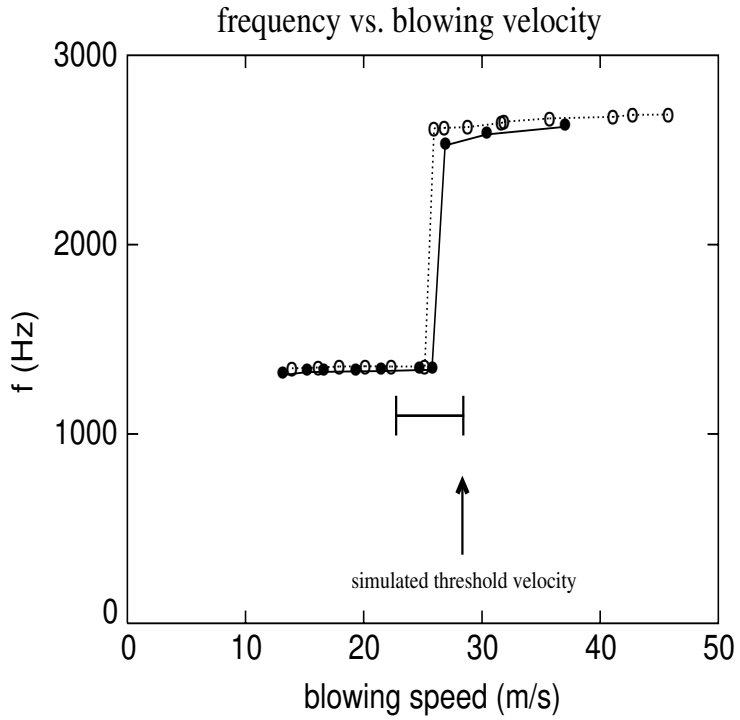

Figure 5.7: Both of the experimental threshold curves from the unmodified bass style recorders that are to be compared against the simulated threshold plots. The error bar is centered at $u_0 = 27$m/s and has a margin of error of $\pm 10\%$.

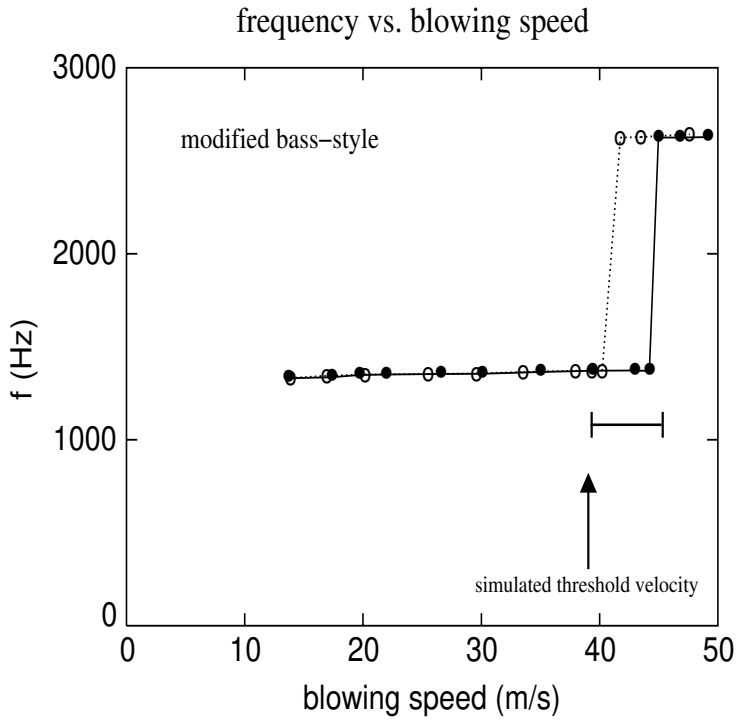

Figure 5.8: Both of the experimental threshold curves from the modified bass style recorders that are to be compared against the simulated threshold plots. The error bar is centered at $u_0 = 41$m/s and has a margin of error $\pm 10\%$.

The fundamental frequency for the 3D printed sopranino style recorder is $f_1 \approx 1267$ Hz while the fundamental frequency for the both bass style variants is ≈ 1330 Hz. At this time it is not clear why there is this difference in frequency (both f_1 and f_2) between the experiment and simulations, but it could be the subject of future study.

In figures (5.10 - 5.12), the respective theoretical and experimental threshold curves are plotted in the same figure for easy comparisons. From the 10% error bar, we can conclude that experimental and theoretical results are in agreement. In addition, we can see that the experimental threshold speed (approximately $[26 - 27]$m/s) for the unmodified bass style recorder has significantly been increased to around ($[36 - 37]$m/s) which is a proof of concept that the geometry alterations to the bass style recorder do indeed resolve the regime change issue that is present in the bass style recorder. Together, figures (5.6 - 5.12) conclusively show that the threshold speed for the bass style recorder has been significantly raised from a value of approximately $u_0 = 28$m/s to about $u_0 = 36.5$m/s with the addition of a trench added beneath the labium of the bass style recorder. This was behavior that was accurately predicted by simulations that were based on the Navier-Stokes equations which are a first principles piece of physics used to described fluid motion. The uncertainty in the channel height which was predicted to be 0.05 mm might be too conservative of an estimate, so experimental and theoretical agreement might be more accurate than presented here. However, the desired behavior of increasing the threshold speed of the bass style recorder has certainly been predicted by the simulations and empirically confirmed using the experiment described in section (5.2).

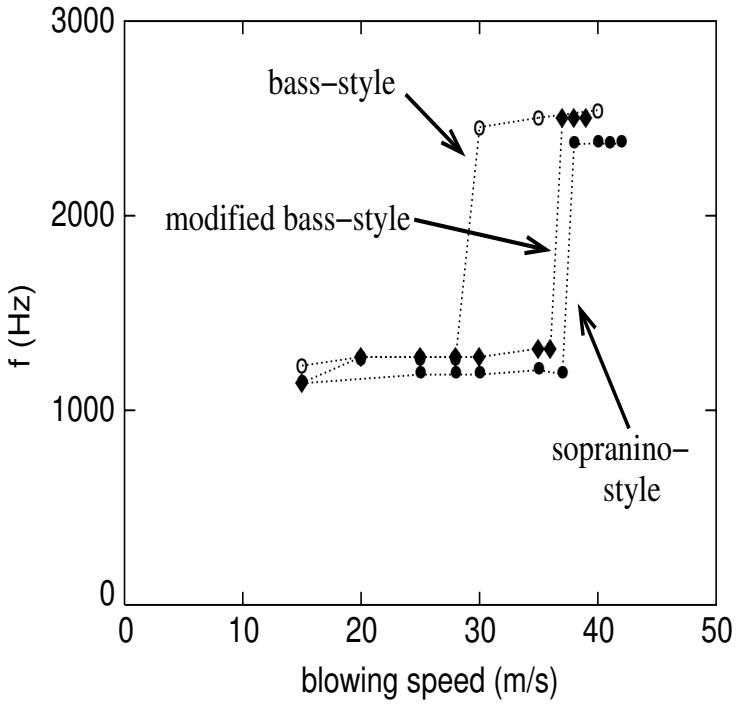

Figure 5.9: The simulated threshold curves for the sopranino-, bass-, and modified bass-style recorders.

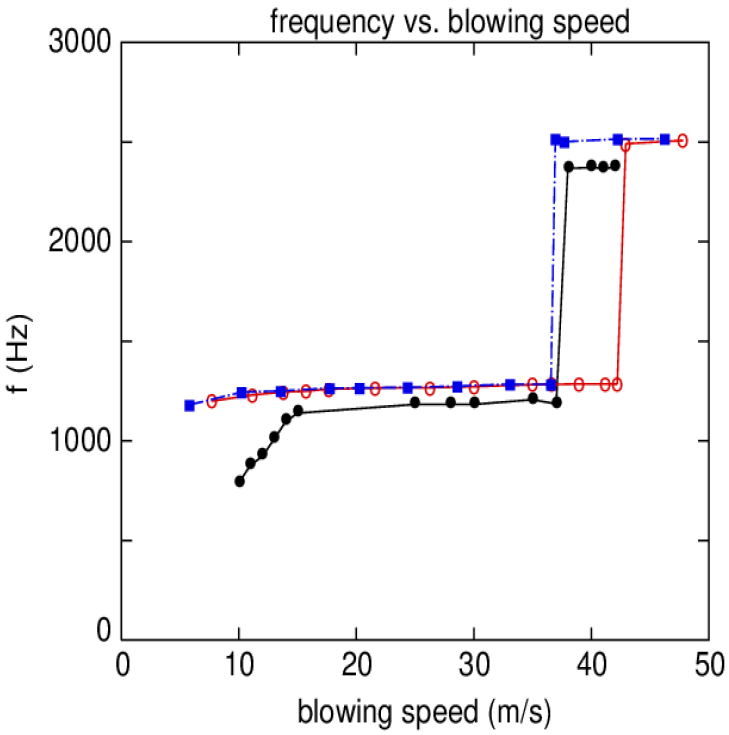

Figure 5.10: The experimental and theoretical threshold curves for the sopranino style recorder. The simulated threshold curve is given by the black line and symbols.

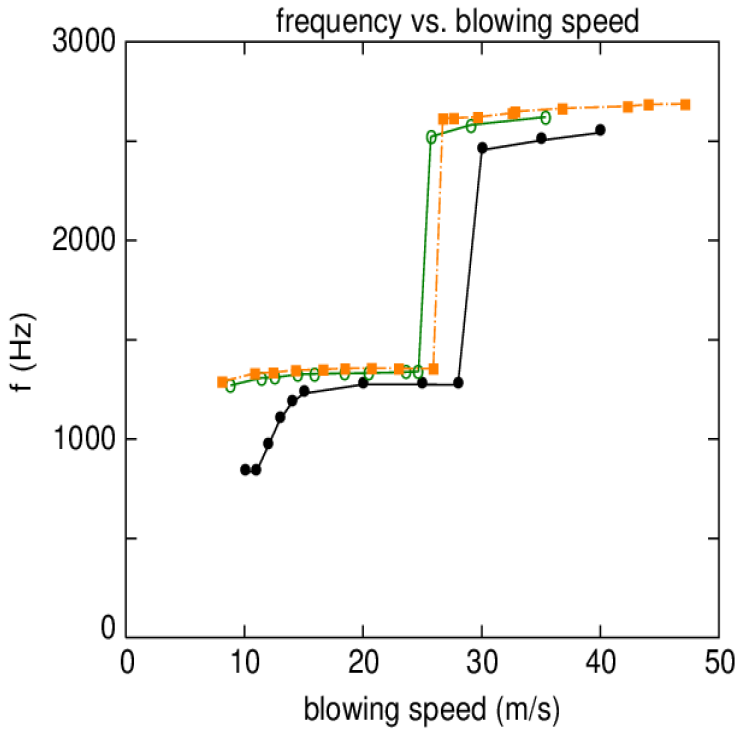

Figure 5.11: The experimental and theoretical curves for the bass style recorder. The simulated threshold curve is given by the black line and symbols.

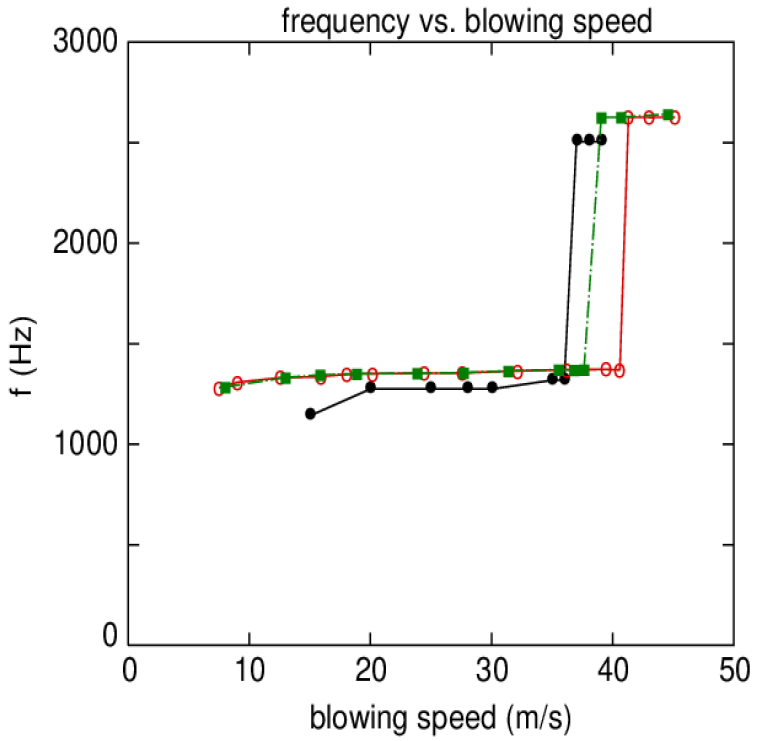

Figure 5.12: The experimental and theoretical curves for the modified bass style recorder. The simulated threshold curve is given by the black line and symbols.

Chapter 6

Effects of Blowing Profile on the Tone of a Soprano Recorder

The purpose of this thesis is to gain a deeper understanding of wind instruments with an emphasis being placed on the recorder. The recorder is an instrument that is introduced to students in their early music education, usually in primary school. One reason for this is because students have little control over the tone color of the instrument; in order to produce a tone with the instrument one only must establish a flow velocity inside the mouthpiece (or channel) and open or close tone-holes as necessary for the desired note. Contrast this with an instrument such as the clarinet where subtle interactions such as those with the player's lips and the reed have important effects on the nature of the tone, i.e a "squawk" or a nice tone, that the instrument produces [30]. Therefore a recorder is a logical starting point for studying the effects that elementary parameters such as blowing speed and ramp-up time have on the attack transient and tone color of a wind instrument since there are fewer parameters that the player can directly control.

Attack transients are known to be important in how people perceive the tone of the instrument [31–35]. One reason for this is that the musician may play a specific note for a very short time interval making the attack transient a significant proportion of that note's played duration. In addition, the attack transients of wind instruments are known to have longer time durations (10 - 30 ms) than for instruments in other families making them especially important in how their tones are perceived by human listeners [31]. In this chapter we will study the effects that *two* parameters have on the spectral content of the attack transients and steady state region of the tone in a recorder. The parameters of interest in this chapter are (1) the blowing speed that the player establishes in the channel of the instrument and (2) the ramp-up time, or how long the

player takes to establish their final blowing speed. We will do so using two methods of spectral analysis: (1) the familiar calculation of the sound spectrum using a FFT and (2) analyzing the autocorrelation function.

In the proceeding sections of this chapter, we will describe the autocorrelation function and explain why it is very useful to combine analyses from the FFT and autocorrelation function (section 6.1), describe the model of recorder we are simulating (section 6.2) and then lastly, analyze the attack transients and steady state portions of the sound produced by a *full-sized* soprano recorder using both the FFTs *and* autocorrelation function (section 6.3) for several different notes (C5, G5, E5 and C6) with different blowing conditions. In section 6.1 we will begin by looking at some spectra and pressure versus time plots for the small scale recorders from chapters 3-5 as an illustration. However, the goal of this chapter is to understand what control a player has over the tone of a *full-sized* soprano recorder. Therefore, the results in section 6.2 and onward are for a model of a *full-sized* recorder.

6.1 Autocorrelation and Correlograms

In this chapter we will use both the sound spectrum as calculated using a Fast Fourier Transform (FFT) *and* a correlogram constructed using the autocorrelation function to analyze recorder tones. In this section we will discuss why *both* methods are needed in order to understand the periodicity of the tone produced by a recorder.

A Fourier transform is a well-known method among physicists to understand the spectral content of a signal. If the entire signal is used to calculate the FFT, then the spectrum that the FFT produces is a summary of all the spectral features present in the signal. It does not give information regarding how the spectral content varies with time - this is the purpose of the spectrogram. One way of constructing a spectrogram is to calculate multiple FFTs using smaller batches of points and producing a spectrum for each batch. The issue with this approach is that as you use fewer points to calculate the Fourier spectra, the inherent resolution of the FFT becomes worse and therefore the estimates of the frequencies determined by the spectra are less precise [36]. Therefore, while the Fourier transform is a valuable tool for understanding

the spectral shape of a periodic signal, the accuracy of the spectrum can suffer if the spectrum is complicated or temporal information is needed.

The autocorrelation function (ACF) is a method used to study the correlations present in a time series [2]. The ACF measures the dependence of a portion of the series at time t with another portion in the series at time s, where $t \neq s$ [2]. Time points in the series that have large autocorrelation at certain time lags indicate large dependence. Using the ACF, we can construct *correlograms* that consist of points that have large autocorrelation as function of time, t. By doing this, we can use correlograms to visualize accurate estimates of the spectral features and how they vary with time. The disadvantage is that correlograms do not yield as much information on the overall spectral shape of the signal as the FFT does. With all of this this in mind, in the next two subsections we illustrate of the advantages and disadvantages of the FFT and how the ACF and correlogram can help complement our spectral analysis.

6.1.1 Spectral Analysis Using FFT

In chapter 3, we saw sound spectra that were calculated from the results of simulations modeling the sopranino-style, bass-style and modified bass-style recorders using different values of the blowing speed. The spectra for different blowing speeds are given in chapter 3 but for convenience, one of these spectra is repeated in figure 6.1. This spectrum was calculated with a 1,024 point (which corresponds to 23.5 ms) Fourier transform from the data contained in the sound pressure versus time plot in figure 6.2. Moreover, the spectrum in figure 6.1 was calculated using the steady-state portion of the tone; the steady-state region of the tone is labeled with *red* in the same pressure versus time plot. If there were a smaller number of points used to calculate the sound spectrum, say 256, then the peaks would be wider but the relative power of the different spectral components would remain the same. An illustration of this is given in figure 6.3; the parameters used are the same except that 256 points were used to calculate the FFT. The largest peak is still centered at $\approx$ 1180 Hz *but* the peak is significantly wider, yielding a less precise estimate of the frequency. One other subtlety to note is that *both* of these sound spectra were calculated during the steady-state region of the tone where the frequencies are well defined. In the attack region of the tone, the region labeled by the blue line in figure

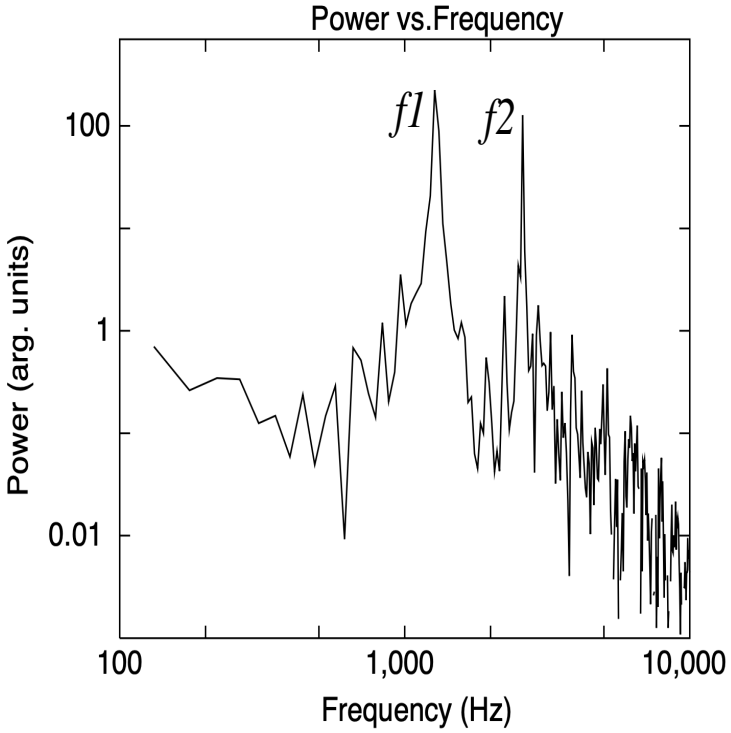

Figure 6.1: Fourier spectrum using 1,024 points for the unmodified bass-style recorder at the regime-change threshold, v_{RC} = 28 m/s. This spectrum was calculated using data from the steady-state (red) region in figure 6.2.

6.2, the spectrum will be more complex. An example of a 1,024 point Fourier transform in the attack (black labeled region) is given in figure 6.4. Using fewer points in the Fourier transform will yield poor quality estimates of the spectral components present in the signal [36]. But if we are dealing with situations when the spectrum is changing rapidly we are forced to use a limited number of data points.

The issues just presented demonstrate the challenges with understanding the spectral features of the attack transient in a recorder - Fourier transform methods always yield less precise estimates of the frequencies when fewer points are used. When trying to understand how the spectral content varies with time, this can be an issue. The *autocorrelation function* can be used to solve this problem in cases like this. In the proceeding subsection, the details of the autocorrelation function are discussed. Afterwards the correlogram, which is used to visualize how the spectral content varies with time, is explained.

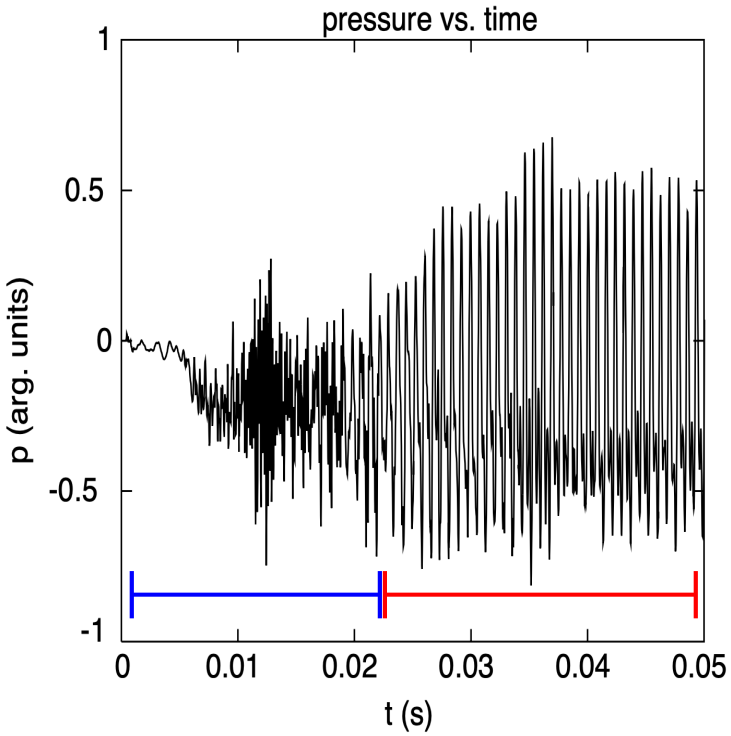

Figure 6.2: Sound pressure vs. time for an unmodified bass-style recorder at the regime-change threshold, v_{RC} = 28 m/s. The blue line indicates the attack portion of the tone and the red line indicates the steady-state portion of the tone.

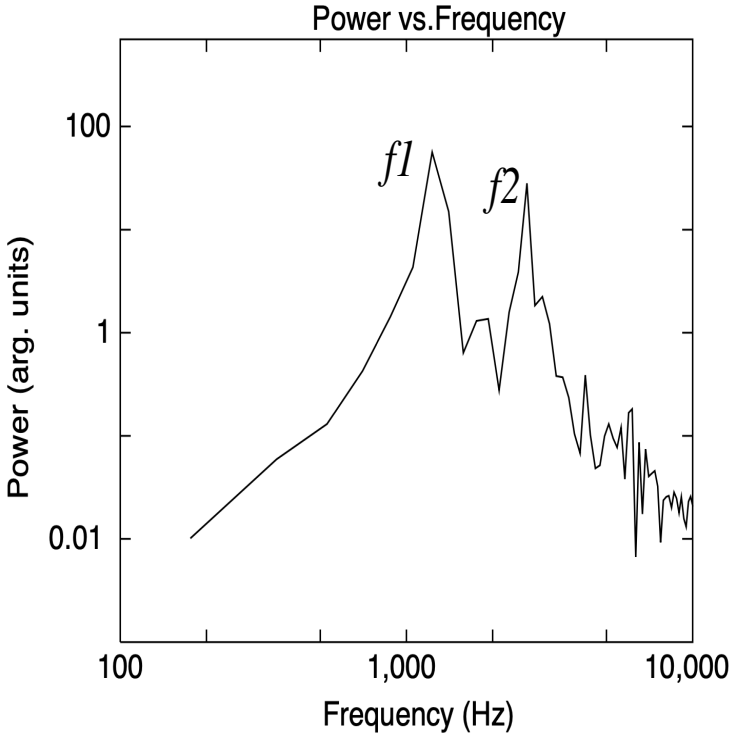

Figure 6.3: Fourier spectrum using 256 points for the unmodified bass-style recorder at the regime-change threshold, v_{RC} = 28 m/s. This spectrum was calculated using data from the steady-state (red) region in figure 6.2.

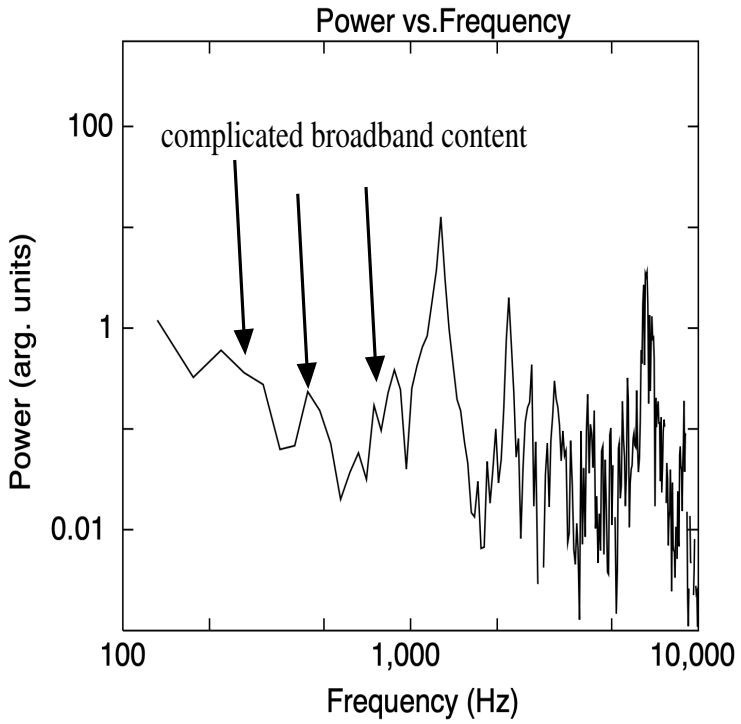

Figure 6.4: Fourier spectrum using 1,024 points for the unmodified bass-style recorder at the regime-change threshold, v_{RC} = 28 m/s. This spectrum was calculated using data from the attack (black) region in figure 6.2.

6.1.2 Autocorrelation and the Correlogram

The advantages and disadvantages of using the FFT for spectral analysis were just discussed. We found that while the FFT is particularly useful for determining the spectral content of a signal, it can lack precision in the estimates of the frequencies when only a subset of the signal is used for its calculation. This can be an issue when one might wish to study how the spectrum varies as a function of time.

The correlogram is a visualization that uses the correlation between two different regions from the same signal of length w, sometimes called the window. In this section we will give a brief overview of the general correlogram as detailed in [2] and in the next subsection an alternative version will be detailed that we will use to analyze the attack transients of several different tones from a simulation of a soprano recorder.

There are several different correlation measures that could be used but the one we will focus on is the *Pearson correlation coefficient*. An expression for the Pearson correlation coefficient is given in equation 6.1,

$$r_{m,n} = \frac{\sum_{k=m}^{m+w-1}(x_k - \overline{x_m})(x_{k+n} - \overline{x_{m+n}})}{\sqrt{\sum_{k=m}^{m+w-1}(x_k - \overline{x_m})^2 \sum_{k=m}^{m+w-1}(x_{k+n} - \overline{x_{m+n}})^2}}, \tag{6.1}$$

where x_k is the kth sample in a time series, m is the starting sample index, n is the delay separating the starting sample points in the window regions, and w is the window width [2]. A good visualization of these parameters for a hypothetical signal can be seen in figure 6.5. In words, $r_{m,n}$ is proportional to the covariance between a portion of a time series and a copy of the time series but delayed by n points in time. The covariance is then divided by the standard deviations of each respective portion of the time series. It can be shown [37] that equation 6.1 is bounded above and below according to $-1 \leq r_{m,n} \leq 1$. If the series has a periodicity time T, then when the time lag n corresponds to the period (T), or a multiple of the period (pT, for $p = 2, 3, 4, ...$), $r_{m,n}$ in equation 6.1 will become large.

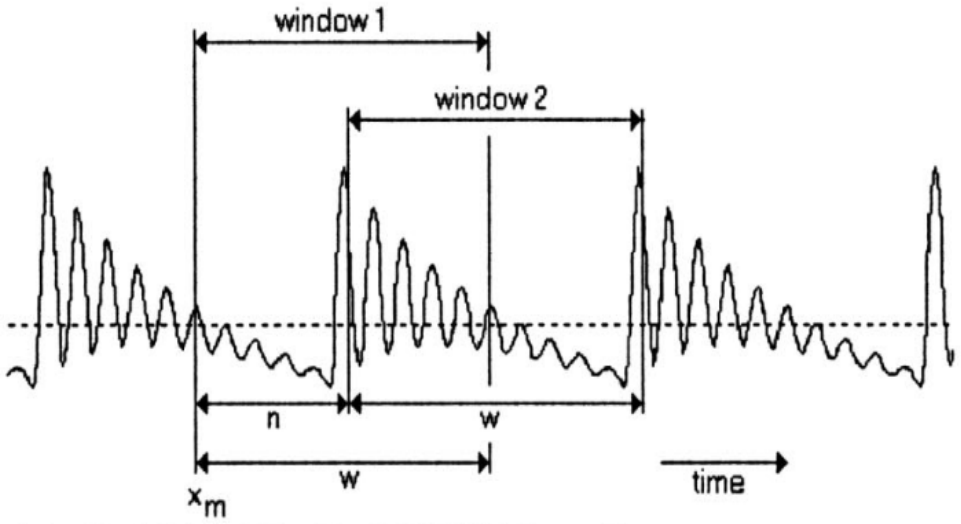

Figure 6.5: Two correlation windows with n and m, x_m, and w labeled. [2].

An example of a traditional correlogram is given in figure 6.6. The correlogram shown as the top plot in figure 6.6 was constructed using the time series (i.e. signal) in figure 6.5. Time, which is indexed by m, is plotted along the x-axis and the time lag, which is indexed by n, is plotted along the y-axis. The darkness of each gray scale point indicates the magnitude of the correlation coefficient for that value of m and n - the larger the correlation, the darker the gray scale value. Such correlograms can be understood as follows: for each time point in the series, the correlation is calculated starting with a time index of m. The correlation is calculated for numerous time lags n, which are plotted along the y-axis. The magnitude of the correlation is calculated for each (m, n) pair and that value determines the darkness. Black points correspond to $r_{m,n} = 1$. If the signal is periodic, then dark bands will be present in the correlogram at integer multiples of the fundamental period ($T, 2T, 3T, 4T, ...$).

I'll briefly interpret the correlogram in figure 6.6 which, again, is constructed from the time series in figure 6.5. We'll begin with the *top* part of the figure which plots the time lag on the y-axis. I will call this type of figure the *time delay-real time* correlogram. For each point, m, on the x-axis in the top correlogram of figure 6.6, $r_{m,n}$ in equation 6.1 is calculated for each value of n on the y-axis. Different values of n correspond to points in the time series separated by Δt ms from the point in the series at m. Dark points in figure 6.6 correspond to $r_{m,n} \approx 1$.

Let T be the fundamental period of the frequency present in the signal. In this *time delay-real time* correlogram, we can see there are multiple dark bands occurring at T (10 ms), $2T$ (20 ms), and $3T$ (30 ms). This means that there are at most three frequencies with values $f_0 = \frac{1}{\Delta t}$, $f_1 = \frac{1}{2\Delta t} = \frac{f_0}{2}$, and $f_1 = \frac{1}{3\Delta t} = \frac{f_0}{3}$ present in the time series in figure 6.5. I use the veribage *at most* because $r_{m,n}$ in equation 6.1 could be ≈ 1 if the time delay (n) is $n \geq T$. In other words, the dark bands in the *top* correlogram could be capturing the same fundamental frequency *if* enough of the signal is provided. High frequency content, spectral content with a small period, is towards the bottom (nearest the x-axis) and low frequency content, spectral content with a large period, is towards the top (farthest away from the x-axis).

I will now interpret the *bottom* part of figure 6.6. This way of displaying the correlogram is useful for our purposes because its y-axis is obtained by inverting the y-axis from the *top* correlogram to show the frequency in Hz. I will call this type of figure the *frequency-real time* correlogram. For each point, m, on the x-axis in the *bottom* correlogram of figure 6.6, $r_{m,n}$ in equation 6.1 is calculated for each value of n on the y-axis. A value of n corresponds to another point in the time series separated by Δt ms from the point in the series at m. *However*, Δt is now inverted which yields $f = \frac{1}{\Delta t}$; f is the quantity that is plotted along the y-axis in the bottom correlogram in figure 6.6. This *frequency-real time* correlogram is especially useful for our purposes because we are able to directly observe the frequencies at which there is strong spectral content within a signal. Let f_0 be the fundamental frequency present in a signal. In this variant of the correlogram, dark bands will appear at f_0, $f_0/2$, $f_0/3$ corresponding to the integer multiples of the fundamental period, etc thus displaying the frequencies of spectral content present in the signal. *However*, $f_0/2$, $f_0/3$ are not necessarily present in the signal; $r_{m,n}$ could be capturing the same fundamental periodicity just at later points in the time series if enough of the signal is provided in equation 6.1. In this frequency-real time correlogram, low frequency spectral content is now towards the bottom of the y-axis while high frequency spectral content is farther up the y-axis.

The frequency-real time correlogram is more appropriate for spectral analysis because of its intuitive method for representing the y-axis - by plotting the frequency along the y-axis rather than time delay (or period). In the next section, we will define a simple variant on this

idea which will be useful for the spectral analysis on the soprano recorder in the remainder of this chapter.

6.1.3 Alternative Correlograms

The full correlogram in figure 6.6 gives us a way of identifying potential harmonic content within the spectrum of a periodic signal as a function of time but it contains too much information for our purposes. A more concise way of displaying the essential same information is to select only the peaks or darkest points in the correlogram. In other words, select the Δt values that correspond to, or where $r_{m,n} \approx 1$, in the time delay-real time correlogram. Afterwards, invert Δt to obtain $f = \frac{1}{\Delta t}$ and plot the corresponding $(m,\ f)$ pair. By following this procedure, we are able to identify possible spectral content present within the signal in a more concise and arguably clearer way. An example of this type of correlogram is in figure 6.7b which was calculated from the sound pressure signal in figure 6.7a. Note that early in the signal there are multiple possible frequencies present which do not seem to be harmonically related to one another. From this point onward, I will refer to the spectral content that is not harmonically related to the resonator of the instrument *inharmonic* content, frequencies, etc. For the remainder of this chapter, frequency-real time correlograms, like the one in figure 6.7b, will be used to understand the spectral content of soprano recorder tones.

6.1.4 Artifact Frequencies

In section 6.1, autocorrelation was explained and then followed by a description of how correlograms are constructed. Correlograms are an important visualization technique which allow us to understand how the periodicity of a signal varies with time. However, a traditional correlogram provides too much information for our purposes in this chapter and therefore in section 6.1.4 an alternative to, but derivative of, the correlogram in figure 6.6 is described. An example of the alternative correlograms we will be analyzing in the remainder of this chapter is in figure 6.7b.

One ‘quirk’ of the autocorrelation function, which was explained in section 6.1, is the presence of what we will term as *artifact* frequencies - frequencies that are present in the

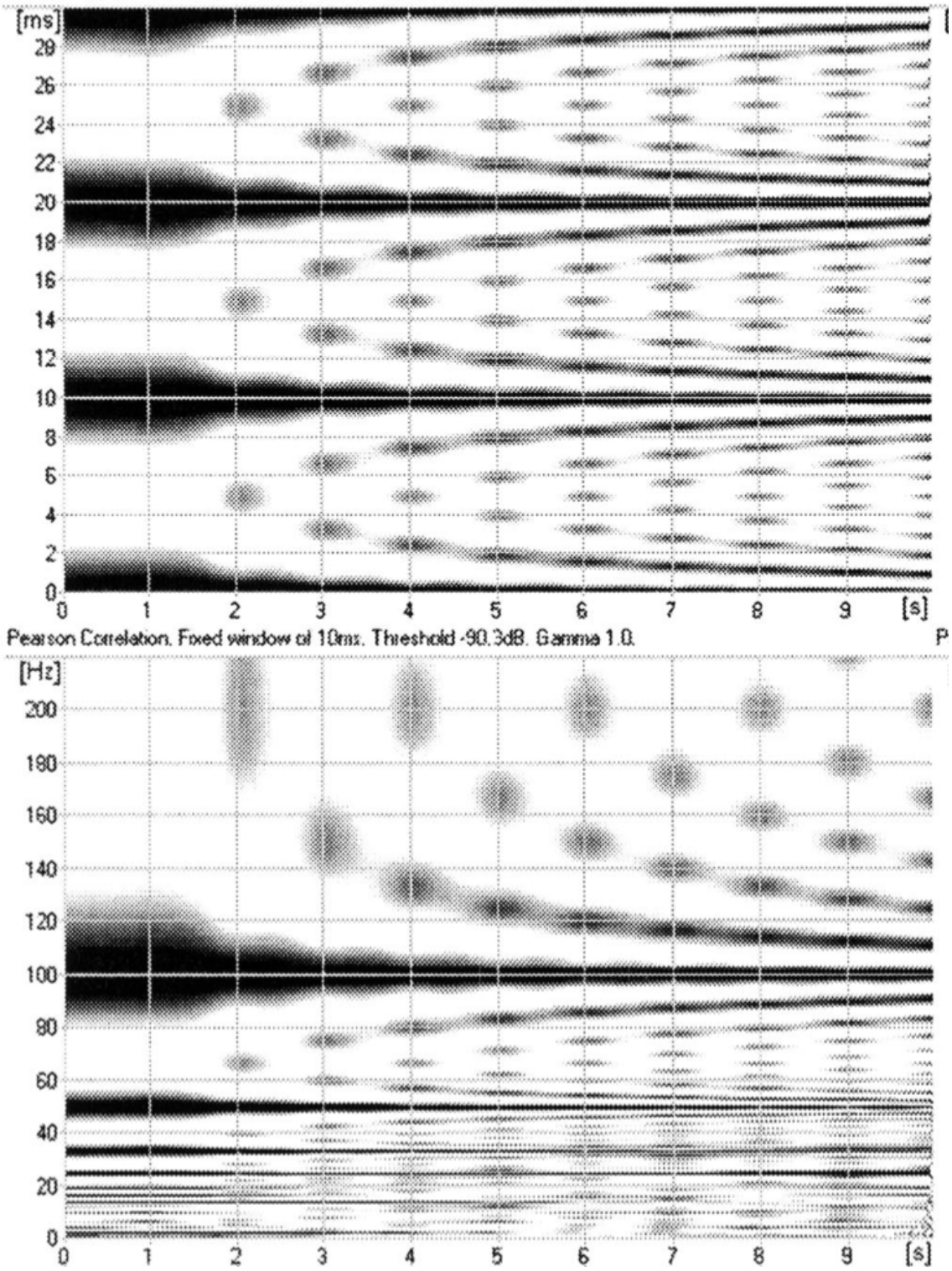

Figure 6.6: **Top**: A *time delay-real time* correlogram. The value of time, or index m, is located along the x-axis and the time lag, or n is on the y-axis. The value of the Pearson correlation is the darkness of the grayscale color. **Bottom**: A *frequency-real time* correlogram with m plotted along the x-axis and $f = \frac{1}{\Delta t}$ along the y-axis. [2].

correlogram but are not true spectral components. An example can be seen if we analyze the correlogram in figure 6.7b and the *green* sound spectrum in figure 6.7c. Each sound spectrum in figure 6.7c was calculated at different points in the signal in figure 6.7a. Specifically, the green sound spectrum was calculated using data from the signal well after 30 ms; later in this chapter, we will give the midpoint of the region where this spectrum was calculated, but for now it suffices to only know that it was calculated after 30 ms. First refer to figure 6.7b. For time greater than 30 ms there seem to be two frequencies present, one frequency at 520 Hz and one at 260 Hz. If we now look at the *green* sound spectrum in figure 6.7c the frequency at 520 Hz is well defined; in fact, the frequency at 520 Hz dominates the sound spectrum. *However*, the frequency at 260 Hz is at best broadband and weak in power. The presence of this spectral component was not anticipated and still being investigated. This artifact is a result of the autocorrelation capturing the same spectral component at 520 Hz but at a time delay that is twice the period associated with 520 Hz. We will call frequencies that are the result of the autocorrelation function capturing spectral content which has already been captured at previous time lags, *artifact frequencies* or *artifacts*.

Frequencies which are artifacts in one region of time in a signal are not necessarily artifacts in another region of time. As a second example, consider again the correlogram in figure 6.7b and the *black* sound spectrum in figure 6.7c. *However*, only consider time that is less than 30 ms in the correlogram in figure 6.7b; the *black* spectrum in figure 6.7c was calculated in this region. There seems to again be *two* frequencies present in the signal during this region of time if we refer to the correlogram. However, if we refer to the black sound spectrum (in figure 6.7c), then it becomes obvious that *both* of the frequencies are present in the sound spectrum during this region of time in the signal.

This example highlights the complementary relationship that these two visualizations have when conducting spectral analysis. The correlogram gives us a good idea how the spectral content of a signal varies in time and the FFT can be used to identify which frequencies are real and which might be artifacts. In the next section we discuss the geometry of the recorder that we will be analyzing.

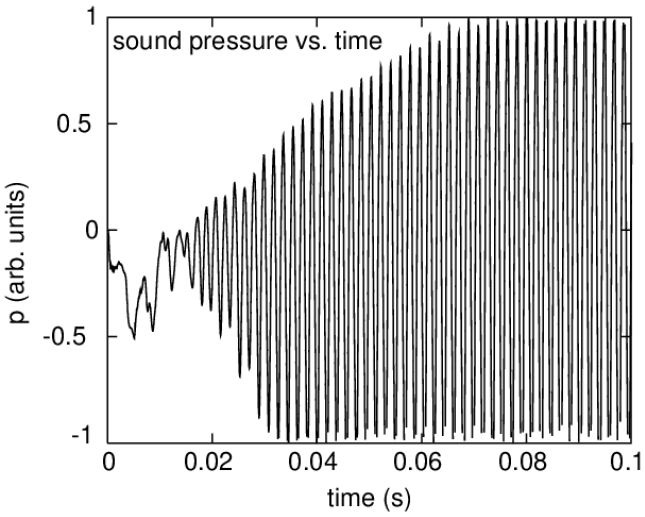

(a)

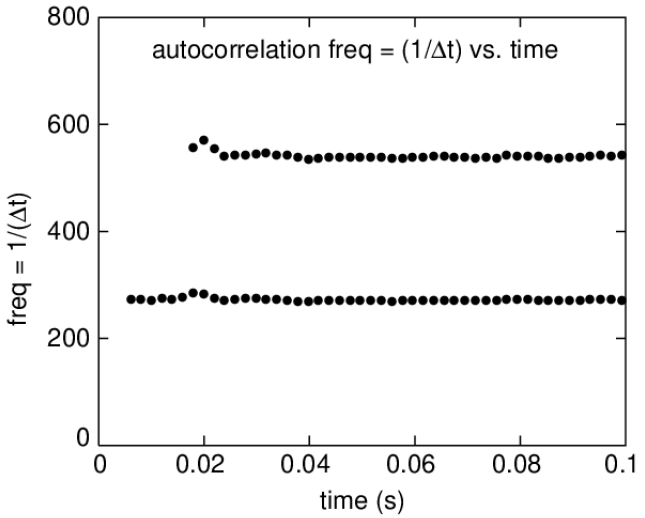

(b)

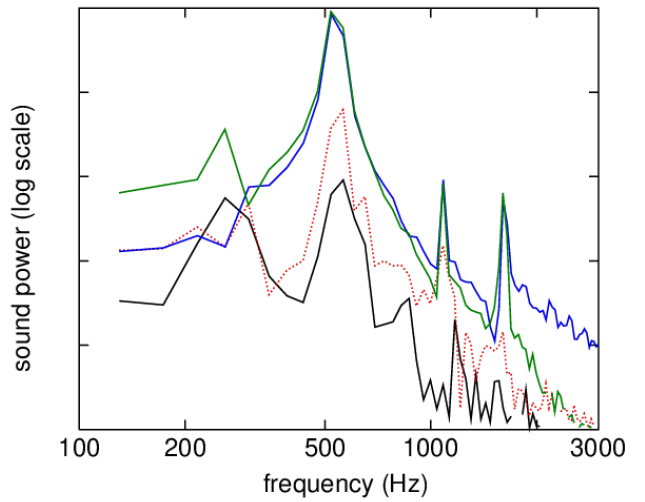

(c)

Figure 6.7: (a) The signal used to construct (a) and (b) in this figure. (b) Alternative correlogram constructed from the data in (a). (c) The sound spectra calculated at various regions in (a).

Figure 6.8: The Yamaha YRS-23 that we are modeling using NSE. This instrument is 33 cm long and has a tapering cylindrical bore. The instrument in this figure has toneholes that are in the same position along the resonator as the simulated instrument in figure 6.9.

6.2 Recorder Geometry Under Analysis

In the past, our group has modeled recorders using geometries that are scaled down in size when compared to real instruments. For example, a soprano recorder is typically $\sim$33 cm long. The recorders we have studied up to this point have been only $\sim$12.1 cm in length. The size of the instruments modeled up to this point have been scaled down because this size was more feasible with the computing resources that were available. With the launch of the more powerful Easley Cluster in 2020, full size instrument simulations became a reality for our group.

For the remainder of this chapter, we will be focusing on simulations that model a full size recorder. Specifically, the recorder we are simulating is a Yamaha YRS-23 soprano recorder which is shown in figure 6.8. The simulated geometry can be viewed in figure 6.9. The model seen in figure 6.9 has a cylindrical bore with a diameter of 13 cm whereas the Yamaha model has the same length but has a tapering cylindrical bore. In addition the toneholes are in the same position along the resonator for both the Yamaha and the simulated instrument. For the results that we will see in the remainder of this chapter, a combination of the toneholes are opened and closed yielding different notes. As we progress through the results of this chapter, it will be stated which note is being analyzed and which of the seven toneholes in figure 6.9 are closed.

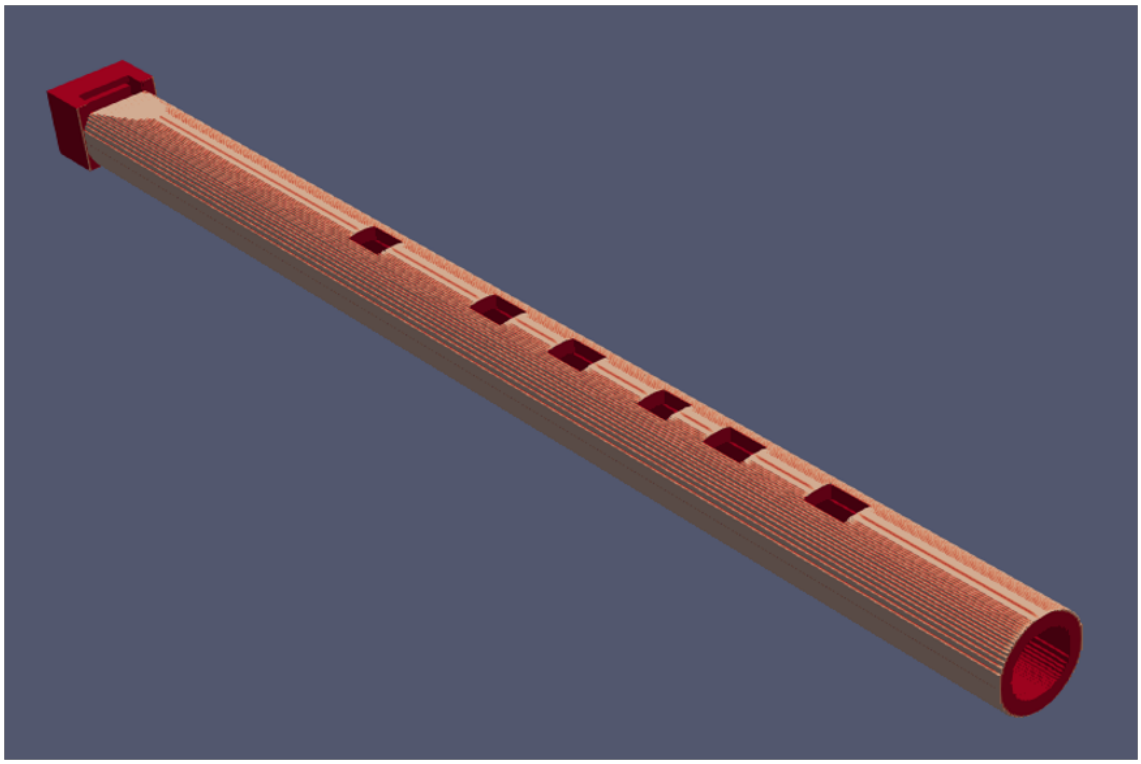

Figure 6.9: The geometry that we are using in the NSE simulations to model the Yamaha YRS-23. This instrument is 33 cm long and has a cylindrical bore that is 13 mm in diameter. This instrument has toneholes that are in the same position along the resonator as the Yamaha recorder in figure 6.8. In this case the open tone holes correspond to a fingering that produces C6.

Summary of Parameters For Spectral Analysis		
Note (Frequency)	Blowing Speed (m/s)	Ramp up Times (ms)
C5 (523 Hz)	12.5, 15	5, 30
E5 (659 Hz)	15	5, 30
G5 (784 Hz)	17	5, 30
C6 (1046 Hz)	21	5, 30

Table 6.1: A list of the fundamental frequencies of each note, the blowing speeds, and ramp up times that will be used in the analysis in this chapter.

6.3 Results

In this section, the spectral analyses are presented for several different notes, blowing speeds, and ramp-up times. For each analysis, the correlogram and sound spectrum calculated with an FFT are presented and analyzed.

The specific notes we will be analyzing are: C5 (523 Hz), E5 (659 Hz), G5 (784 Hz), and a C6 (1046 Hz). We will analyze each of these notes at a fixed blowing speed: (C5, 12.5 m/s and 15 m/s), (E5, 15 m/s), (G5, 17 m/s), (C6, 21 m/s) and specifically, for each of these note-blowing speed pairs we will analyze the FFT and correlogram for two different ramp up times. Each FFT will be calculated with 23.5 ms worth of time and the parameters used to construct each correlogram are given in the appropriate captions. For the C5 we will analyze two different blowing speeds. Different blowing speeds, increasing as we consider higher notes, were used because notes with a higher frequency require higher blowing speeds in order to produce the appropriate fundamental mode. A summary of these parameters are given in table 6.1.

6.3.1 Spectral Analysis: C5

In this subsection we analyze the spectral content of C5 at two different blowing speeds: 12.5 m/s and 15 m/s. Figure 6.10 shows the simulated geometry for the soprano recorder and the tone hole placement necessary to produce C5.

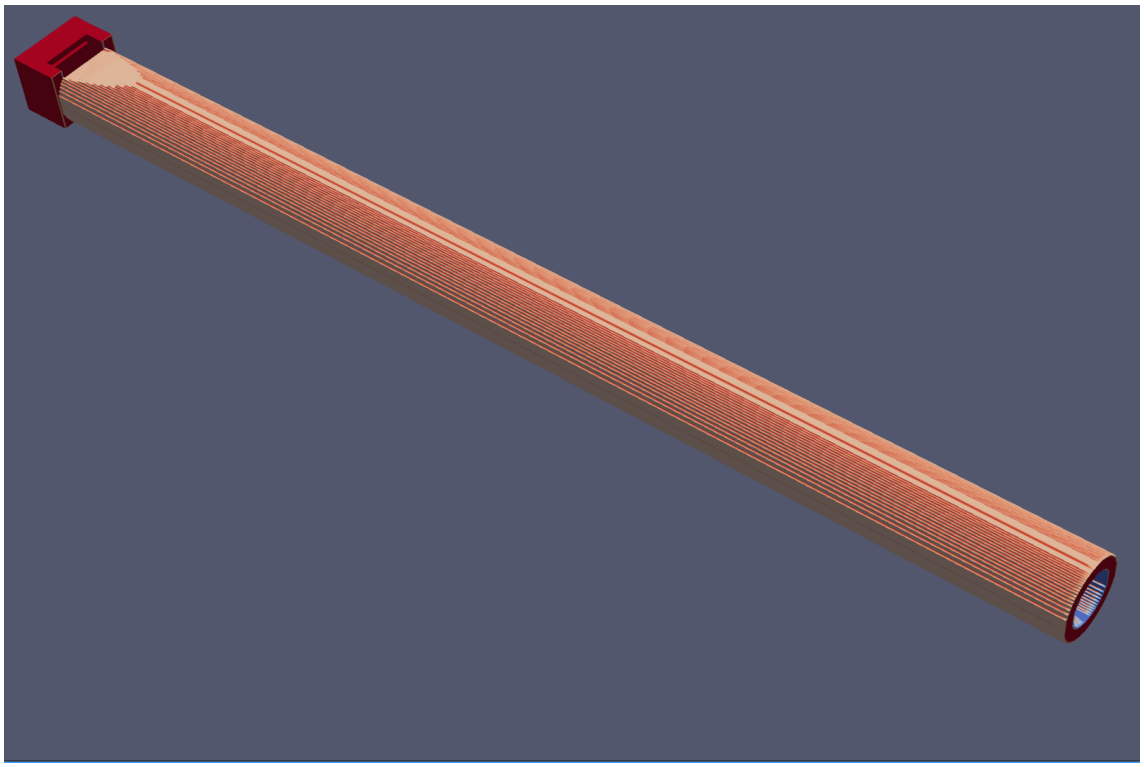

Figure 6.10: Simulated geometry of a soprano recorder illustrating the fingering for C5.

We begin our spectral analysis for the C5 with a blowing speed of 15 m/s, and ramp up time of 5 ms. The signal, or tone, that the instrument produces with these parameters can be viewed in figure 6.11a and figure 6.11b. Figure 6.11a gives 200 ms worth of tone while figure 6.11b gives 100 ms worth of tone and also has been zoomed in to emphasize the attack portion of the tone. The correlogram and FFT for these particular parameters that were calculated from the tone in figures 6.11a - 6.11b are in figures 6.12 - 6.13. We can view how the spectral content varies with time from the correlogram in figure 6.12. During the steady state or later portion of the tone, we see that the tone is dominated by the frequency that is associated with the length of the resonator (≈520 Hz). The frequency in the spectrogram at ≈260 Hz during this portion of the tone is a result of large correlations that are present at twice the period for the fundamental frequency (≈ 523 Hz) and can be ignored, i.e, this spectral feature is an *artifact*. If this correlogram had the spectral components plotted at later times (greater than 100 ms) then the correlogram would display just the two frequencies at 260 Hz and 520 Hz as can be seen in figure 6.12 at times (greater than 80 ms). We can use the green sound spectrum in figure 6.13 to verify this fact. The green sound spectrum in figure 6.13 was calculated with a 1,024 point

(23.5 ms) FFT that was centered at 110 ms - well into the steady portion of the tone. If we look closely at this green sound spectrum then we can see that the spectrum is dominated by the fundamental frequency of the recorder (≈520 Hz). There is a *slight* peak at around 260 Hz, but it is several orders of magnitude smaller than the dominant peak at 520 Hz. If we now look at the attack portion (less than 40 ms) of the tone we see a few different frequencies at 260 Hz, 400 Hz, and 800 Hz present within the spectrum. We can verify that these frequencies are real by looking at the spectrum that was calculated with the attack portion of the tone. Specifically we will refer to the *black* spectrum in figure 6.13. This sound spectrum was again calculated with a 1,024 point FFT but centered at 20 ms, well within the attack portion of the tone. Looking at the black spectrum we can see that there are indeed broad peaks centered at these frequencies. The origin of the spectral features with frequencies near 260 Hz, 400 Hz, and 800 Hz is not completely clear. Speculation on a possible origin will be discussed in section 6.4 after showing all the results of this section (section 6.3).

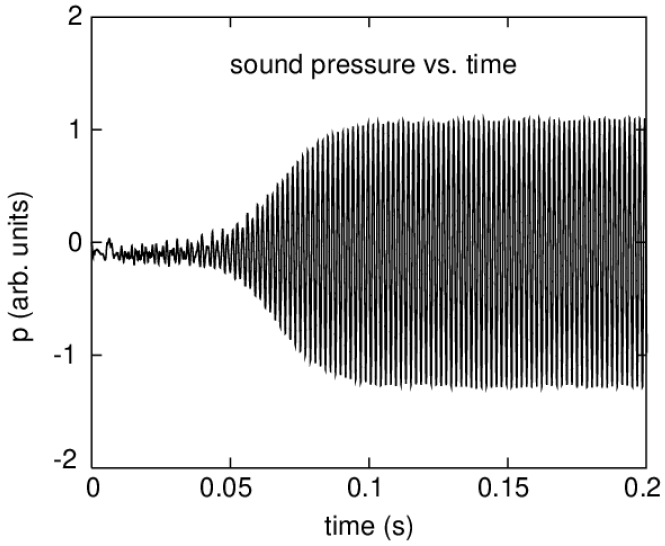

(a)

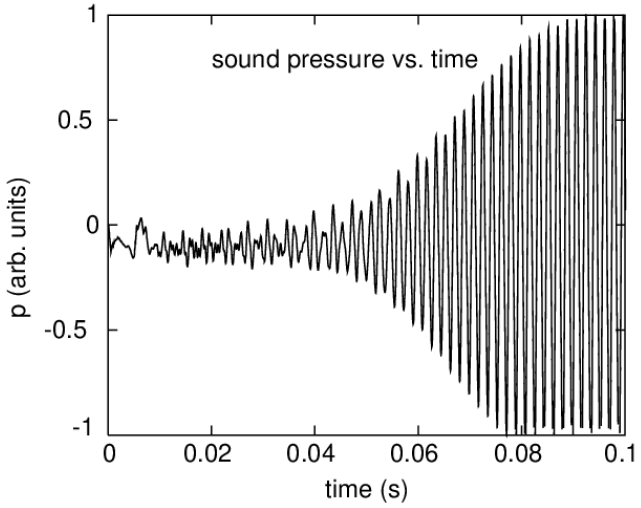

(b)

Figure 6.11: (a) ρ vs. time plot for C5 with a blowing speed of 15 m/s and a ramp up time of 5 ms. (b) ρ vs. time plot for C5 with a blowing speed of 15 m/s and a ramp up time of 5 ms. In this figure we only show the first 100 ms in order to give a good illustration of the attack portion of the tone.

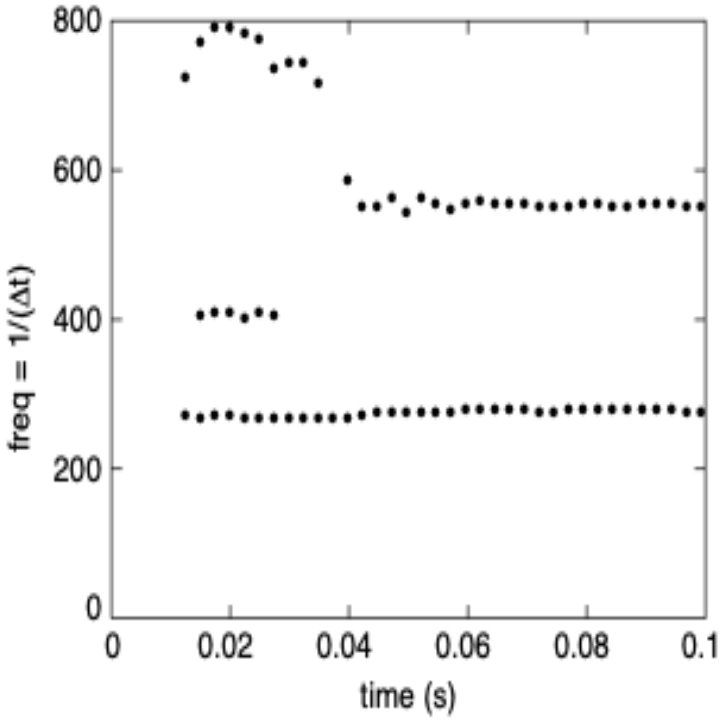

Figure 6.12: Correlogram for C5 with a blowing speed of 15 m/s, ramp up time of 5 ms. The window size is 20 ms and the starting time is at 5 ms.

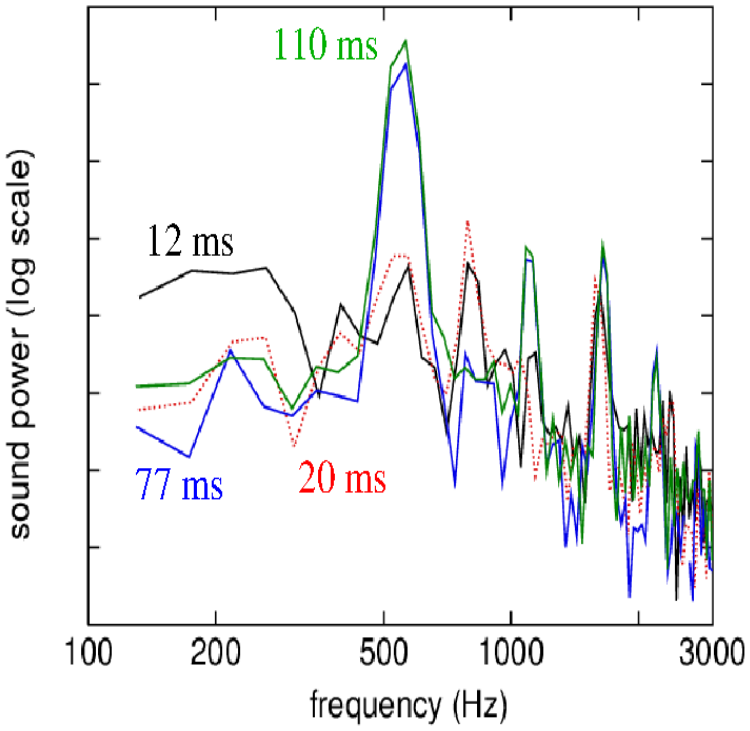

Figure 6.13: Sound spectra for C5 with a blowing speed of 15 m/s, ramp up time of 5 ms. Each spectrum was calculated with an FFT using 23 ms from figure 6.11a and 6.11b. Each FFT was calculated using 23.5 ms of data with the following midpoints for different the different colored spectra black: 12 ms, red: 20ms, blue: 77 ms, green: 110 ms.

Next, we analyze the spectral content for C5 with a blowing speed of 15 m/s and a ramp up time of 30 ms. The signal, or tone, that the instrument produces with these parameters can be viewed in figure 6.14a and figure 6.14b. Figure 6.14a gives 200 ms worth of tone while figure 6.14b gives 100 ms worth of tone and has been zoomed in to emphasize the attack portion of the tone. The correlogram and FFT for these particular parameters that were calculated from the signal in figures 6.14a and 6.14b are in figures 6.15 - 6.16. We can view how the spectral content varies with time from the correlogram in figure 6.15. During the steady state, we see similar behavior for the tone produced with a ramp up time of 5 ms - we see that the spectrum of the steady state is dominated by the frequency associated with the length of the resonator. If this correlogram had the spectral components plotted at later times (greater than 100 ms) then the correlogram would display just the two frequencies at 260 Hz and 520 Hz as can be seen in figure 6.15 at times (greater than 60 ms). Using the green spectrum, we can again ignore the frequency in the correlogram in figure 6.15 at 260 Hz using a similar argument. If we now

look at the attack portion (less than 80 ms) of the tone we see a new spectral component at 260 Hz present within the spectrum. In addition, we see that this spectral component initially has a frequency of about 200 Hz and then *slowly* increases in frequency to 260 Hz. We can verify that this frequency is real by looking at the spectrum that was calculated with the attack portion of the tone. Specifically we will refer to the *red* spectrum. This sound spectrum was again calculated with a 1,024 point FFT but centered at 20 ms, well within the attack portion of the tone. Looking at the red spectrum we can see that there is indeed a broadband peak centered at this frequency.

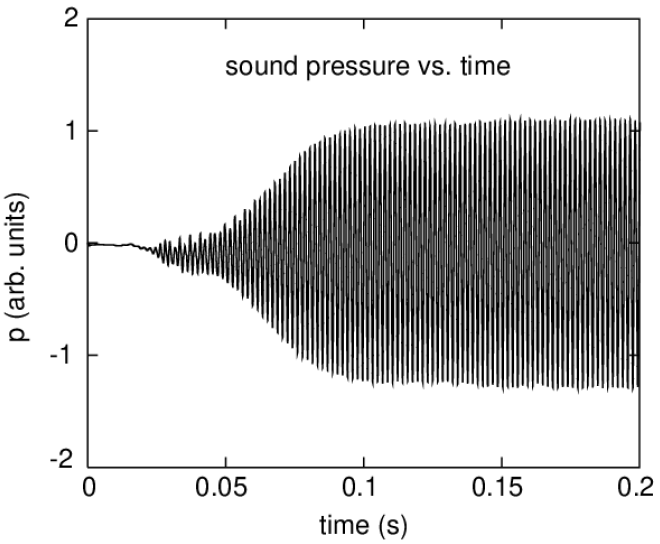

(a)

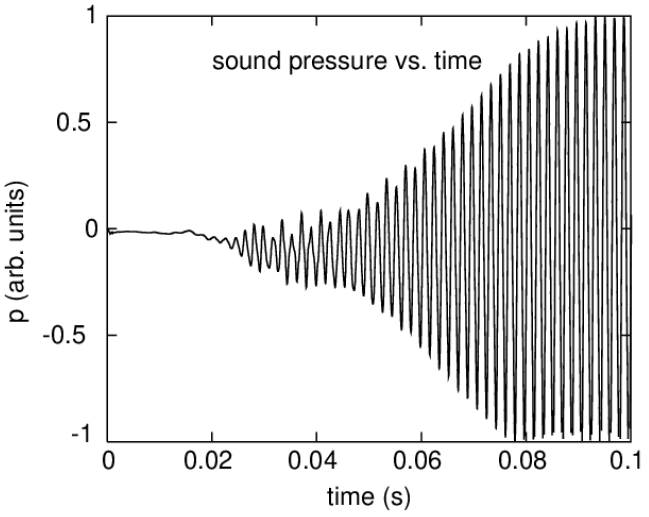

(b)

Figure 6.14: (a) ρ vs. time plot for C5 with a blowing speed of 15 m/s and a ramp up time of 30 ms. (b) ρ vs. time plot for C5 with a blowing speed of 15 m/s and a ramp up time of 30 ms. In this figure we only show the first 100 ms in order to give a good illustration of the attack portion of the tone..

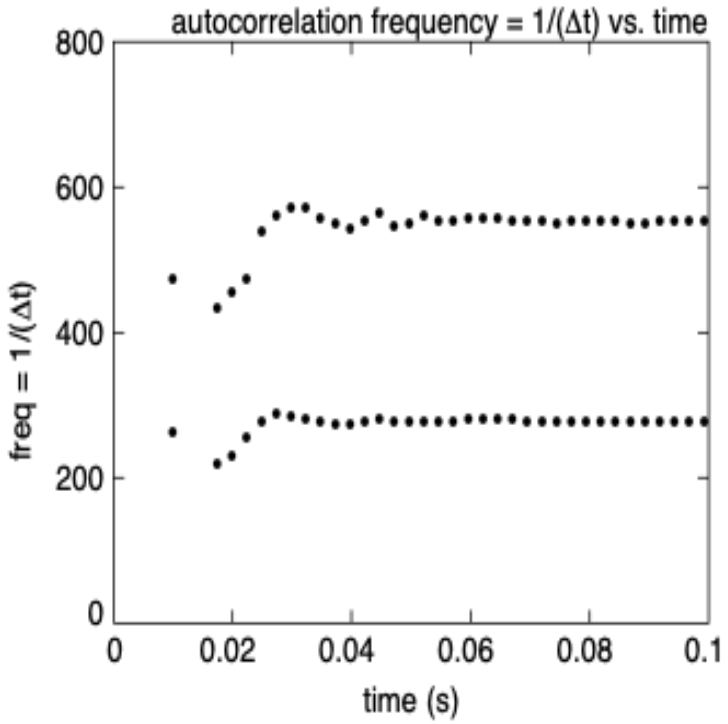

Figure 6.15: Correlogram for C5 with a blowing speed of 15 m/s, ramp up time of 30 ms. The window size is 20 ms and the starting time is at 5 ms.

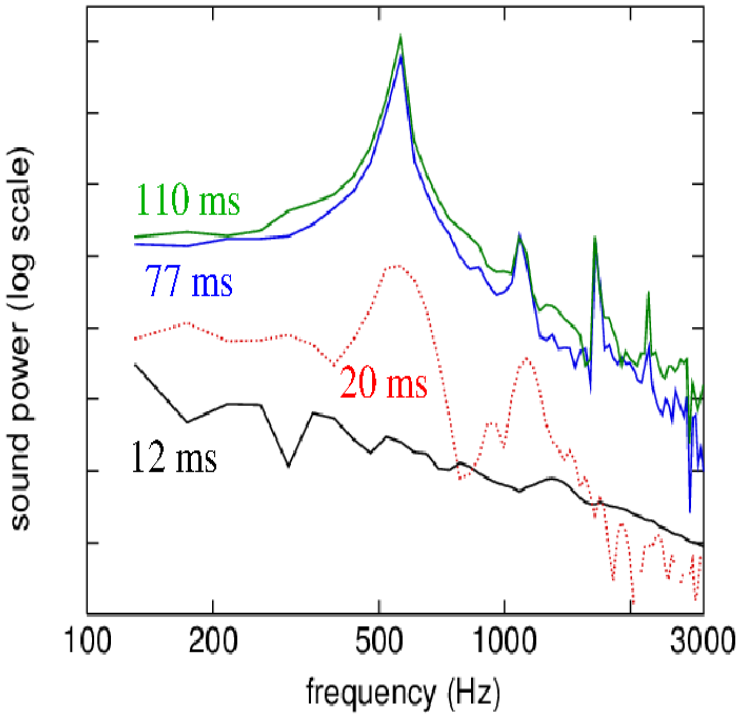

Figure 6.16: Sound spectrum for C5 with a blowing speed of 15 m/s, ramp up time of 30 ms. Each spectrum was calculated with an FFT using 23 ms from figure 6.14a and 6.14b. Each FFT was calculated using 23.5 ms of data with the following midpoints for different the different colored spectra black: 12 ms, red: 20ms, blue: 77 ms, green: 110 ms.

We next analyze the spectral content for a C5 but now the blowing speed has been decreased from 15 m/s to 12.5 m/s. In addition, the ramp up time is set to 5 ms. The tone that the instrument produces with these parameters can be viewed in figures 6.17a - 6.17b. Figure 6.17b shows the attack portion of the tone in detail and when we compare to the attack portion for a blowing speed of 15 m/s and ramp up time of 5 ms in figure 6.11b, we can see the nonlinear differences in these attack portions when the blowing speed is changed. The correlogram and FFT for these parameters can be viewed in figures 6.18 - 6.19. We can see how the spectral content varies with time from the correlogram in figure 6.18. During the steady state (greater than 30 ms) the fundamental frequency of the C5 (520 Hz) and a second frequency (260 Hz) are present in the spectrum. Analyzing the green sound spectrum in figure 6.19, it clearly shows that both of these frequencies are real, but the frequency at 520 Hz dominates the spectrum while the frequency at 260 Hz is very low in power. However, both of these frequencies will contribute to the color of the tone during the steady state portion of the tone. Focusing attention

to the attack portion of the tone (less than 30 ms) we analyze the same correlogram (fig. 6.18) but consider the *black* sound spectrum in figure 6.19. Figure 6.18 shows that, again, there are two potential frequencies present in the tone: the fundamental frequency of C5 (520 Hz) and the inharmonic frequency at 260 Hz. Interestingly, if we refer to figure 6.19, *both* of these frequencies are real and have approximately the same power and therefore should contribute equally to the color of the tone.

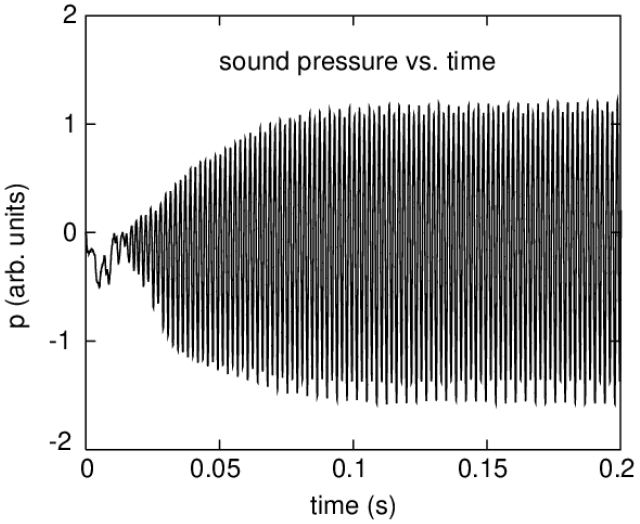

(a)

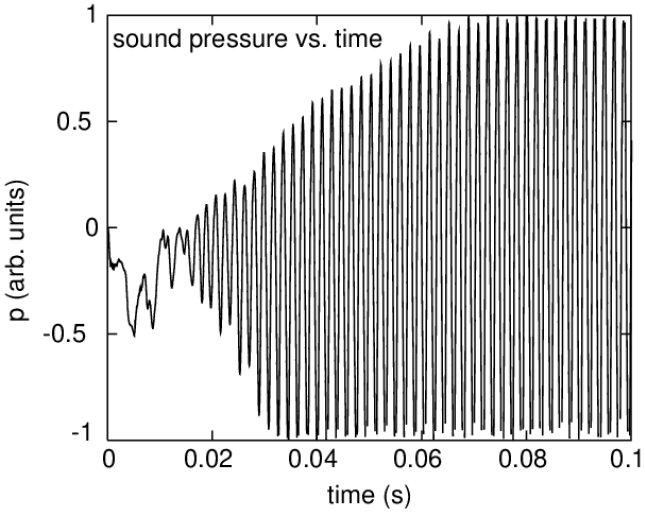

(b)

Figure 6.17: (a) ρ vs. time plot for C5 with a blowing speed of 12.5 m/s and a ramp up time of 5 ms. (b) ρ vs. time plot for C5 with a blowing speed of 12.5 m/s and a ramp up time of 5 ms. In this figure we only show the first 100 ms in order to give a good illustration of the attack portion of the tone..

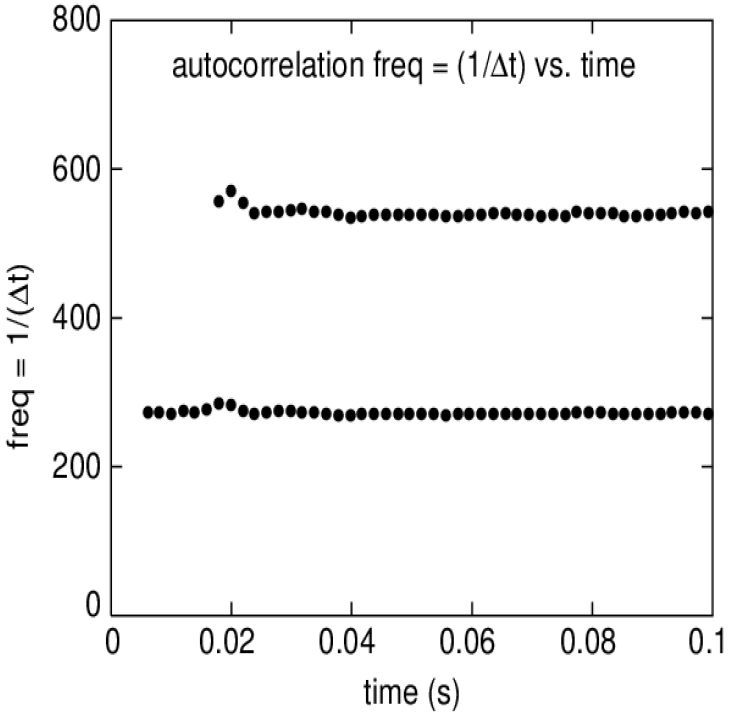

Figure 6.18: Correlogram for C5 with a blowing speed of 12.5 m/s, ramp up time of 5 ms. The window size is 4 ms and the starting time is at 2 ms.

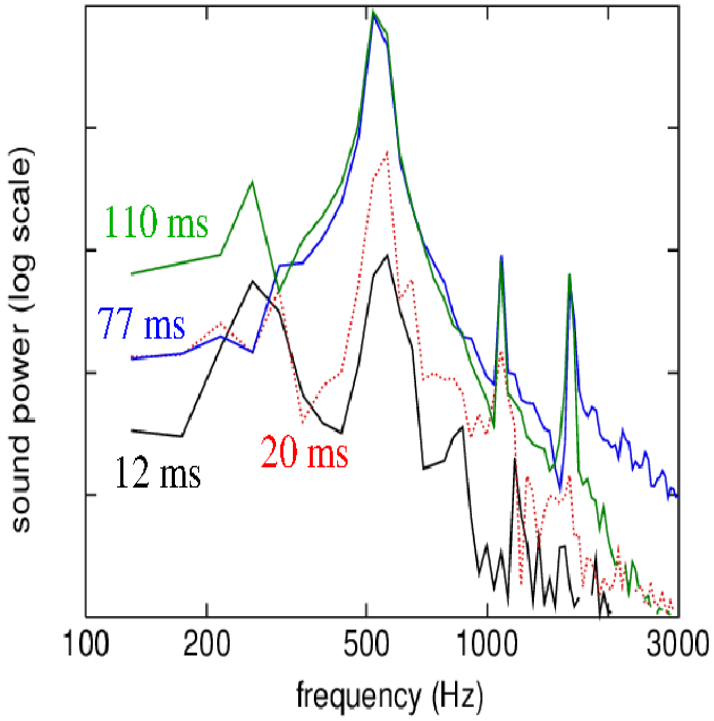

Figure 6.19: Sound spectrum for C5 with a blowing speed of 12.5 m/s, ramp up time of 5 ms. Each spectrum was calculated with an FFT using 23 ms from figure 6.17a and 6.17b. Each FFT was calculated using 23.5 ms of data with the following midpoints for different the different colored spectra black: 12 ms, red: 20ms, blue: 77 ms, green: 110 ms.

We now analyze the spectral content for a C5 for the same blowing speed, 12.5 m/s, with the ramp up time increased to 30 ms. The tone that the instrument produces with these parameters can be viewed in figures 6.20a - 6.20b. Figure 6.20b shows the attack portion of the tone in detail. The correlogram and FFT for these parameters can be viewed in figures 6.21 - 6.22. We can see how the spectral content varies with time from the correlogram in figure 6.21. During the steady state (greater than 60 ms) the fundamental frequency of the C5 (520 Hz) and an inharmoinc frequency (260 Hz) are present in the steady state spectrum. Analyzing the green sound spectrum in figure 6.22, it is clear that only the fundamental frequency of the C5 (520 hz) is present in the spectrum. Focusing our attention to the attack portion of the tone (less than 30 ms) we analyze the same correlogram (fig. 6.21) but now analyze the *black* sound spectrum in figure 6.22. Figure 6.21 shows that, again, there are two frequencies present in the tone: the fundamental frequency of C5 (520 Hz) and the inharmonic frequency at 260 Hz. What makes the black spectrum in figure 6.22 particularly interesting is the present of a dominant broadband

spectral frequency centered at 260 Hz. In addition, the fundamental frequency of the C5, while present in the tone is weak in power when compared to the broadband frequency. Together, figure 6.21 - 6.22 show that as you increase the ramp up time, the spectrum increasingly has broadband content present with increasing power.

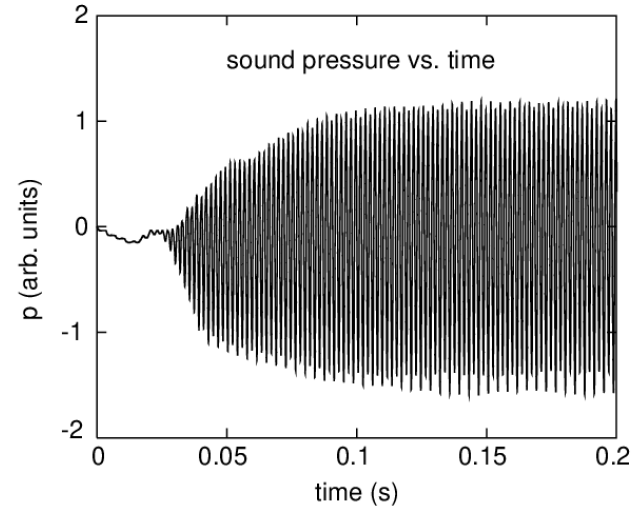

(a)

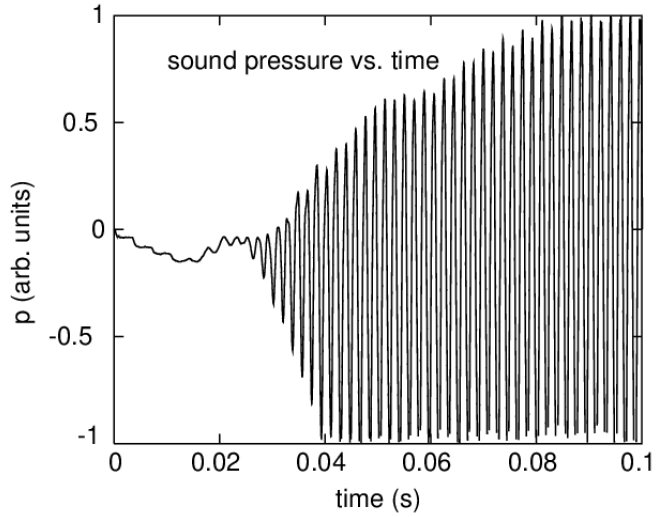

(b)

Figure 6.20: (a) ρ vs. time plot for C5 with a blowing speed of 12.5 m/s and a ramp up time of 30 ms. (b) ρ vs. time plot for C5 with a blowing speed of 12.5 m/s and a ramp up time of 30 ms. In this figure we only show the first 100 ms in order to give a good illustration of the attack portion of the tone.

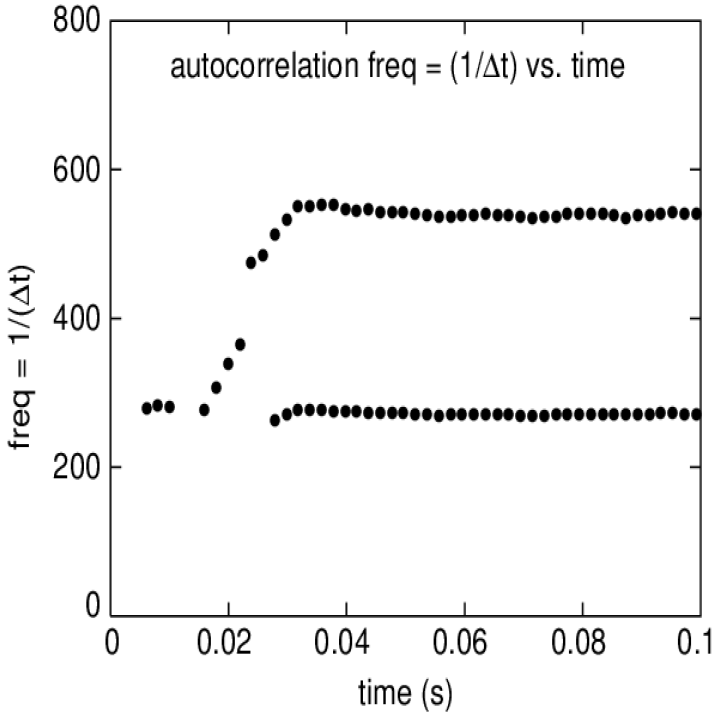

Figure 6.21: Correlogram for C5 with a blowing speed of 12.5 m/s, ramp up time of 30 ms. The window size is 4 ms and the starting time is at 2 ms.

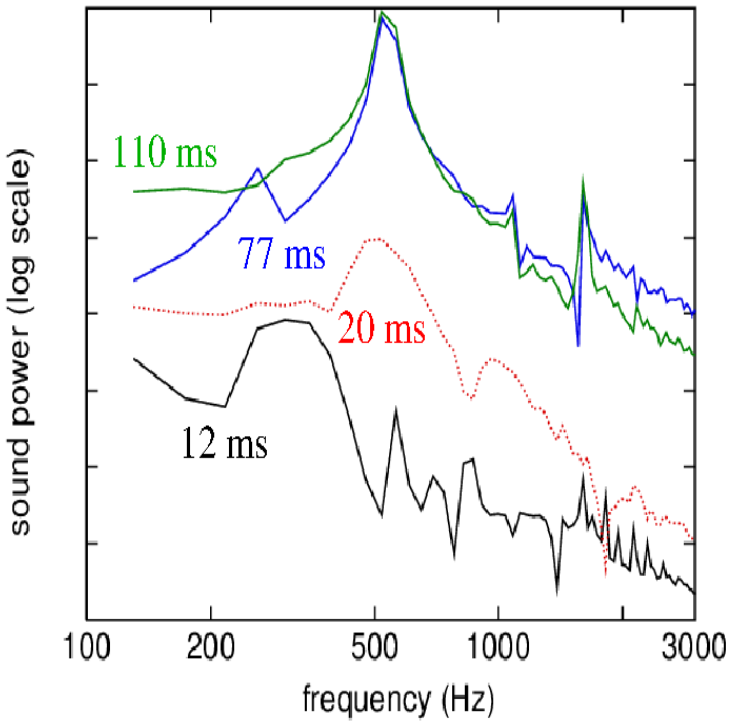

Figure 6.22: Sound spectrum for C5 with a blowing speed of 12.5 m/s, ramp up time of 30 ms. Each spectrum was calculated with an FFT using 23 ms from figure 6.20a and 6.20b. Each FFT was calculated using 23.5 ms of data with the following midpoints for different the different colored spectra black: 12 ms, red: 20ms, blue: 77 ms, green: 110 ms.

6.3.2 Spectral Analysis: E5

Section 6.3.1 focused on a single note, i.e, the C5 (520 Hz). In this subsection we study the E5 (659 Hz) at two different ramp up times, 5 ms and 30 ms. All the results shown for the E5 in this subsection are with the blowing speed at 15 m/s. Figure 6.23 shows the simulated geometry for the soprano recorder and the tone hole placement necessary to produce E5. All of the parameters used in this subsection are summarized in table 6.1.

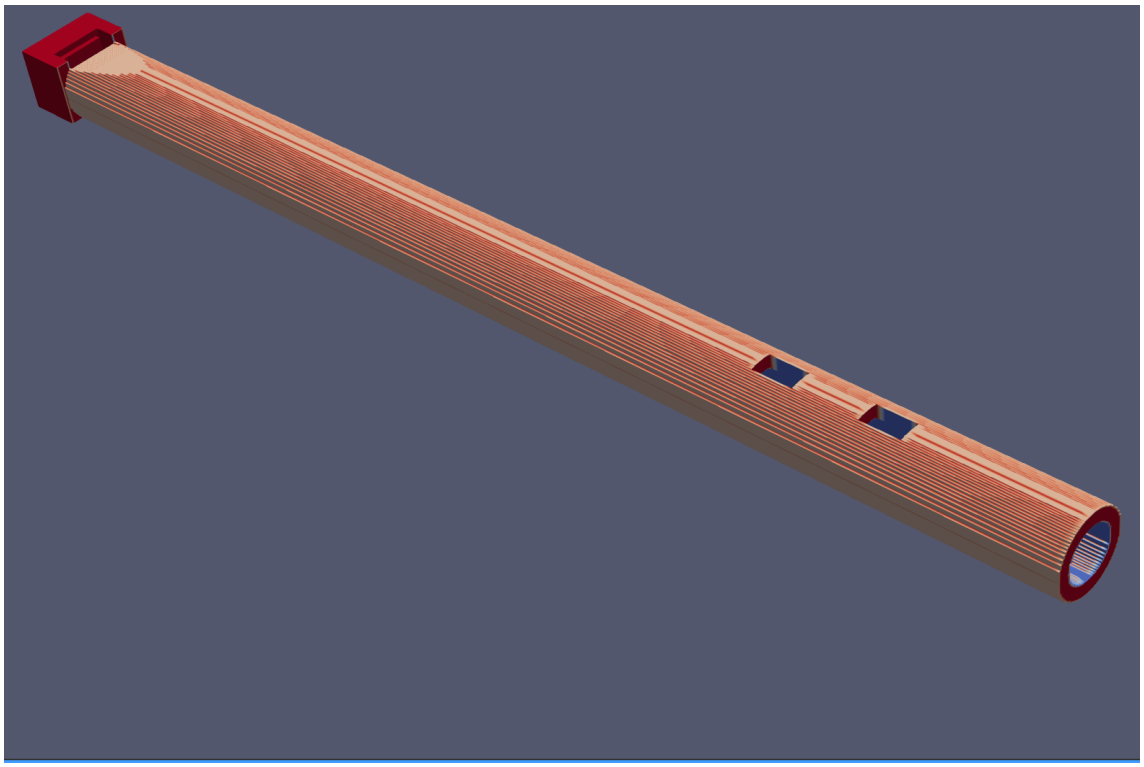

Figure 6.23: Simulated geometry of a soprano recorder illustrating the fingering for E5.

We begin this subsection with an analysis of the E5 at a ramp up time of 5 ms. The tone that the instrument produces can be found in figure 6.24a - 6.24b. Figure 6.24a displays 200 ms worth of tone while figure 6.24b displays 100 ms worth of tone in order to better show the attack region. Note the difference in the attack transient in figure 6.11b versus the attack in figure 6.24b. Keeping the parameters the same but changing the note can have dramatic and nonlinear effects on the attack transient and the comparison between figures 6.11b and 6.24b illustrates this. The correlogram and FFT for these particular parameters that were constructed from the tone in figures 6.24a - 6.24b can be found in figures 6.25 - 6.26. We can see how the spectral content varies with time from the correlogram in figure 6.25. In this correlogram we can see that the after about 40 ms, the approximate steady state time region, the fundamental frequency of the E5 (659 Hz) has had time to settle in. In addition we see that a frequency at around 370 Hz *might* be present in the spectrum during this time interval as well but upon analyzing the green (steady state) sound spectrum in figure 6.26 we can see that this spectral component is an artifact. Next we analyze the spectral content of the attack portion of the tone which is approximately less than 40 ms. From the correlogram in figure 6.25, there is only *one*

frequency present in the spectrum for the first 20 ms. In the first 20 ms, the frequency steadily increases from a value of approximately 320 Hz to a value of about 370 Hz. In addition, after 20 ms the fundamental frequency of E5 (659 Hz) then becomes present in the tone. To verify the presence of the spectral component at $\approx$ 370 Hz, we now look at the black sound spectrum calculated in the attack portion of the tone in figure 6.26. If we look closely at this spectrum we can see that there are two spectral components centered at approximate 350 Hz and 659 Hz. The component at 350 Hz dominates the spectrum during this time period. This analysis of the E5 at a ramp up time of 5 ms demonstrates the presence of lower frequency inharmonic spectral components during the attack region (less than 40 ms). However, during the steady state region (greater than 40 ms) the fundamental frequency (659 Hz) dominates the spectrum while lower frequency content goes aways. Lastly, the correlogram in figure 6.25 shows that the fundamental and dominant component takes time to 'settle in'.

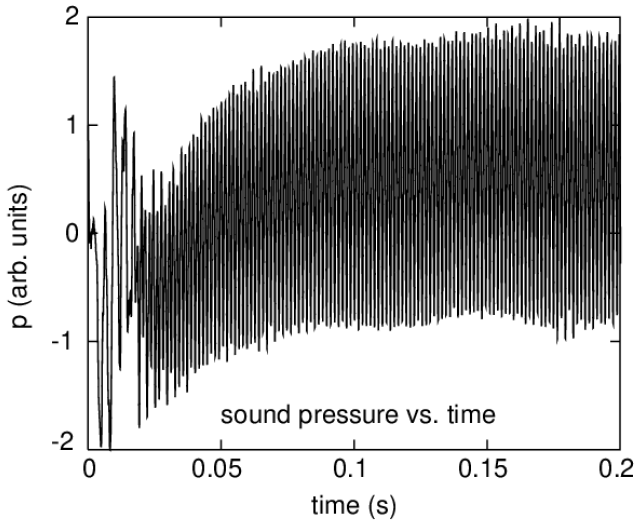

(a)

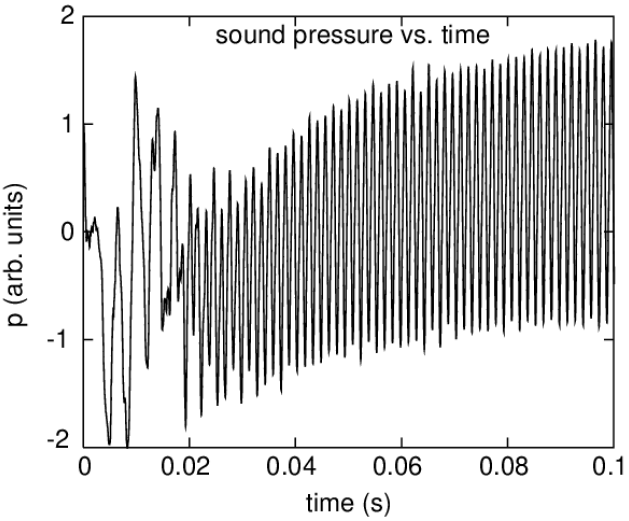

(b)

Figure 6.24: (a) ρ vs. time plot for E5 with a blowing speed of 15 m/s and a ramp up time of 5 ms. (b) ρ vs. time plot for E5 with a blowing speed of 15 m/s and a ramp up time of 5 ms. In this figure we only show the first 100 ms in order to give a good illustration of the attack portion of the tone.

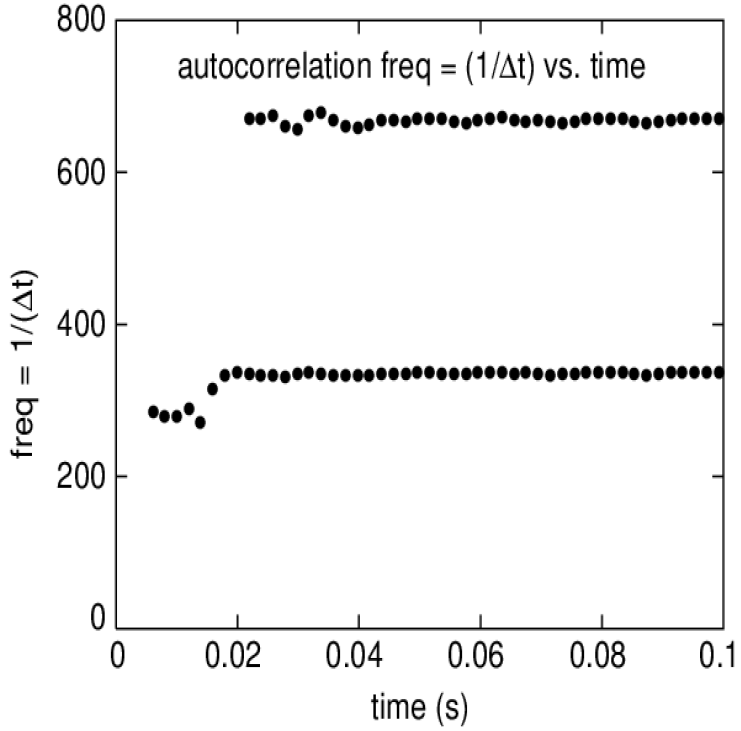

Figure 6.25: Correlogram for E5 with a blowing speed of 15 m/s, ramp up time of 5 ms. The window size is 4 ms and the starting time is at 2 ms.

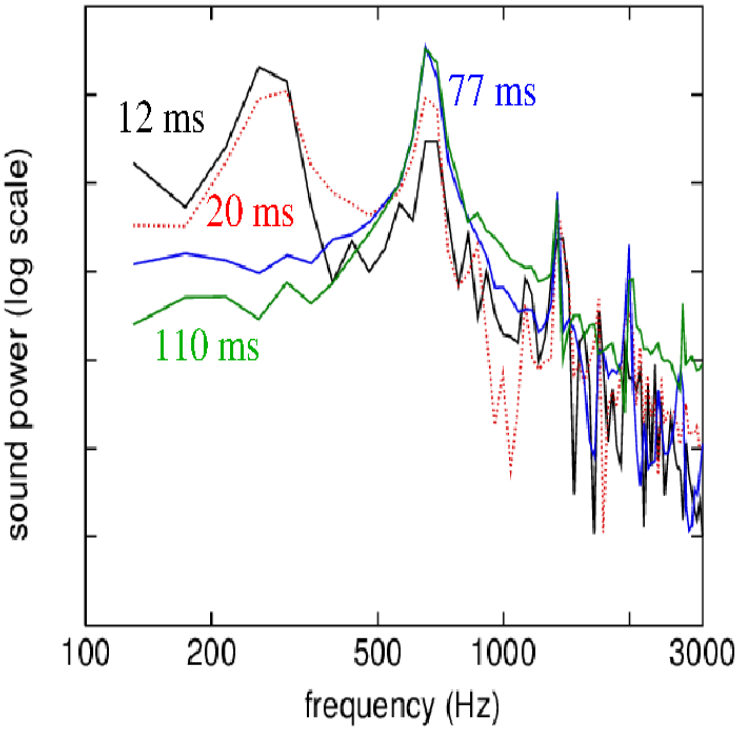

Figure 6.26: Sound spectrum for E5 with a blowing speed of 15 m/s, ramp up time of 5 ms. Each spectrum was calculated with an FFT using 23 ms from figure 6.24a and 6.24b. Each FFT was calculated using 23.5 ms of data with the following midpoints for different the different colored spectra black: 12 ms, red: 20ms, blue: 77 ms, green: 110 ms.

We next analyze the results of the E5 but now we increase the ramp up time to 30 ms. The blowing speed of 15 m/s remains unchanged. The tone that the instrument produces can be found in figure 6.27a - 6.27b. Figure 6.27a displays 200 ms worth of tone while figure 6.27b displays only 100 ms worth of tone in order to better show the attack region.The correlogram and FFT for these particular parameters were constructed from the tone in figures 6.28 - 6.29. Using the correlogram in figure 6.28 we can get a sense of how the spectral content varies with time. First we analyze the steady state portion of the tone which is approximately greater than 40 ms. If we refer to the correlogram in figure 6.28 there are two spectral components that appear to be present in the tone: one component at 659 Hz and another at approximately 370 Hz. Looking at the green sound spectrum, which was calculated during the steady state, the component with frequency 659 Hz dominates the spectrum while the component with frequency of 370 Hz appears to be an artifact. The frequency at 370 Hz seems to be an artifact because it has very little power when compared to the fundamental component (frequency 659

Hz). We now analyze the attack portion of the tone which is the region before or less than 40 ms of time. Referring to the correlogram in figure 6.28 we see some interesting behavior of the attack region before 20 ms. During this early region there do not seem to be spectral components with well defined frequencies but rather a gradient of spectral content that increases in frequency from about 250 Hz to approximately 400 Hz. The black sound spectrum reinforces these findings. The black spectrum shows the presence of low frequency content below 500 Hz. After 20 ms but before 40 ms, the attack region now seems to have two spectral components that seem to slowly increase to 370 Hz and 659 Hz. If we refer to the *red* sound spectrum, which was calculated in this region, we see that there are two broadband peaks at 370 Hz and 659 Hz. To summarise, during the earliest part of the attack region there appears to be low frequency content with minimal high frequency content. During the late stages of the attack region the spectral content becomes more well defined and increases to frequencies of 370 Hz and 659 Hz; these frequencies are seen in the red sound spectrum in figure 6.29. During the steady state portion of the one there is one dominating frequency of 659 Hz with weak higher harmonic content (1000+ Hz).

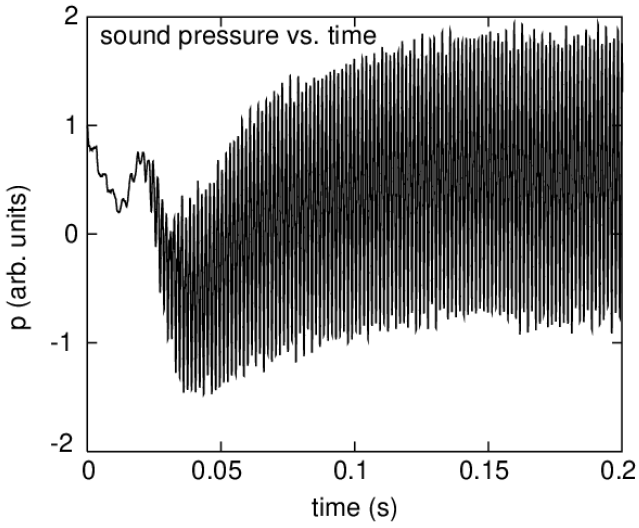

(a)

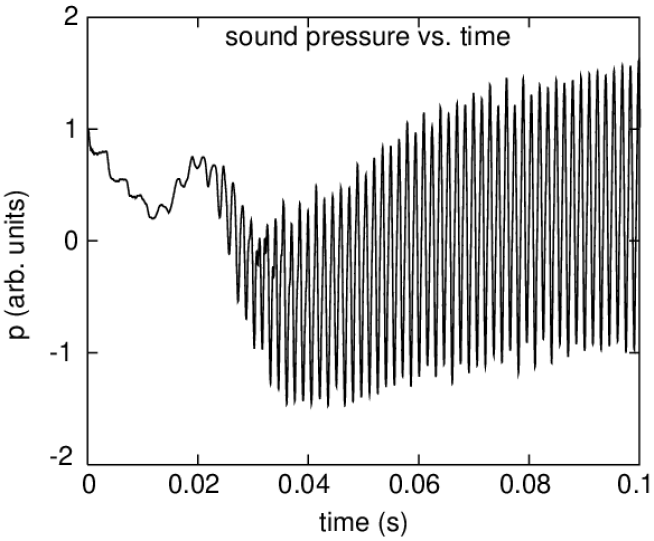

(b)

Figure 6.27: (a) ρ vs. time plot for E5 with a blowing speed of 15 m/s and a ramp up time of 30 ms. (b) ρ vs. time plot for E5 with a blowing speed of 15 m/s and a ramp up time of 30 ms. In this figure we only show the first 100 ms in order to give a good illustration of the attack portion of the tone.

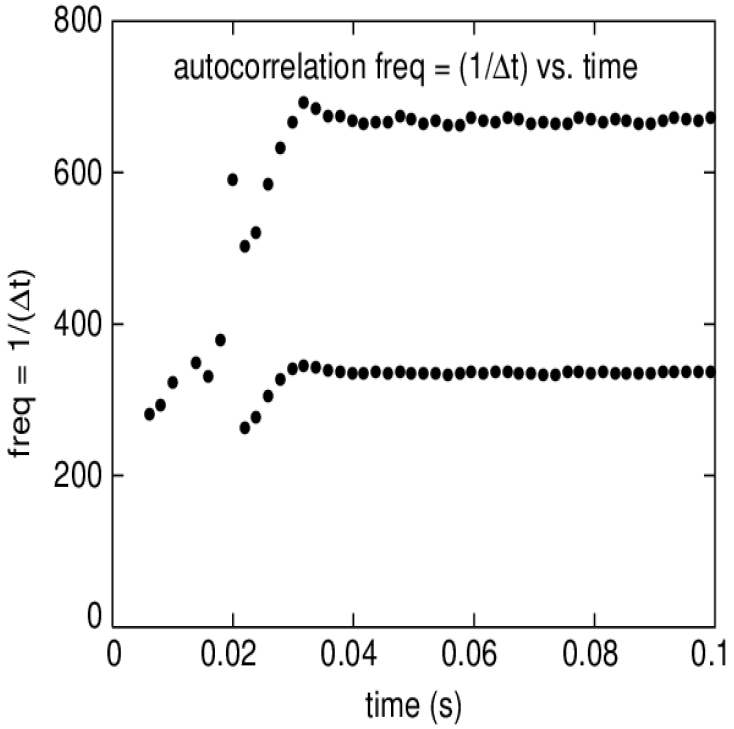

Figure 6.28: Correlogram for E5 with a blowing speed of 15 m/s, ramp up time of 30 ms. The window size is 4 ms and the starting time is at 2 ms.

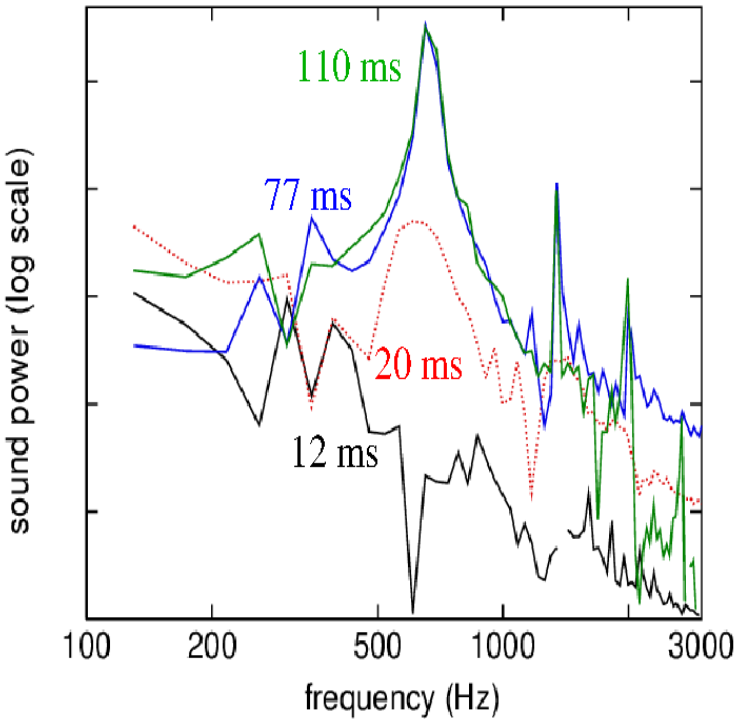

Figure 6.29: Sound spectrum for E5 with a blowing speed of 15 m/s, ramp up time of 30 ms. Each spectrum was calculated with an FFT using 23 ms from figure 6.27a and 6.27b. Each FFT was calculated using 23.5 ms of data with the following midpoints for different the different colored spectra black: 12 ms, red: 20ms, blue: 77 ms, green: 110 ms.

6.3.3 Spectral Analysis: G5

Thus far we have discussed on two notes: C5 and E5 in sections 6.3.1 and 6.3.2 respectively. In this subsection we will discuss G5 (784 Hz) at a constant blowing speed (17 m/s) and two ramp up times (5 ms and 30 ms). Figure 6.30 shows the simulated geometry for the soprano recorder and the tone hole placement necessary to produce G5. All of the parameters are summarized in table 6.1.

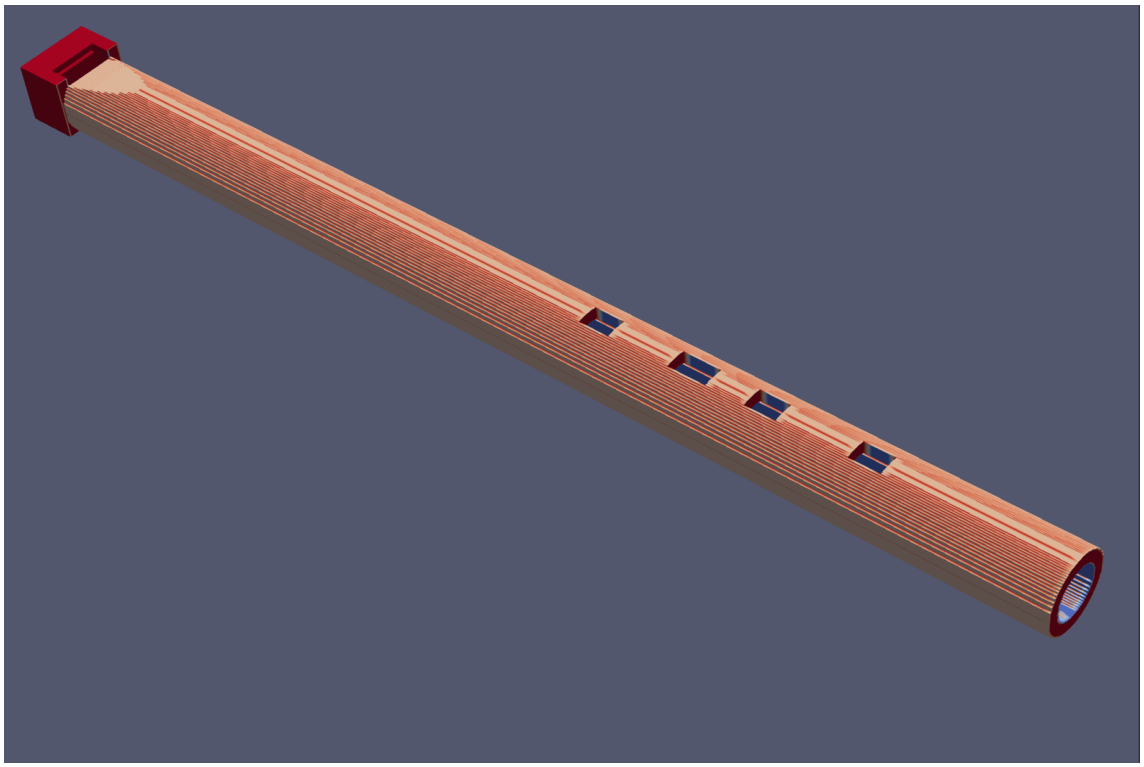

Figure 6.30: Simulated geometry of a soprano recorder illustrating the fingering for G5.

We begin this subsection with an analysis of the G5 at a blowing speed of 17 m/s and a ramp up time of 5 ms. The tone that the instrument produces using these parameters can be found in figures 6.31a - 6.31b. Figure 6.31a displays 200 ms worth of tone while figure 6.31b displays 100 ms worth of tone in order to better show the attack region of the tone. The correlogram and FFT constructed from the parameters just mentioned can be found in figures 6.32 - 6.33. From the correlogram in figure 6.32 we can see how the spectral content varies with time. First we will analyze the steady state region of the tone which happens after approximately 40 ms. In the steady state region of the tone for the other two notes (C5 and E5) there were only two stable frequencies present in their respective correlograms. *However*, in this correlogram we now see the presence of three potential stable frequencies. The fundamental frequency of the E5 has a value of 784 Hz and the other two inharmonic frequencies have approximate values of 260 Hz and 400 Hz. If we refer to the green sound spectrum in figure 6.33 then we can see that only the fundamental frequency at 784 Hz and its second mode are present in the spectrum. Therefore the lower frequency peaks in the correlogram (260 Hz and 400 Hz) in the steady portion of the tone are artifacts. We now analyze the attack portion (less than 40 ms)

of the tone for the G5 with a blowing speed of 17 m/s and a ramp up time of 5 ms. In the correlogram in figure 6.32 we again see the presence of three different spectral features in the tone with frequencies 260 Hz, 400 Hz, and 784 Hz. If we refer to the black sound spectrum in figure 6.33 then we verify the presence of all three of these features. First, the fundamental spectral feature (frequency 784 Hz) is the dominant feature in the spectrum. In addition, we can verify the presence of the lower frequency spectral content (with frequencies 260 Hz and 400 Hz) by noting the broadband frequency centered at 260 Hz. This broadband feature has a width that covers frequencies from below 200 Hz to well above 400 Hz so it encompasses both the 260 Hz and 400 Hz features; this broadband content has a similar magnitude of power when compared to the fundamental frequency. In summary, the steady state portion of the tone is dominated by the fundamental harmonic (784 Hz) while the attack portion of the tone adds the presence of two inharmonic spectral features, one with frequency 260 Hz and the other at 400 Hz.

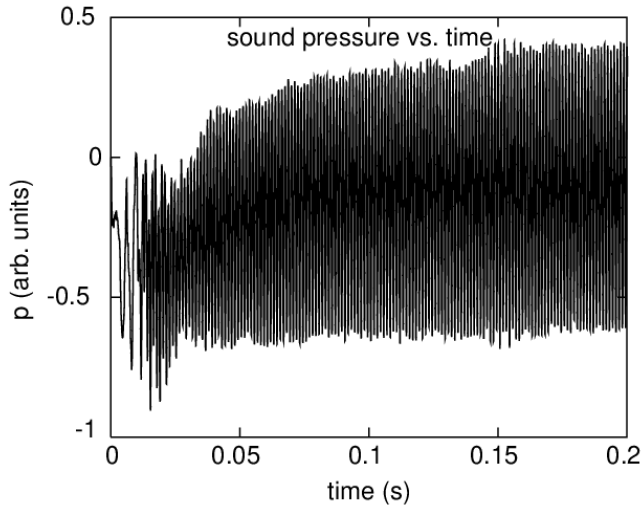

(a)

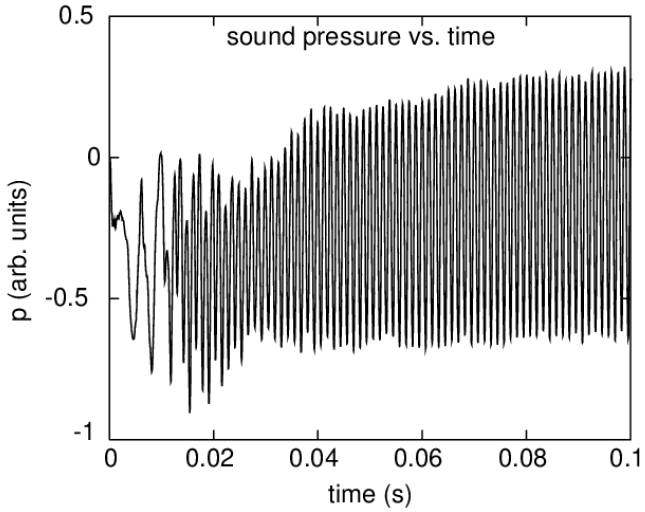

(b)

Figure 6.31: (a) ρ vs. time plot for G5 with a blowing speed of 17 m/s and a ramp up time of 5 ms. (b) ρ vs. time plot for G5 with a blowing speed of 17 m/s and a ramp up time of 5 ms. In this figure we only show the first 100 ms in order to give a good illustration of the attack portion of the tone.

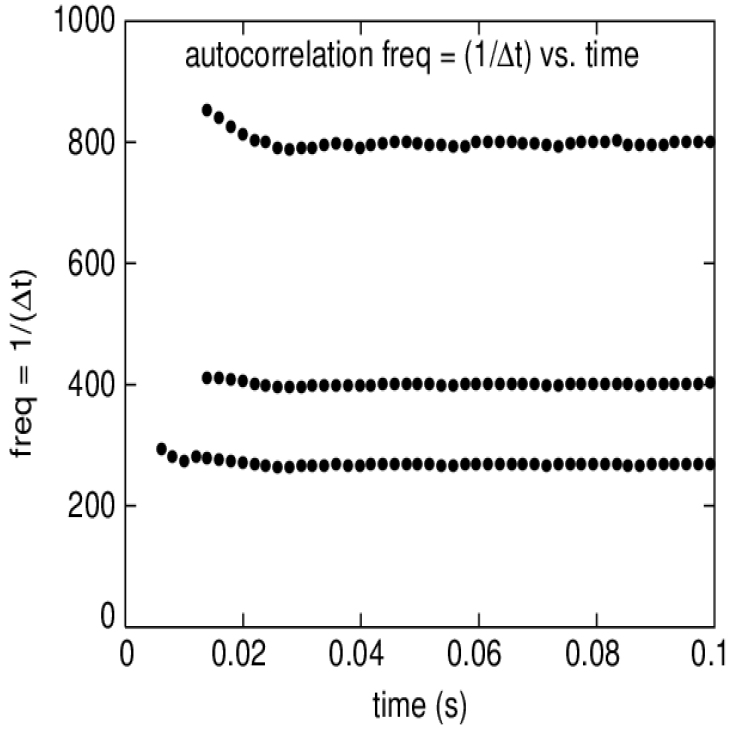

Figure 6.32: Correlogram for G5 with a blowing speed of 17 m/s, ramp up time of 5 ms. The window size is 4 ms and the starting time is at 2 ms.

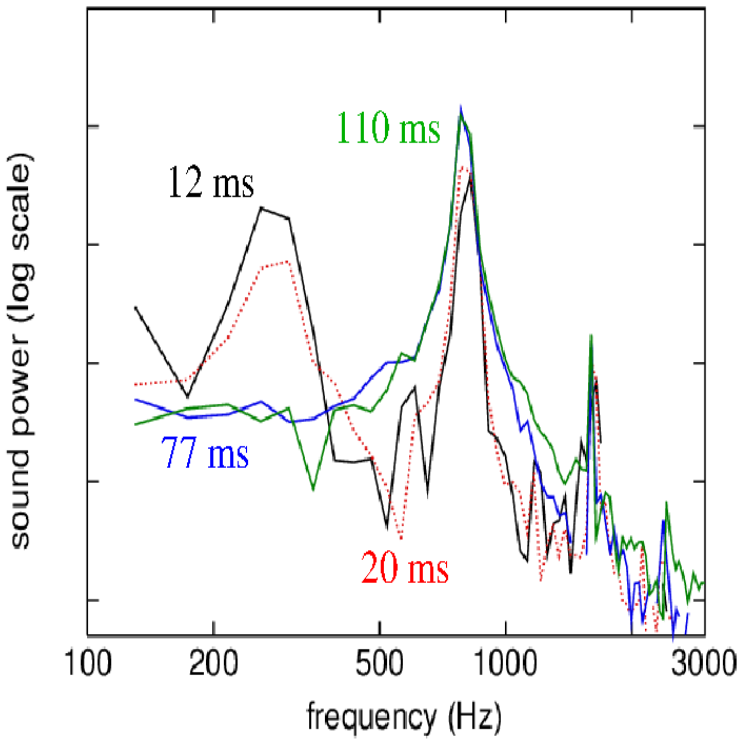

Figure 6.33: Sound spectrum for G5 with a blowing speed of 17 m/s, ramp up time of 5 ms. Each spectrum was calculated with an FFT using 23 ms from figure 6.31a and 6.31b. Each FFT was calculated using 23.5 ms of data with the following midpoints for different the different colored spectra black: 12 ms, red: 20ms, blue: 77 ms, green: 110 ms.

We next analyze the results of the G5 but now we increase the ramp up time to 30 ms. The tone that the instrument produces can be found in figures 6.34a - 6.34b. Figure 6.34a displays 200 ms worth of tone while figure 6.34b displays 100 ms worth of tone in order to better show the attack region. The correlogram and FFT can be found in figures 6.35 - 6.36. From the correlogram in figure 6.35 we can observe how the spectral content varies with time. First we will analyze the steady region of the tone which starts at approximately 40 ms and persists for the remainder of the time the instrument is played. In the steady state region of the tone we again see the presence of three possible spectral features with frequencies of 784 Hz, approximately 400 Hz, and 260 Hz. If we consider the green sound spectrum in figure 6.36 then we observe that the spectrum is dominated by the spectral feature that represents the fundamental mode of the G5. In addition, there are two high frequency spectral features that represent higher order modes of the fundamental. We now analyze the attack region of the tone which takes place before 40 ms. We first consider the interval from 0 ms - 20 ms. For this

purpose we analyze the black spectrum in figure 6.36. We observe a behavior in this region for this ramp up time (30 ms) that is similar to the E5 at the same ramp up time: before 20 ms there does not appear to be any stable frequency but rather low frequency content that seem to be slowly increasing. If we refer to the black sound spectrum in figure 6.36 then we can see the presence of low frequency content. If we now consider the interval of time from 20 ms to 40 ms, we now see the presence of three possible features present in the tone: one with frequency 260 Hz, another with 400 Hz, and the last frequency is the fundamental mode associated with the G5 (784 Hz). If we refer to the red spectrum in figure 6.36 then we see the presence of only the fundamental feature (784 Hz). In summary, the steady state portion of the tone for this ramp up time has one dominant frequency at 784 Hz with faint higher frequency content while the attack region has low frequency content from 0 ms to 20 ms and then a broadband feature centered at 784 Hz from 20 ms to 40 ms.

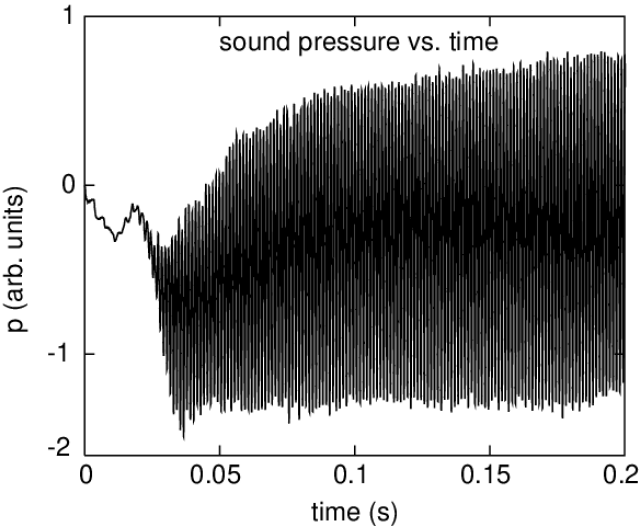

(a)

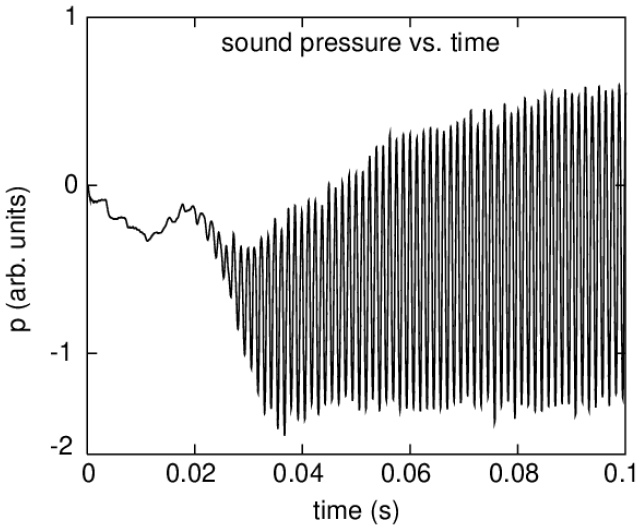

(b)

Figure 6.34: (a) ρ vs. time plot for G5 with a blowing speed of 17 m/s and a ramp up time of 30 ms. (b) ρ vs. time plot for G5 with a blowing speed of 17 m/s and a ramp up time of 30 ms. In this figure we only show the first 100 ms in order to give a good illustration of the attack portion of the tone.

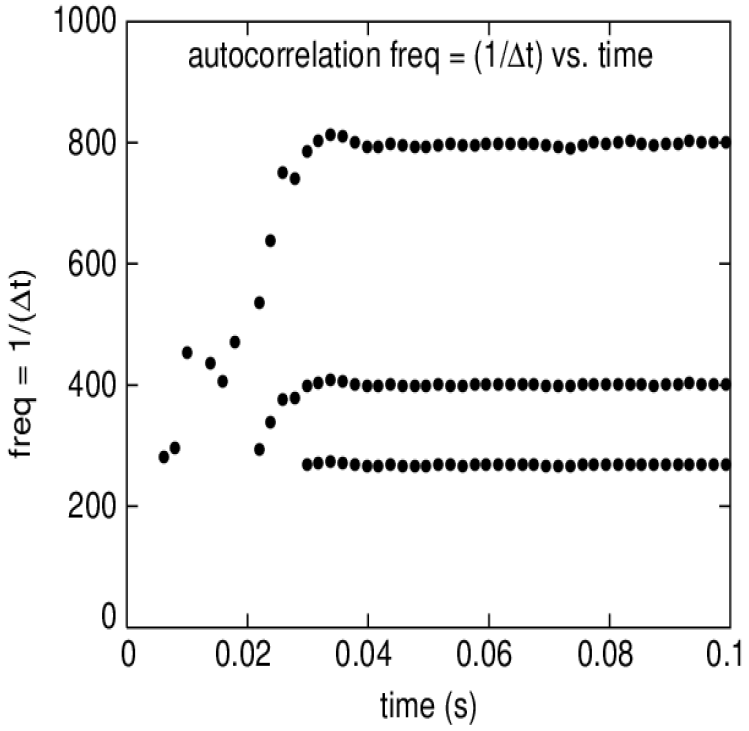

Figure 6.35: Correlogram for G5 with a blowing speed of 17 m/s, ramp up time of 30 ms. The window size is 4 ms and the starting time is at 2 ms.

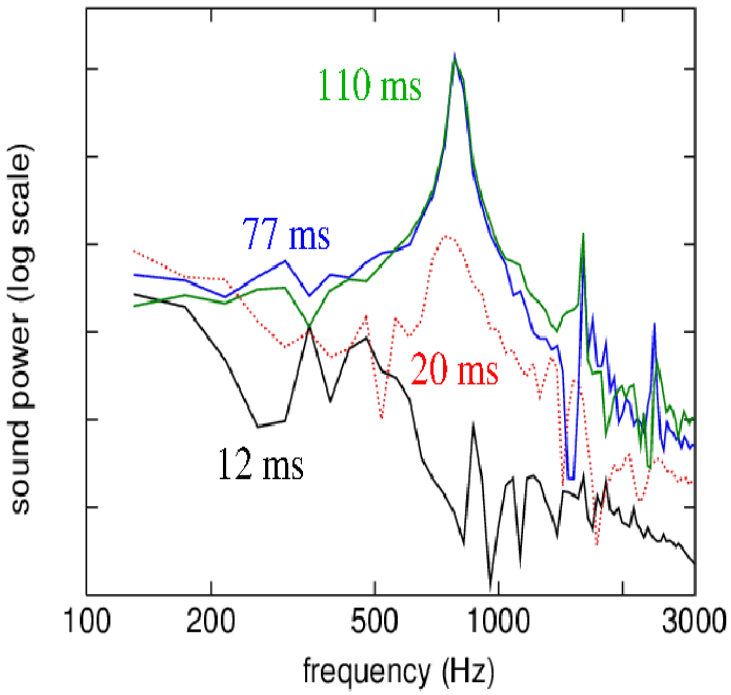

Figure 6.36: Sound spectrum for G5 with a blowing speed of 17 m/s, ramp up time of 30 ms. Each spectrum was calculated with an FFT using 23 ms from figure 6.34a and 6.34b. Each FFT was calculated using 23.5 ms of data with the following midpoints for different the different colored spectra black: 12 ms, red: 20ms, blue: 77 ms, green: 110 ms.

6.3.4 Spectral Analysis: C6

Thus far we have discussed three notes: C5, E5, and G5 in sections 6.3.1, 6.3.2, and 6.3.3 respectively. In this subsection we will discuss the results of the final note: C6 (1046 Hz) at a constant blowing speed (21 m/s) and two ramp up times (5 ms and 30 ms). Figure 6.37 shows the simulated geometry for the soprano recorder and the tone hole placement necessary to produce C6. All of the parameters are summarized in table 6.1.

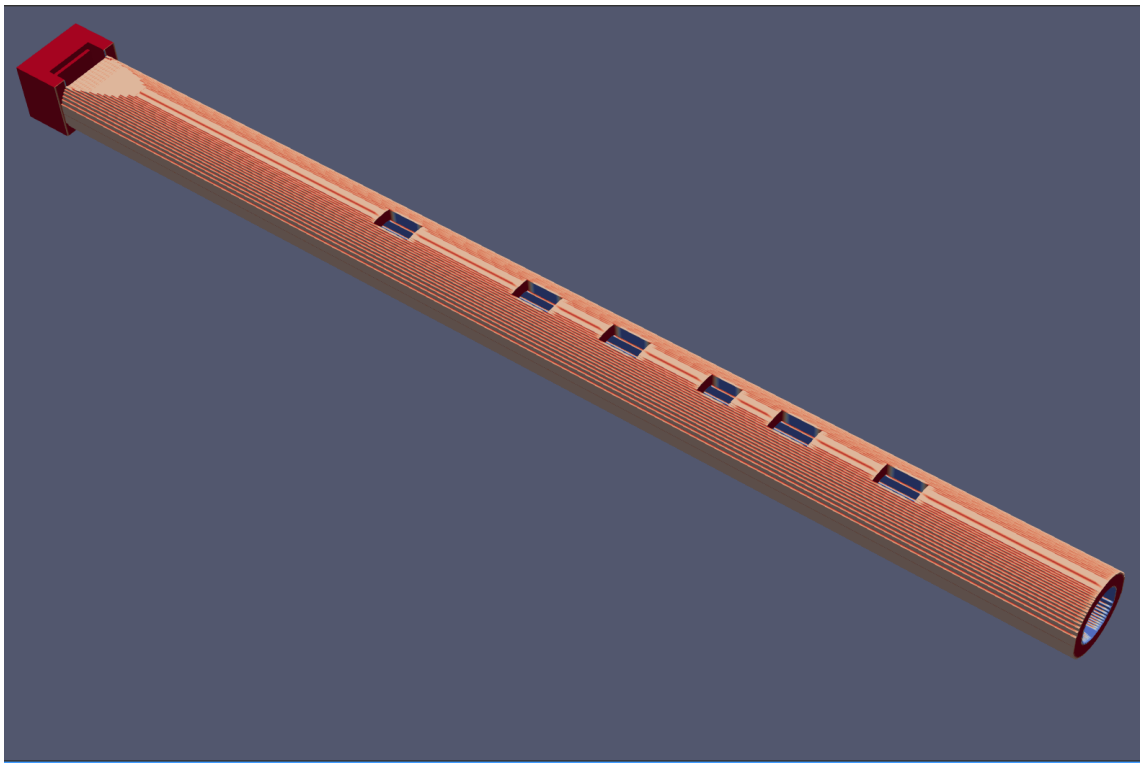

Figure 6.37: Simulated geometry of a soprano recorder illustrating the fingering for C6.

We begin this subsection with an analysis of the C6 at a blowing speed of 21 m/s and a ramp up time of 5 ms. The tone that the instrument produces can be found in figures 6.38a - 6.38b. Figure 6.38a displays 200 ms worth of tone while figure 6.38b displays 100 ms in order to better show the attack region. The correlogram and FFT constructed from the parameters just mentioned can be found in figures 6.39 - 6.40. From the correlogram in figure 6.39 we can observe how the spectral content varies with time. First we will analyze the steady state region of the tone which takes place approximately after 40 ms. Previously for the G5 at a ramp up time of 5 ms, we observed three potential spectral features present in the correlogram. In the correlogram in figure 6.39 for the C6 at a ramp up time of 5 ms we now observe *four* potential spectral features present in the tone. If we refer to the green FFT in figure 6.40 then we can see that two features with frequencies 1046 Hz and 560 Hz are actually present in the tone; the other two spectral features with frequencies less than 500 Hz (260 Hz and 303 Hz to be exact) appear to be artifacts. We now analyze the attack region of the tone which takes place between 0 ms to 40 ms. If we refer to the correlogram in figure 6.38a then we can observe the four spectral features present in the tone during this time interval. In this 40 ms timespan we can

observe that the frequencies associated with these four spectral features take time to 'settle in'. The frequencies of all these features tend to start from a slightly higher value and decrease to their true value. Referring to the correlogram in figure 6.40 we observe that *all four* of these spectral features are present in the black spectrum. As time progresses the lower frequency spectral content appears to decrease as is evident in the red sound spectrum in figure 6.40: the lower frequency content decreases in power while the power of the fundamental frequency (1046 Hz) and its octave increases. In summary, during the steady portion of the tone, the fundamental frequency (1046 Hz) dominates the spectrum. In addition, the octave ($\approx$2100 Hz) and an inharmonic feature with frequency 560 Hz is also present in the tone although they are about two orders of magnitude weaker than the fundamental mode; lower frequency content (less than 500 Hz) is not existent and appears to be an artifact. During the attack (less than 40 ms) portion of the tone we observe that *all four* spectral features are present in the sound spectrum during the first 40 ms, but the power of lower frequency content decreases in power as time progresses while the power of the fundamental mode of the C6 increases in power.

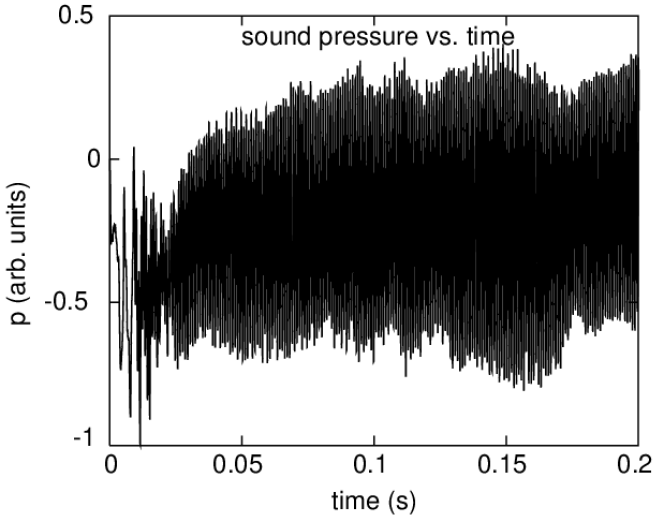

(a)

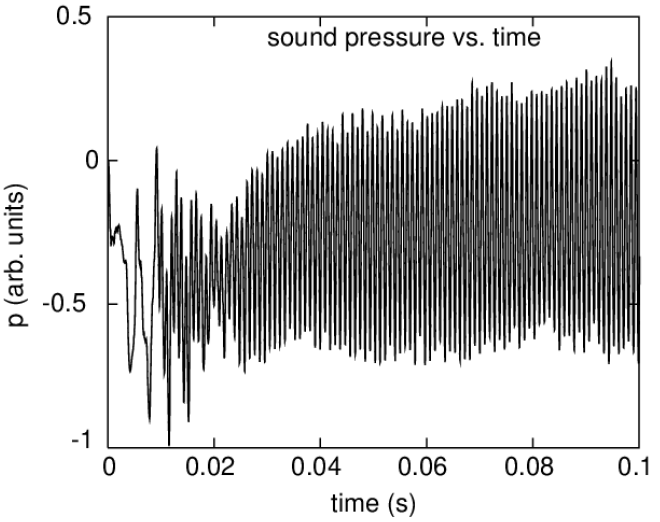

(b)

Figure 6.38: (a) ρ vs. time plot for C6 with a blowing speed of 21 m/s and a ramp up time of 5 ms. (b) ρ vs. time plot for C6 with a blowing speed of 21 m/s and a ramp up time of 5 ms. In this figure we only show the first 100 ms in order to give a good illustration of the attack portion of the tone.

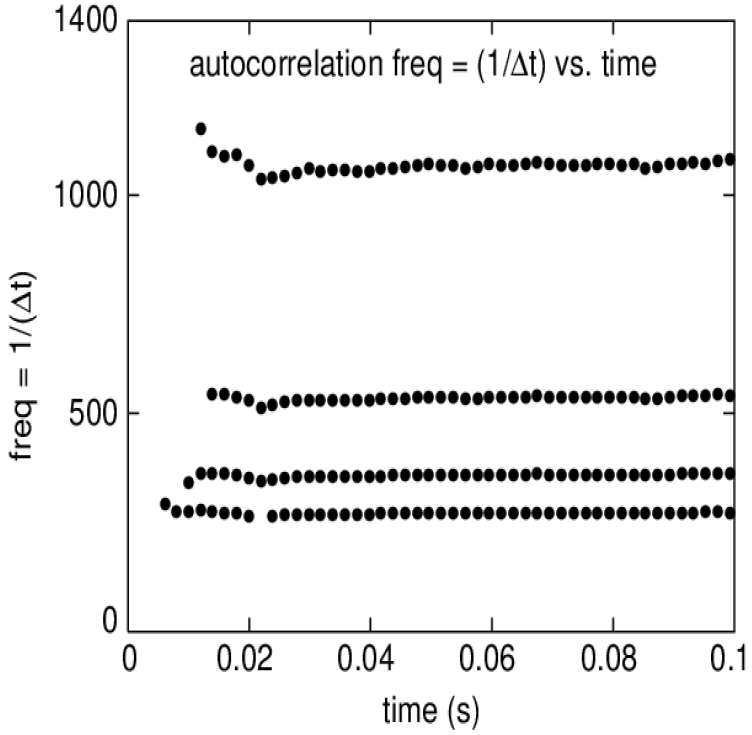

Figure 6.39: Correlogram for C6 with a blowing speed of 21 m/s, ramp up time of 5 ms. The window size is 4 ms and the starting time is at 2 ms.

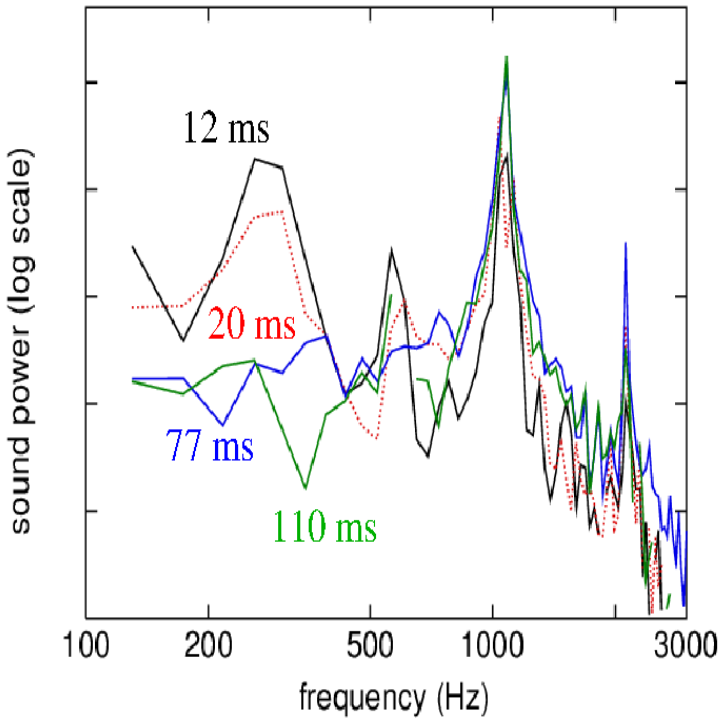

Figure 6.40: Sound spectrum for C6 with a blowing speed of 21 m/s, ramp up time of 5 ms. Each spectrum was calculated with an FFT using 23 ms from figure 6.38a and 6.38b. Each FFT was calculated using 23.5 ms of data with the following midpoints for different the different colored spectra black: 12 ms, red: 20ms, blue: 77 ms, green: 110 ms.

We conclude our spectral analysis with C6 at a blowing speed of 21 m/s and a ramp up time of 30 ms. The tone that the instrument produces can be found in figures 6.41a - 6.41b. Figure 6.41a displays 200 ms of tone while figure 6.41b displays 100 ms in order to better show the attack region. The correlogram and FFT for these particular parameters can be found in figures 6.42 - 6.43. Using the correlogram in figure 6.42 we can observe how the spectral content varies with time. First we will analyze the steady state portion of the tone which is approximately the first 50 ms. If we refer to the correlogram in figure 6.40 then we observe the presence of now *seven* possible frequencies present in the tone of the instrument. The values of each of these frequencies is approximately: 268 Hz, 313 Hz, 447 Hz, 581 Hz, 849 Hz, 1046 Hz, and 1118 Hz. If we now refer to the green sound spectrum in figure 6.40 we can see that *all* of these frequencies appear to be present within the system although the fundamental feature dominates the spectrum. This was a different story in the analyses of notes lower on the musical scale where inharmonic low frequency spectral content vanished in the steady state

region of the tone. We will now analyze the attack region of the tone which has duration from 0 ms - 50 ms. If we refer to the correlogram in figure 6.42 the first interesting behavior to note is that the tone appears to *not* have any periodicity in the first 20 ms. This cannot be directly be verified using the black sound spectrum in figure 6.43 since the region of time where this FFT was calculated extends greater than 20 ms. However, if we refer to attack region of the tone in figure 6.41b we can verify the lack of periodicity before 20 ms. If we next refer to the correlogram in figure 6.41b in the interval of time from 20 ms to 40 ms, we note the presence of seven possible frequencies again. If we refer to the red sound spectrum in figure 6.43 we can verify the presence of the spectral content with frequencies 260 Hz, 482 Hz, 570 Hz, 700 Hz, 790 Hz, 870 Hz, and 1046 Hz where the feature with frequency of 870 Hz dominates the spectrum in this interval of time. In summary, C6 with a slower ramp up time of 30 ms had the presence of many low frequency spectral features in both the attack and steady state regions. For C6 with a faster ramp up time (5 ms) only three low frequency features are present in the tone, and the octave of C6 (2093 Hz) is also more prominent (by about an order of magnitude) in the tone.

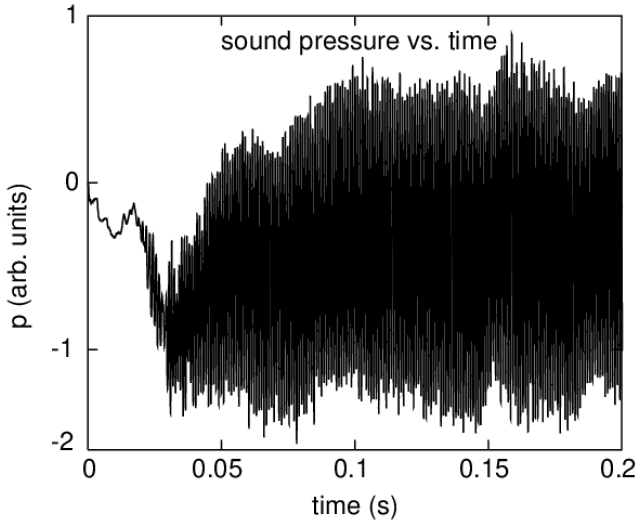

(a)

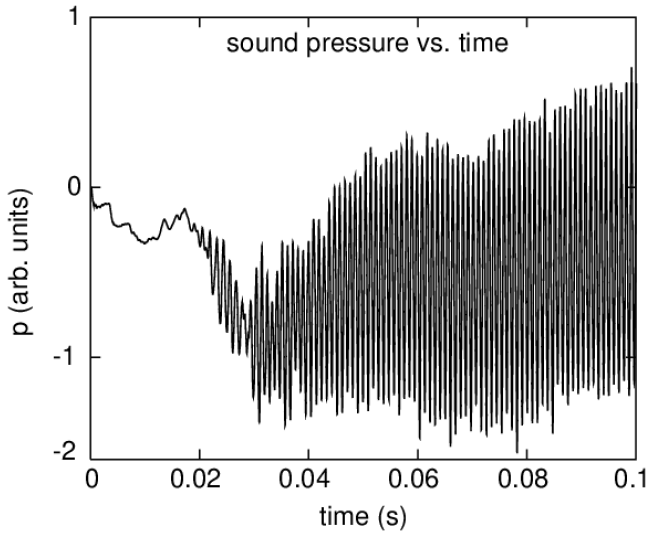

(b)

Figure 6.41: (a) ρ vs. time plot for C6 with a blowing speed of 21 m/s and a ramp up time of 30 ms. (b) ρ vs. time plot for C6 with a blowing speed of 21 m/s and a ramp up time of 30 ms. In this figure we only show the first 100 ms in order to give a good illustration of the attack portion of the tone.

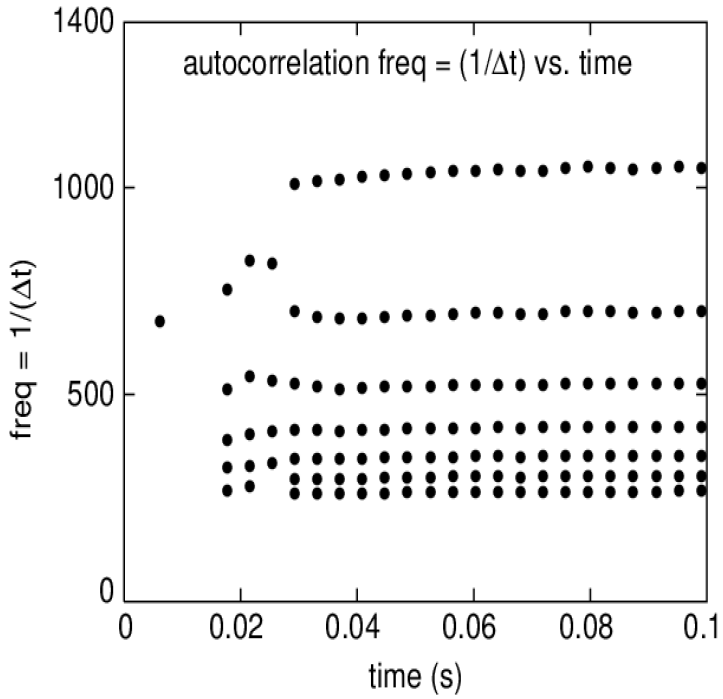

Figure 6.42: Correlogram for C6 with a blowing speed of 21 m/s, ramp up time of 30 ms. The window size is 4 ms and the starting time is at 2 ms.

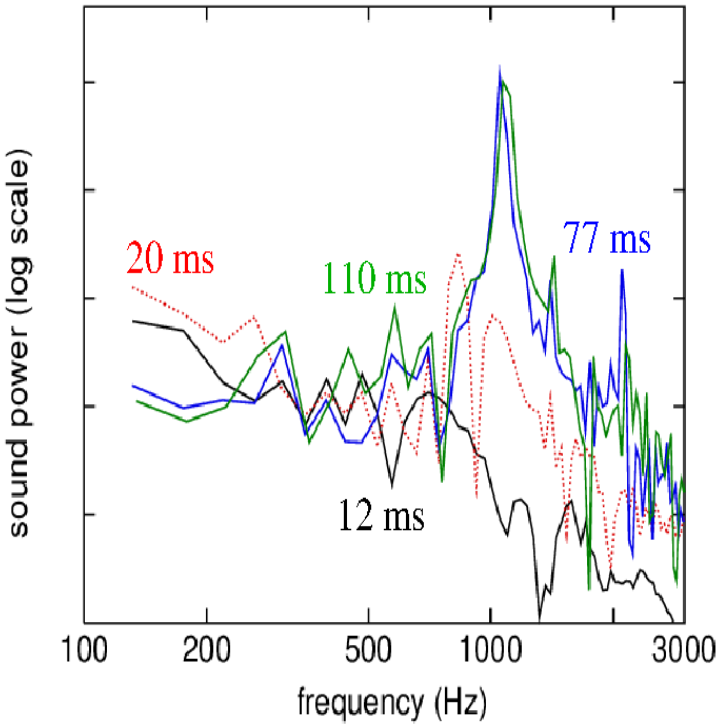

Figure 6.43: Sound spectrum for C6 with a blowing speed of 21 m/s, ramp up time of 30 ms. Each spectrum was calculated with an FFT using 23 ms from figure 6.41a and 6.41b. Each FFT was calculated using 23.5 ms of data with the following midpoints for different the different colored spectra black: 12 ms, red: 20ms, blue: 77 ms, green: 110 ms.

6.4 Summary of Results

In this section the results from section 6.3 are summarized and discussed. Furthermore, we divide the discussion into three different components: trends that are observed for different parameters, trends that are observed as we consider notes that are higher in scale, and lastly a discussion of edge tones.

We first discuss observations about the attack and steady state portions of the tone when comparing differences in parameters, i.e, different blowing speeds or ramp up times for a given note. One general trend during the attack transient is that longer ramp up times produce tones that have strong broadband spectral content that are the result of a slow increase to the harmonic frequencies of the resonator. We will elaborate more on the possible origins of these types of frequencies later in this section. A good example of this type of behavior can be seen by comparing the correlograms and spectra in figures 6.18-6.19 and 6.21-6.22. In figure 6.21

between 4 ms to 30 ms we see a slow increase to the fundamental frequency of 520 Hz whereas in figure 6.18 this behavior is not seen. This slow increase in frequency to the fundamental mode results in the broadband frequency centered near 260 Hz in the black spectrum in figure 6.22. Another interesting behavior that happens during the attack portion of the tone is that faster ramp up times tend to introduce stronger harmonic high frequency spectral content. A good illustration of this type of behavior can be seen by comparing the early sound spectra shown in black in figures 6.26 and 6.29. In figure 6.26 the peak near frequency 1318 Hz is weaker in power by about an order of magnitude than the peak near 659 Hz. In contrast, in figure 6.29 those same peaks have about two orders of magnitude difference.

We next consider how the attack portion of the tone changes when we ascend to higher notes. The main effect that is observed is the introduction of more inharmonic spectral features into the spectrum. A good illustration of this behavior can be seen by comparing the correlograms and the early black and red sound spectra in figures 6.21-6.22 and 6.42-6.43. In the black sound spectrum in figure 6.22 there is primarily one dominant broadband frequency centered at 260 Hz, however in the black spectrum in figure 6.43 there are four additional inharmonic spectral features present; this can be seen more clearly by comparing the correlograms in figure 6.21 and 6.42. This effect is even more dramatic when we compare the red spectra in the same figure. In the red spectrum in figure 6.22 there is one dominant broadband peak near 520 Hz whereas in the red spectrum in figure 6.43 there are as many as seven inharmonic peaks now present in the spectrum.

Finally, we provide a possible explanation for the existence of the inharmonic spectral content and one hypothesis is that they involve *edgetones*. An edgetone is the sound produced by an air jet interacting with a wedge or often a sharp *edge* [38, 39]. Using the context of the recorder, an edgetone is produced from the interaction of the air jet and the labium. Many theories have been presented on the mechanism of the edgetone and it is has been the subject of much controversy since its discovery. It is well agreed upon in the literature that the frequency of the edgetone is dependent on the exit velocity of the air jet and the window or the distance from the channel to the labium [38,40]. For the air jet velocity and window length in a recorder, the edgetone frequency would be in the range of a few hundred hertz [41, 42]. In addition, we

expect nonlinear interactions between the edgetones and the resonator harmonics; this could conceivably give new modes lower in frequency than the resonator harmonics that would not be expected in a linear system. This would explain the presence of inharmonic spectral content in each note as well as the presence of more inharmonic content for notes that were produced with higher blowing velocities. One way to test this hypothesis is to change the length of the window w and observe how the frequency of the inharmonic components change. This will be the subject of exciting future studies.

Chapter 7

Modeling a Clarinet Reed

In the last fifty-nine years, several computational models of the clarinet have been explored and compared with experiments. Each model has a varying degree of detail in how each distinct element of the clarinet is treated, however, the clarinet *reed* is the focus of this chapter. In 1963 Backus [43] constructed an idealized model of the clarinet in which the reed is modeled as a single-degree-of-freedom oscillator where the reed *aperture* is driven by the pressure difference between the players mouth and the mouthpiece of the clarinet. There were several more models presented since Backus' paper in 1963 [44], but a recent example of a single-degree-of-freendom model of the clarinet reed was presented in 2003 by Dalmont et al [45]. In Dalmont's study, the reed was modeled as a single-degree-of-freedom oscillator that describes the dynamics of the reed *tip* that is driven by the pressure difference. These are not the only single-degree-of-freedom models of the reed, but they are typical.

Lumped element approximations, such as the ones just discussed, perform well at describing certain behaviors such as the presence of a threshold blowing pressured needed in order for the instrument to produce sound. *However*, there are some physical characteristics of the clarinet that cannot be explored unless a *distributed* model of the reed is adopted. For example, how does the reed thickness affect the behavior of the clarinet? This question cannot be explored unless the reed is modeled as a vibrating bar whose equation of motion is given by the Euler-beam equation [46].

Stewart and Strong [44] were among the first to implement a distributed model for the reed. This was state-of-the-art early work that modeled the complete clarinet instrument. With supercomputers such as Easley at Auburn University, we can improve the flow and pressure

calculations that are part of a full clarinet model, but the reed calculation presented by Stewart and Strong is still state-of-the-art to this day. Stewart's [44] lumped model demonstrated key behaviors that are found in a real clarinet including self-sustaining oscillations and threshold blowing pressures. Stewart and Strong solved for the motion of the reed by using both an *explicit* and an *implicit* finite-difference method. The advantages that *implicit* methods have over *explicit* methods have already been discussed in chapter 2; Stewart and Strong chose to implement the *implicit* implementation for their calculation due to those reasons.

Approximately two decades later Avanzini and van Walstijn [3] studied an even more complete model of the reed motion by adding more realistic reed/mouthpiece interaction forces. For the remainder of this thesis, AW [3] will be used to reference Avanzini and van Walstijn's work. The additions to the reed model of Stewart and Strong that AW made are that (1) the reed is clamped to a mouthpiece and behaves as a cantilever beam and (2) is contact with a (player's) lip. The equation used to model the reed *and* the numerical method used to solve for its motion is the same as in Stewart and Strong, however, the motion of the reed was solved for using a highly stable and accurate implicit finite-difference scheme called the implicit-θ method. In this chapter a distributed model for a clarinet reed is surveyed in addition to the implicit numerical method that AW (and Stewart/Strong) used for their model. The code used to simulate the reed motion was then added into the code for a model of the clarinet written by N. Giordano [30].

The reed of a clarinet can be modeled as a vibrating bar with length L, uniform width w, and nonuniform thickness $b(x)$. One end is clamped at $x = 0$ with the free end at $x = L$ as can be seen in Figure 7.1. The reed will be assumed to be constrained to move in only one-dimension, that is, it is assumed that only one-dimensional flexural waves with displacement along y are present in the reed. Torsional modes will not be accounted for here because the expected frequencies of the sound from the clarinet are significantly lower than the frequencies of any torsional vibrations. Furthermore, it is assumed that the reed is made of a homogeneous material which implies that the density ρ and Young's modulus Y are uniform. The motion of a simple uniform reed undergoing flexural vibrations is described by [3, 47],

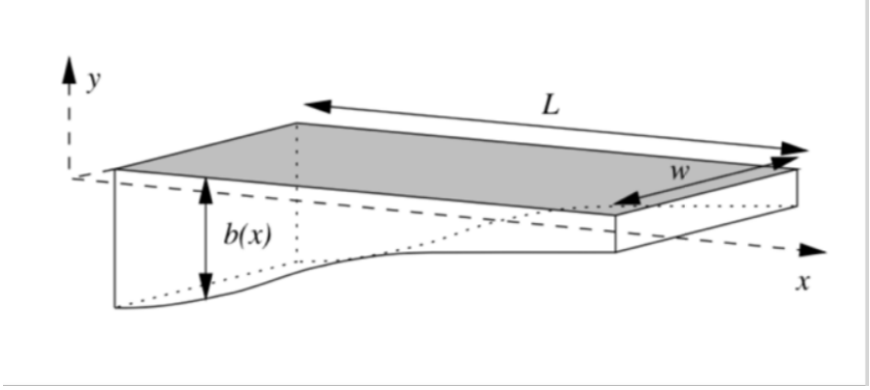

Figure 7.1: Diagram of a nonuniform beam/reed. Diagram is from AW [3].

$$IY\frac{\partial^4 y}{\partial x^4} = -\rho S\frac{\partial^2 y}{\partial t^2}, \tag{7.1}$$

where I is the moment of inertia, S is the cross-sectional area, y is the displacement from equilibrium, x is the position along the length of the reed, and t is time. This fourth-order partial differential equation provides a model for a vibrating reed for which there are no external or damping forces present. The equation of motion must be extended to include external and damping forces and a non-uniform thickness. The equation of motion then becomes [3, 47],

$$\frac{\partial^2}{\partial x^2}\left[YI(x)\left(1+\eta\frac{\partial}{\partial t}\right)\frac{\partial^2 y}{\partial x^2}\right] + \rho S(x)\frac{\partial^2 y}{\partial t^2} = F(x,t), \tag{7.2}$$

where $I(x)$ and $S(x)$ are now functions of x, $F(x,t)$ is the total external force on the reed, and η is the magnitude of viscoelastic losses internal to the reed. The moment of inertia is now a function of the cross-sectional area $S(x)$ and the radius of gyration $R_g(x)$, i.e, $I(x) = S(x)R_g^2(x)$. Assuming that the width, w, of the reed is constant and the thickness, $b(x)$, is nonuniform, $S(x)$ becomes $S(x) = wb(x)$. Under the assumption that the width, w, is uniform, the radius of gyration is $R_g^2(x) = b(x)/12$. The boundary conditions associated with a vibrating cantilevered reed that is clamped at $x = 0$ and free to move at $x = L$ are,

$$y(0,t) = \frac{\partial y}{\partial x}(0,t) = 0, \tag{7.3}$$

and

$$\frac{\partial^2 y}{\partial x^2}(L,t) = \frac{\partial^3 y}{\partial x^3}(L,t) = 0\ . \tag{7.4}$$

Equations 7.2 - 7.4 provide a sufficient model for a clarinet reed with multiple external forces such as the damping from the players lips, and the pressure of the surrounding air contained in $F(x,t)$ in equation 7.2.

7.1 Implicit Theta Method

In chapter 2, the advantages and disadvantages of explicit and implicit finite difference methods for solving PDE were compared. The largest advantage of explicit methods is the ease of implementation that comes with the sacrifice of longer runtimes due to increased resolution, especially in the time domain. This is the result of explicit methods being unstable for resolutions that *do not* satisfy the *Courant* condition. However, implicit methods have the advantage in that they are *unconditionally* stable; any combination of spatial and time resolution may be used given that they provide enough accuracy for the problem being solved. This is especially important in dispersive systems, such as the reed, since high frequencies can demand high and therefore limiting resolutions. For this reason, the *implicit-θ* method used in AW [3] and Stewart and Strong [44] was used to solve for the motion of the reed in Giordano and Thacker [30] and in this thesis.

In this section, the *implicit-θ* method is surveyed. We begin by rewriting equation 7.1 by rearranging terms,

$$Y\frac{\partial^2}{\partial x^2}\left[I(x)\frac{\partial^2 y}{\partial x^2}\right] + \eta Y\frac{\partial^2}{\partial x^2}\left[I(x)\frac{\partial^3 y}{\partial x^2 \partial t}\right] + \rho S(x)\left[\frac{\partial^2 y}{\partial t^2}\right] = F(x,t)\ . \tag{7.5}$$

First- and second-order derivatives will be approximated as second-order accurate centered differences

$$\frac{\partial y}{\partial t}(x_j,t_i) \approx \frac{y_j^{i+1} - y_j^{i-1}}{2t_s} \tag{7.6}$$

$$\frac{\partial^2 y}{\partial t^2}(x_j,t_i) \approx \frac{y_j^{i+1} - 2y_j^{n} + y_j^{i-1}}{t_s^2} \tag{7.7}$$

We will now define a discrete operator, δ_x^2, that approximates the second spatial derivative

$$\frac{\partial^2 y}{\partial x^2}(x_j, t_i) \approx \delta^2 y = \frac{y_{i+1}^i - 2y_i^i + y_{i-1}^j}{x_s^2} \tag{7.8}$$

The first term on the left-hand side of equation 7.5 will be approximated as [3],

$$\frac{\partial^2}{\partial x^2}[I(x)\frac{\partial^2 y}{\partial x^2}](x_j, t_i) \approx (1-2\theta)\delta_x^2[I(\delta_x^2 y)]_j^i + \theta\left(\delta_x^2[I(\delta_x^2 y)]_j^{i+1} + \delta_x^2[I(\delta_x^2 y)_j^{i-1}]\right), \tag{7.9}$$

where $0 \leq \theta \leq 1$ is a parameter that is used to impart a time-smoothing effect on the spatial derviatives [3]. Equation 7.9 is known as an implict θ-scheme, and for $\frac{1}{4} \leq \theta \leq 1$ the θ-scheme is unconditionally stable for any x_s and t_s and can be adjusted for accuracy. Chaigne [47] found, and AW [3] confirmed, that $\theta = \frac{1}{4}$ gives the most accurate predictions for the frequencies of a uniform bar, which have analytical solutions. For this reason, $\theta = \frac{1}{4}$ will be used through all simulations presented in this chapter. Each $\delta_x^2\left[I(\delta_x^2 y)\right]_j^i$ term can be written as [3]

$$\delta_x^2\left[I(\delta_x^2 y)\right]_j^i = \frac{I_{j+1}y_{j+2}^i - 2(I_{j+1}+I_j)y_{j+1}^i}{x_s^4} + \frac{(I_{j+1}+4I_j+I_{j-1})y_j^i}{x_s^4} + \frac{I_{j-1}y_{j-2}^i - 2(I_j+I_{j-1})y_{j-1}^i}{x_s^4}. \tag{7.10}$$

The middle term on the left-hand side of the equality of equation 7.5 will be approximated as [3]

$$\frac{\partial^2}{\partial x^2}\left[I\frac{\partial^3 y}{\partial^2 \partial t}\right] \approx \theta f_s\left(\delta_x^2[I(\delta_x^2 y)]_j^{i+1} - \delta_x^2[I(\delta_x^2 y)]_j^{i-1}\right). \tag{7.11}$$

Lastly, the discretized boundary conditions from equations 7.3 - 7.4 are given as [3],

$$\begin{aligned} y_0^i = 0,\ y_{-1}^i = y_1^i, \\ y_{N+1}^i = 2y_N^i - y_{N-1}^i, \\ y_{N+2}^i = y_N^i - 4y_{N-1}^i + y_{N-2}^i. \end{aligned} \tag{7.12}$$

In order to solve the resulting matrix equations that inevitably follow from the θ-implicit discretization of equation 7.5, an efficient LU-decomposition [24] can be used to decompose the

upper and lower matrix which can then be used to solve for the proceeding time-step of the displacement of the reed y_j^{i+1}.

7.2 Simulations

Thus far we have surveyed the history on clarinet modeling and have focused on the on modeling of the *clarinet reed*. In addition, we have discussed the equation that will be used to model the motion of the clarinet reed, namely the Euler-Bernoulli beam equation. Lastly, the numerical method used to solve for the motion of the reed, the *implicit-θ* method, has been presented and discussed. In the sections that follow, the simulation of the standalone reed is tested and validated. In addition, the full model of the clarinet will be briefly discussed.

In this section the parameters and results of the Euler-beam simulations using the implicit-θ method are explored. The set of parameters discussed is taken directly from AW [3] to assure the fidelity of the simulations. The parameters used in AW are provided in table 7.1.

Name	Value
Length	$L = 34 \times 10^{-3}$m
Width	$w = 13 \times 10^{-3}$m
Viscoelastic constant	$\eta = 6.0 \times 10^{-7}$s
Fluid damping coefficient	$\gamma = 100$Hz
Young's modululs	$Y = 5.6 \times 10^{9}$N/m^2
Density	$\rho = 500$kg/m^3
Driving frequency	$f = 223$Hz

Table 7.1: The Avanzini parameter set

Furthermore, in the AW study a spatial mesh of $x_s = 1.7 \times 10^{-4}$ m and a time-step of $t_s = 5.0 \times 10^{-6}$ s. With the parameters provided in 7.1, the time-step, and spatial mesh, and the absence of an external force, Avanzini reported a fundamental frequency of $\omega_0 = 1405$ Hz. Using the same parameters as Avanzini, my implementation of the implicit theta method to approximately solve equation 7.5 gave a fundamental frequency of $\omega_0 = 1404$ Hz. In addition to the frequency, the "displacement vs time" plot is given as well. Given the parameters listed in 7.1, one expects the system to be underdamped. As can be seen from figure 7.2, the reed-system clearly displays underdamped oscillations since the amplitude of oscillations decrease exponentially. These

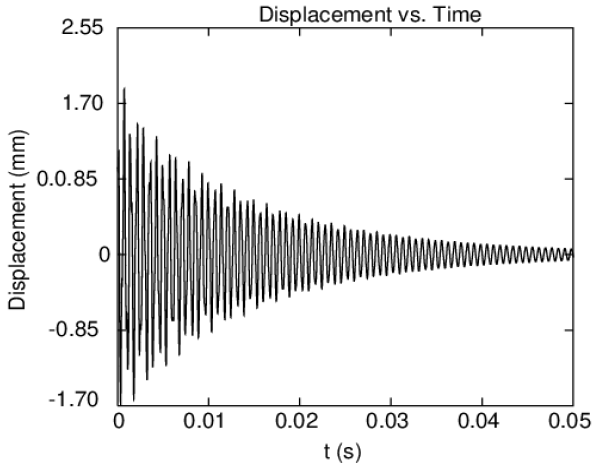

Figure 7.2: Displacement vs time plot for Avanzini parameter set

results should assure the reader that the simulation is working and converging to a physically realizable solution when the reed is damped and absent of any external forces. In the clarinet simulations performed by Giordano and Thacker, an external force from the surrounding air as calculated using solutions of the NSE was introduced into the system.

To check that the simulation for the reed is still convergent in the presence of an external force, a sinusoidal external force per unit length was introduced into the reed-system with the form,

$$(F_{ext})^n = A_{min} + \left(\frac{A_{max} - A_{min}}{2}\right)(1 + \sin(2\pi f n t_s + \phi_0)), \tag{7.13}$$

where n is the time step, and A_{min} and A_{max} are the minimum and maximum amplitudes. This external force per unit length is uniform and is imparted to every lattice point on the reed. Once the external force has been introduced, one can expect additional harmonics introduced into the early portion of the motion due to damped undriven transients that have not yet decayed. In addition, the steady-state oscillations should contain only one frequency, i.e, the frequency of the sinusoidal external force, which for the AW [3] parameter set, is $f = 223$ Hz and can be found in table 7.1; this driving frequency is a typical frequency produced by instruments in the clarinet family. These results are given in figures 7.4 and 7.5. With the combined results of figures 7.2-7.5 the fidelity of the reed simulations are confirmed.

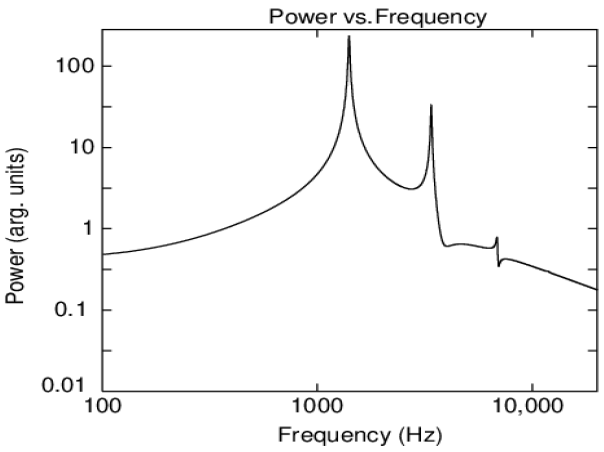

Figure 7.3: Fourier transform for Avanzini parameter set. The frequency corresponding the largest power is 1405 Hz.

7.3 Conclusion

In the introduction of this chapter, the fundamental equation responsible for the vibrations of a uniform/nonuniform reed have been given and surveyed. The motivation for using finite-difference methods for this chapter is to approximate solutions to the Euler-beam equation in order to model the motion of a nonuniform reed in a clarinet, i.e, use a distributed model for the reed. In section 7.2 the parameter set that was used by AW [3] is given in table 7.1. The frequency produced by the AW simulations is given and matches well with the frequency produced by the simulations that are used in this thesis. In addition, the simulations in this thesis demonstrate both damped- and driven-motion when in the absence and presence of an external force. Based on these results, the fidelity of the reed simulations in this thesis was confirmed.

The purpose of the reed simulation work presented in this chapter was for use in a large distributed simulation of a clarinet constructed by N. Giordano [48, 30]. The implicit-θ method presented in section 7.1 allowed the use of a smaller mesh, x_s, in the spatial dimension while the time-step t_s can remain invariant since the implicit-θ method is unconditionally stable for any x_s and t_s as long as $1/4 \leq \theta \leq 1$.

As stated before, the purpose of using this model of the reed is to use it as part of a fully functional clarinet model that utilized the NSE [30]. The geometry of this model of the clarinet

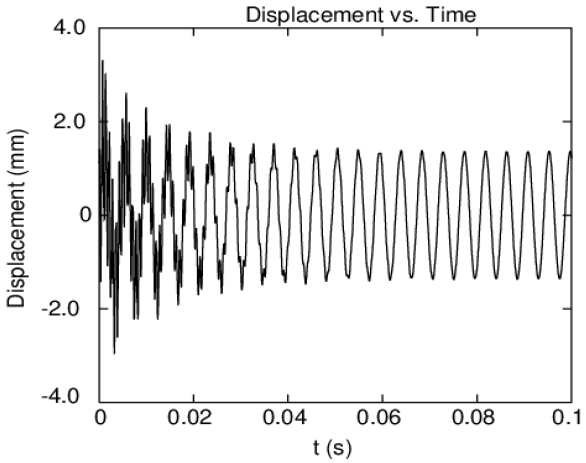

Figure 7.4: Displacement vs time plot for the Avanzini parameter set with an additional external force added to the system

was smaller than a real clarinet in order to keep the numerical modeling feasible. The clarinet is a complex instrument to model because there are many working parts in the model: (1) the dynamics of the reed need to be modeled, (2) collisions with the mouthpiece and the reed need to be accounted for and (3) the interaction of the reed and the players lips must be included. These three things were accounted for in addition to modeling the airflow in the resonator of the clarinet [30].

This clarinet model [30] was the first study to (1) use the NSE to model the airflow in the resonator in the recorder, (2) study the effect of varying the geometry of the mouthpiece, (3) alter the physical properties and dimensions of the reed, (4) vary the detailed geometry of the mouth and (5) vary the position of the reed at which it contacts the lips of the player and incorporate lip damping. This model of the clarinet was a study of many firsts and the modeling of the reed was an integral part of it. Full details are given in [30].

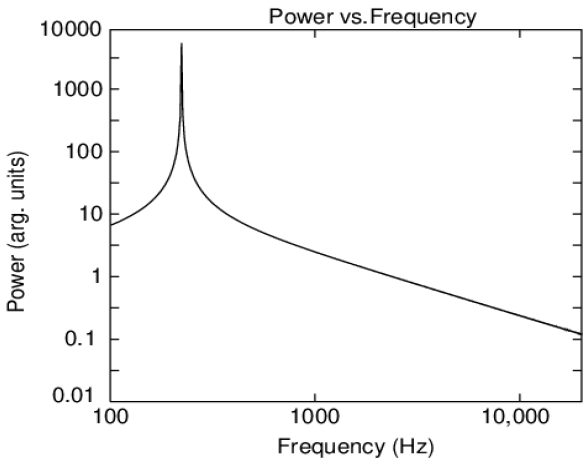

Figure 7.5: Fourier transform for Avanzini parameter set with an external force added to the reed-system. The frequency corresponding the peak is 223 Hz.

Chapter 8

Summary and Conclusion

In this thesis we have studied musical wind instruments using a set of fundamental set of equations from physics known as the Navier-Stokes Equations. In the past, studying instruments using this technique was not feasible due to the lack of computing resources that have only been available recently. Our group focuses on the study and simulation of win instruments. Specifically our group has studied the recorder, clarinet, trumpet, piccolo, and piano. This thesis was dedicated to solely studying various physical behaviors of the recorder and the clarinet.

Chapter 1 motivated the study of musical instruments and gave various early acoustics studies by people such Duhamel, Helmholtz, and Raman. In addition, a brief history of the literature on the simulation of wind instruments was discussed. We found that models of such instruments can be categorized into *lumped* or *distributed* models and emphasized that this thesis will focus on distributed models. This thesis emphasizes distributed models because certain physical characteristics of the instrument can only be studied using this type of model. For example, only using a distributed model can we study the effects that small alterations to recorder geometry have on the physical behavior of the instrument.

In chapter 2 the numerical methods that will be used to numerically solve the NSE were explained in detail. This chapter included exposition on the Navier-Stokes equations, implicit and explicit finite difference methods, and the implementation details of the simulations. Specifically, the form of the NSE that were numerically solved were given as well as the assumptions that lead to that form. The MacCormack predictor-corrector was detailed; this method is *the* algorithm used in the recorder simulations in chapter 3. Lastly, how the simulations were implemented was briefly discussed in the last section of chapter 2.

Chapter 3 introduced the phenomena of *regime change* and its prevalence among the recorder family - particularly in recorders of lower register. Specifically, *bass* recorders suffer from regime change that limits a players ability to play the note that represents the instrument's fundamental mode at a moderate to loud volume. This can be issue for players who might need to play and hold this note at such volume. Additionally, the hypothesis as to why this issue is present in the bass recorder was discussed. Using this hypothesis, recorder geometries were constructed that are significantly smaller in scale but displayed the regime change characteristics of both the sopranino and bass recorders - these two model geometries were called the sopranino - style and bass - style recorders. The airflow of both of these recorders were then studied and it was found that introducing a trench beneath the labium of the recorder increases the playing range of the fundamental note on the bass - style recorder. This bass - style recorder that has a trench beneath the labium was called the *modified bass-style reocrder*.

Chapter 4 introduced the experiment and physical copies of the sopranino - style bass - style, and modified bass - style recorders that were used to validate the simuations of chapter 3. The dimensions of both the sopranino - style and bass - style recorders were given and also how they can be made in the AutoCAD software. In addition, a brief survey of 3D printing was given and the largest source of uncertainty in the experiment was discussed.

Chapter 5 detailed the setup of the experiment and the results. It was found that the experiment on the sopranino - style, bass - style, and modified bass - style recorders were in experimental agreement. These results showed that the modifications to the geometry of the bass - style recorder successfully increased the playing range of the note that represents this instrument's fundamental mode. In addition, it is strong evidence that NSE modeling can be used successfully to improve the design of wind instruments and supports the modeling conducted in other studies that make use of the NSE.

Chapter 6 studied the effects that the player's blowing profile has on the tone of a full sized recorder, namely, a recorder that was modeled on a Yamaha YRS-23 soprano recorder. To motivate the approach taken in our analysis, section 6.1 explained the shortcomings of using the FFT for spectral analysis of a time dependent signal and why the correlogram provides a way to visualize such signals that are complementary to the FFT. In addition, section 6.2

detailed the recorder geometry that was used in the simulations and is based on the Yamaha YRS-23 soprano recorder. Lastly, sections 6.3 and 6.4 detailed the results of the analysis for four different notes.

In chapter 7, a distributed model of a clarinet *reed* was explained in detail. Previous models of the clarinet have mixed distributed and lumped modeling in order to study this instrument. However, this model of the reed will be included in a model of the clarinet that is completely *distributed*. Specifically, the reed was modeled as an Euler-beam which is a fourth order partial differential equation. The implicit - θ method was used to solve the Euler-beam equation and its details were given in this chapter. The results of several simulations were given in order to validate that this implementation of the reed model was correct. This algorithm for the reed was then used with NSE code from our group that produced a full first principles model of the clarinet [30].

This thesis used first principles simulations that were based on the NSE to study the recorder and certain aspects of the clarinet. These simulations were not only used to study certain physical phenomena of the recorder, but to also improve its design. Recorders that were small in scale were studied in chapter 3 - 5, however, in chapter 6 a full sized recorder that was based on a soprano Yamaha recorder was studied. Studies such as these were only possible with the rise of advanced computing power that have become recently become available and I anticipate *many more* studies that utilize first principles physics in the future.

References

[1] Nicholas S. Lander. *Recorder Home Page: History: Medeival Period*, 2020.

[2] Svante Granqvist and Britta Hammarberg. The correlogram: A visual display of periodicity. *Journal of the Acoustical Society of America*, 114(5):2934–2945, November 2003.

[3] Frederico Avanzini and Maarten Van Walstijn. Modelling the mechanical response of the reed-mouthpiece-lip system of a clarinet. part 1. a one-dimensional distributed model. *Acta Acustica United with Acustica*, 90, 2004.

[4] Lumen Learning. Pythagoras: Musical investigations and theories.

[5] Neville H. Fletcher and Thosmas D. Rossing. *The Physics of Musical Instruments*. Spring-Verlag New York Inc, 1991.

[6] C. V. Raman. Experiments with mechanically-played violins. *Proceeding of the Indian Asscociation for the Cultivation of Science*, 6, 1920.

[7] Harry F. Olson. *Frederick Albert Saunders*. National Academy of Sciences, 1967.

[8] N. Giordano and M. Jiang. Physical modeling of the piano. *EURASIP Journal on Advances in Signal Processing*, 7, 2004.

[9] Iran Sanadzadeh and Angela K. Coaldrake. Heuristic finite element models of the japanese koto. *Journal of the Acoustical Society of America*, 144, 2016.

[10] E. Becache, A. Chaigne, G. Derveaux, and P. Joly. Numerical simulation of a guitar. *Computer and Structures*, 83, 2005.

[11] N. Giordano. Computational study of the piccolo: Evidence of chaotic tones. *Journal of the Acoustical Society of America*, 140, 2016.

[12] N. Giordano. Physical modeling of a conical lip reed instrument. *Journal of the Acoustical Society of America*, 143, 2018.

[13] Howard C. hardy and James E. Ancell. Comparison of the acoustic performance of calf-skin and plastic drum head. *Journal of the Acoustical Society of America*, 30, 1958.

[14] Panayotis A. Skordos. *Modeling flue pipes: Subsonic flow, lattice Boltzmann, and parallel distributed computers*. PhD thesis, Massachusetts Institute of Technology, 1995.

[15] H. Kühnelt. Simulating the mechanism of sound generation in flutes using the lattice boltzmann method. *Proceedings of the Stockholm Music Acoustics Conference (SMAC)*, SMAC 03, 1995.

[16] H. Kühnelt. Simulating the mechanism of sound generation in flutes and flue pipes with the lattice-boltzmann-method. *International Symposium on Musical Acoustics*, SMAC 03:251–254, 2004.

[17] H. Kühnelt. Simulation and analysis of the flow-acoustic interactions in the mouth of flute-like instruments. *Forum Acusticum (European Conference on Acoustics)*, pages 1–6, 2005.

[18] R. T. Schumacher. Self-sustained oscillations of the clarinet: An integral equation approach. *Acta Acustica*, 40, 1978.

[19] R. T. Schumacher. Self-sustained oscillations of the organ flue pipe: An integral equation approach. *Acta Acustica*, 39, 1978.

[20] Y. Obikane. Computational aeroacoustics on a small flute using a direct simulation. *Computational Fluid Dynamics*, pages 435–441, 2010.

[21] Massachussetts Institute of Technology. *Comparison between subsonic flow simulation and physical measurements of flue pipes*, Dourdan, France, 1995.

[22] N. Giordano. Simulation studies of a recorder in three dimensions. *Journal of the Acoustical Society of America*, 135, 2014.

[23] N. Giordano. Direct numerical simulation of a recorder. *Journal of the Acoustical Society of America*, 133, 2013.

[24] William T. Vetterling William H. Press, Saul A. Teukolsky and Brian P. Flannery. *Numerical Recipes: The Art of Scientific Computing*. Cambridge University Press, 2007.

[25] Robert W. MacCormack. The effect of viscosity in hypervelocity of impact cratering. *American Institute of Aeronautics and Astronautics*, 69-354, 1969.

[26] Rossing Giordano. personal communication.

[27] Francois Blanc, Benoit Fabre, Nicolas Montgermont, Patricio De La Cuadra, and Andrea Almeida. Scaling of flute-like instruments: An analysis from the point of view of the hydrodynamic instability of the jet. *Acta Acustica*, 96, 2010.

[28] J. Martin. *The Acoustics of the Recorder*. Moeck, 1993.

[29] D. J. Acheson. *Elementary Fluid Dynamics*. Clarendon Press, 1 edition, August 1990.

[30] N. Giordano and J.W. Thacker. Navier-stokes-based model of the clarinet. *Journal of the Acoustical Society of America*, 148:3827–3835, December 2020.

[31] International Symposium on Musical Acoustics. *Experimental study of attack transients in flute-llike instruments*, Le Mans, France, July 2014.

[32] Irwin Pollack. Number of pulses required for minimal pitch. *Journal of the Acoustical Society of America*, 42:895, June 1967.

[33] P. J. Metters and R. P. Williams. Experiments on tonal residues of short duration. *Journal of Sound and Vibration*, 26(3):432–436, October 1973.

[34] Mattson Ogg, L. Robert Slevc, and William J. Idsardi. The time course of sound cateogry identification: Insights from acoustic features. *Journal of the Acoustical Society of America*, 142(6):3459–3473, December 2017.

[35] R. Klinke and R. Hartmann, editors. *Threshold duration for melodic pitch*, 15 Chaucer Road, Cambridge CB2 2EF, 1983. International Symposium on Hearing, Springer-Verlag.

[36] Ronald N. Bracewell. *The Fourier Transform and Its Applications*. McGraw-Hill, third edition edition, June 1999.

[37] Robert H. Shumway and David S. Stoffer. *Time series analysis and its applications: with R examples*. Statistics. Springer, 233 Spring Street, New York, NY 10013, third edition, 2011.

[38] Alan Powell. On the edgetone. *Journal of the Acoustical Society of America*, 33:395–409, April 1961.

[39] C. Segoufin, B. Fabre, and M. P. Verge. Experimental study of the influence of the mouth geometry on sound production in a recorder-like instrument: Windway length and chamfers. *Acta Acustica*, 86:649–661, January 2000.

[40] Istvan Vaik, Roxana Varga, and Gyorgy Paal. Frequency and phase characteristics of the edge tone. *Periodica Polytechnica Mechanical Engineering*, 58(1):55–67, September 2013.

[41] N. S. Dougherty, B. L. Liu, and J. M. O'Farrell. Numerical simulation of the edge tone phenomenon. Technical report, National Aeronautics and Space Administration, 1994.

[42] C. Segoufin and B. Fabre. Experimental investigation of the flue channel geometry influence on edge-tone oscillations. *Acta Acustica United with Acustica*, pages 966–975, March 2004.

[43] John Backus. Small-vibration theory of the clarinet. *Journal of the Acoustical Society of America*, 35(3):305 – 313, March 1963.

[44] Stephen E. Stewart and William J. Strong. Functional model of a simplified clarinet. *Journal of the Acoustical Society of America*, 68, 1980.

[45] Jean-Pierre Dalmont, Joel Gilbert, and Sebastian Ollivier. Nonlinear characteristics of single-reed instruments: Quasistatic volume flow and reed opening measurements. *Journal of the Acoustical Society of America*, 114:2253–2262, October 2003.

[46] Stephen Timoshenko. *History of Strength of Materials*. Dover Publications, reprint of 1st edition edition, 1953.

[47] Antoine Chaigne and Vincent Doutaut. Numerical simulations of xylophones. 1. time-domain modeling of the vibrating bars. *Journal of the Acoustical Society of America*, 101, 1997.

[48] Nicholas Giordano and Jared Thacker. Navier-stokes-based modeling of the clarinet. *Proceedings of the International Symposium on Musical Acoustics*, pages 367–370, 2019.